Chapter 5
Applications: Measurement of Surface Soil Moisture

Soil moisture is a key parameter in numerous environmental studies, including hydrology, meteorology, and agriculture. Soil moisture plays an important role in the interaction between the land surface and the atmosphere, as well as in the partitioning of precipitation into runoff and ground water storage. In spite of its importance, soil moisture has not found a widespread application in the modeling of hydrological and biogeochemical processes and related ecosystem dynamics, in part because soil moisture is a difficult parameter to measure on a large-area, cost-effective, and routine basis.

It is well known that return signals from synthetic aperture radar (SAR) are affected by surface characteristics, such as the roughness, the correlation length, and the dielectric constant of the soil. Some earlier studies (Wang, et al., 1986 [1]; Dobson and Ulaby, 1986 [2]) using single frequency and single polarization Shuttle Imaging Radar-B (SIR-B) imagery could only describe the dependence of backscattering coefficient σ_0 on these surface parameters separately. Estimation of surface soil wetness was usually obtained by employing an empirical relationship to convert the measured σ_0 into volumetric soil moisture m_v (Jackson, 1993 [3]). Several research groups have, for example, reported a linear relationship between the observed radar backscatter expressed in decibels (dB) and the volumetric soil moisture of the surface (Schneider and Oppelt, 1998 [4]; Quesney et al., 2000 [5]). It is commonly reported that the slope of this linear relationship is a function of the vegetation cover, with decreasing slopes as the amount of vegetation increases indicating decreasing sensitivity to soil moisture in the presence of increasing

amounts of vegetation. As an aside, it is often found that the offset in the linear relationship is correlated with the surface roughness.

The inversion of soil moisture information from radar backscatter became more rigorous after the availability of polarimetric radar data. Basically, the additional measurements allow us to separate the effects of surface roughness and soil moisture on the observed radar backscatter. Several algorithms have been developed for measuring bare surface soil moisture quantitatively using dual-polarization L-band SAR image data (Dubois et al., 1995 [6]; Shi et al., 1997 [7]) or three-polarization SAR measurements (Oh et al., 1992 [8]).

The algorithm proposed by Oh et al. (1992) [8] was derived empirically from data measured with a truck-mounted scatterometer and the algorithm involves ratios of various polarization combinations. Dubois et al. (1995) [6] used the same data, plus data from truck-mounted scatterometers measured by the University of Berne (Wegmuller, 1993 [9]) over bare surfaces with a wide range of surface roughnesses to derive an empirical algorithm that uses horizontal-horizontal (HH) and vertical-vertical (VV) polarization combinations at L-band. Shi et al. (1997) [7] generated a synthetic data set using the Integral Equation Method (IEM) model (Fung et al.,1992 [10]) and then derived a set of coefficients to parameterize their synthetic data set. These parameters were then used to invert Airborne Synthetic Aperture Radar (AIRSAR) and SIR-C data. As in the case of Dubois et al., (1995) [6], the algorithm proposed by Shi et al. (1997) [7] uses a pair of measured radar cross-sections to estimate the surface dielectric constant and a roughness parameter. Both these algorithms have been applied to data acquired from space during the SIR-C mission and have shown accuracies on the order of 4 percent when estimating volumetric soil moisture from SAR data.

Since these early studies, many more results have been reported. We will discuss these results in more detail in this chapter. This chapter will also include a detailed of examination of the related algorithms. The chapter also includes a discussion of the algorithm proposed by Kim and van Zyl (2009) [11] that utilizes time series data to track changes in soil moisture. Finally, we shall look at the effects of vegetation on these algorithms and show that the time series algorithm shows some promise in providing the capability to measure soil moisture even in the presence of vegetation.

5.1 Surface Electrical and Geometrical Properties

Before describing the details of the individual models and their performance, we briefly review the properties, both electrical and geometrical, of rough surfaces. For the moment, we shall focus our attention on bare surfaces. The case of vegetated surfaces will be discussed later in the chapter.

5.1.1 Geometrical Properties

We can describe the local surface height of any rough surface by a two-dimensional function $\xi(x,y)$, where x and y represent the horizontal coordinates of the surface. It is typically assumed that the statistical distribution of the surface height is Gaussian with zero mean. The so-called surface roughness, or root mean square (rms) height of the surface, h is defined as

$$h^2 = \left\langle \xi^2(x,y) \right\rangle, \tag{5.1-1}$$

where $\langle x \rangle$ means the average of x Simply knowing the rms height of the surface is not yet a complete description of the geometrical properties of the surface. One also has to know how the surface height at one point on the surface is related to the surface height at a different point. This is described by the surface-height correlation function. For an isotropically rough surface, the surface-height correlation function is a function only of the separation between the two points on the surface, r. The surface-height correlation function is mathematically described by

$$\rho(r) = \frac{\left\langle \xi(x,y)\xi(x',y') \right\rangle}{h^2}. \tag{5.1-2}$$

The two most commonly used surface-height correlation functions are the Gaussian and exponential correlation functions. The Gaussian correlation function for an isotropically rough surface is

$$\rho_g(r) = e^{-r^2/l^2}. \tag{5.1-3}$$

The quantity l is known as the surface correlation length. The exponential surface-height correlation function is given by

$$\rho_e(r) = e^{-|r|/l}. \tag{5.1-4}$$

Instead of the correlation function, surfaces are often characterized in terms of their roughness spectral density, or roughness spectrum. This function is the Fourier transform of the surface autocorrelation function. For isotropically rough surfaces, the roughness spectrum is

$$W(k_x,k_y) = \frac{2}{\pi}\int_0^\infty r\rho(r)J_o(kr)dr. \tag{5.1-5}$$

The roughness spectrum functions for the Gaussian and the exponential correlation functions are

$$W_g\left(k_x,k_y\right)=\frac{l^2}{\pi}\exp\left[\frac{-\left(k_x^2+k_y^2\right)l^2}{4}\right] \tag{5.1-6}$$

and

$$W_e\left(k_x,k_y\right)=\frac{2l^2}{\pi\left[1+\left(k_x^2+k_y^2\right)l^2\right]^{3/2}}. \tag{5.1-7}$$

To understand the difference between surfaces with these different correlation functions, we show a comparison of the correlation functions in Fig. 5-1. We note that the Gaussian correlation function is larger for small separations than the exponential function, but rapidly decreases to become smaller than the exponential correlation function for larger values of r/l. This means that one would expect a surface with an exponential correlation function to appear to have larger slopes at the micro scale than a surface with an equivalent

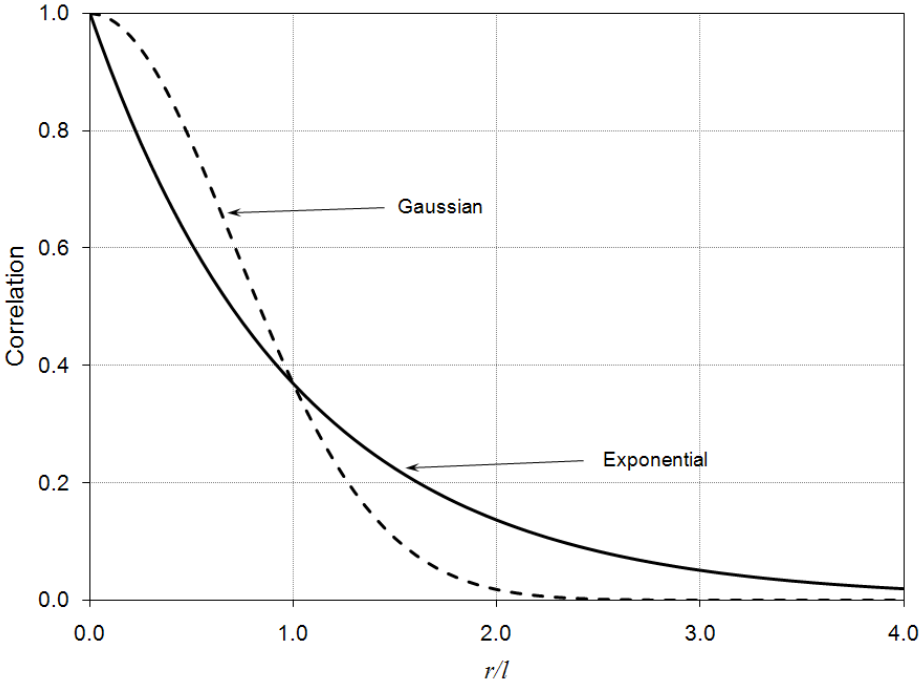

Fig. 5-1. Comparison between the Gaussian and the exponential correlation functions.

correlation length and a Gaussian correlation function. Looking at the slopes of the two types of surfaces, we note that the total mean-square slope of a surface with a Gaussian correlation function is

$$s_g^2 = \left\langle \left(\frac{\partial \xi}{\partial x} \right)^2 + \left(\frac{\partial \xi}{\partial y} \right)^2 \right\rangle = \frac{4h^2}{l^2} . \tag{5.1-8}$$

The surface with the exponential correlation function, on the other hand, has surface slopes and all higher surface derivatives that are infinite; that is,

$$s_e^2 = \infty . \tag{5.1-9}$$

To illustrate the differences between these two surface types more graphically, Figs. 5-2 and 5-3 represent two such synthetic surfaces with the same rms height and correlation length. The surface with Gaussian correlation function (shown in Fig. 5-2) appears to have less high frequency roughness than the surface with the exponential correlation function (shown in Fig. 5-3). Figures 5-3 and 5-4 show the effect of the surface correlation length on the appearance of the rough surface. Not surprisingly, the surface with the shorter correlation length appears to have more high-frequency roughness than the one with the longer correlation length.

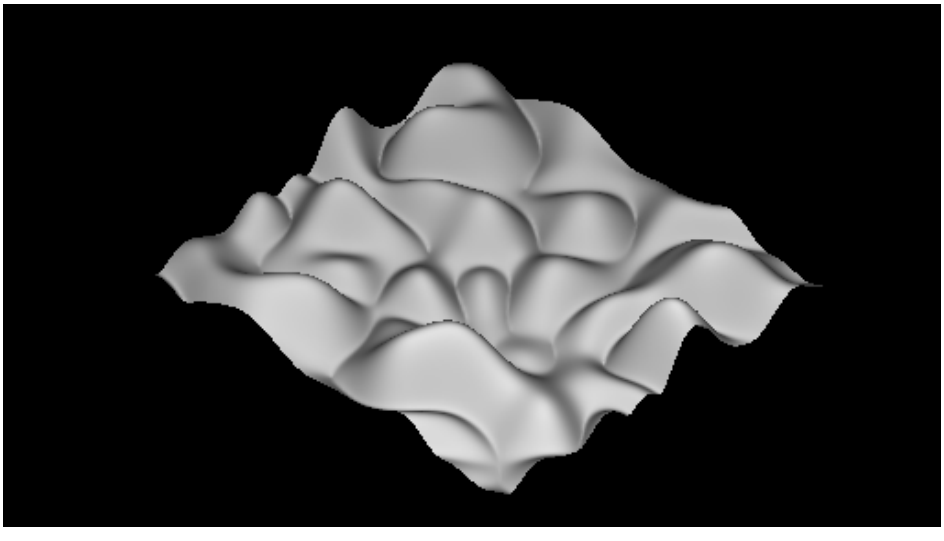

Fig. 5-2. Synthetic rough surface generated using a Gaussian surface height correlation function. Note the smooth appearance of the surface compared to that generated with the exponential surface height correlation function shown in Fig. 5-3.

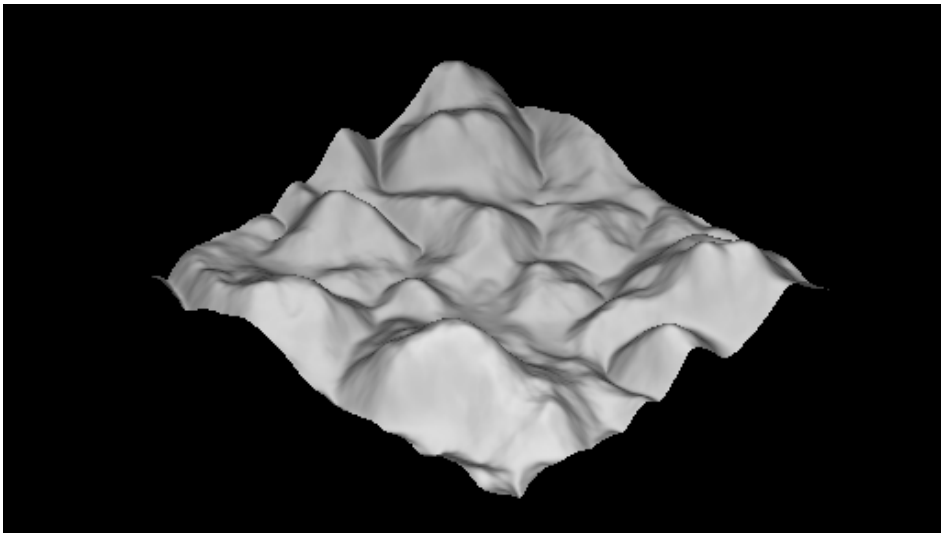

Fig. 5-3. Synthetic rough surface generated with an exponential surface height correlation function. The surface has the same rms height and correlation length as the surface generated with a Gaussian correlation functions shown in Fig. 5-2.

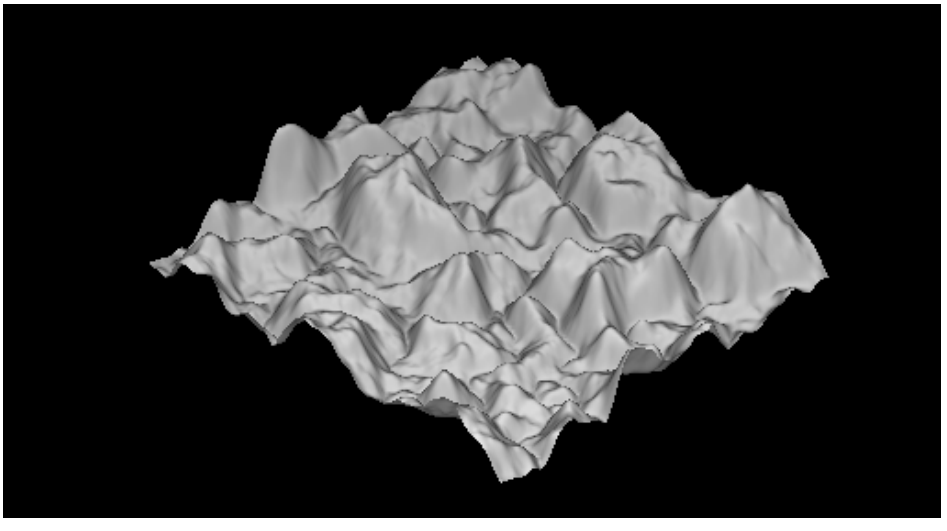

Fig. 5-4. Synthetic rough surface generated with an exponential surface height correlation function. The surface has half the correlation length of the surface shown in Fig. 5-3.

Several researchers have measured profiles of micro-topography in order to better describe the roughness characteristics of natural surfaces. The profiles of micro-topography are measured using various approaches. The simplest approach utilizes a large board with a grid painted on it. The board is then pushed into the surface to the lowest point on the surface, and a photograph is taken of the board covered with the surface profile. The profile is subsequently digitized from the photograph. The advantages offered by this approach are that it is easy to make the measurement and the equipment is relatively cheap and easily operated in the field. Disadvantages include the fact that only relatively short profiles can be measured (typically a meter or two at best) and that the soil has to be soft enough to permit insertion of the board.

A second approach utilizes a horizontal bar with an array of vertical rods of equal length that are dropped to the surface. The heights of the top of the rods above a known level surface are then measured and recorded. While relatively easier to operate than the boards described above, especially over rocky or hard surfaces, the disadvantage of this method is the limited length of the profiles that can be measured with one instrument; consequently, a large amount of time is required to make measurements of reasonably large areas, especially in areas with difficult access.

Laser profilers are also sometimes used to measure micro-topography. In this case, a laser is mounted on a frame that allows the laser to translate in a raster pattern. Measurements are typically taken every centimeter or so along a particular profile. These instruments obviously require power to operate, limiting their utility to easily accessible areas. An additional drawback is that the size of the frame usually limits the area that can be measured to a meter or so square. Another method is to operate lasers from low-flying aircraft; using this method, however, the measurement density is inadequate for micro-topography studies.

Stereo photography, either close-range or from specially equipped helicopters, seems to provide the best balance between accuracy and coverage. As part of this method, the photographs are digitized and then correlated against each other to reconstruct the micro-topography using the same kind of software developed to construct large-scale, digital-elevation models from stereo cameras flown on either aircraft or satellites. While more expensive to acquire, the full three-dimensional surface can be reconstructed over a relatively large area, providing excellent statistics.

Using stereo photographs acquired from a helicopter, Farr (1992) [12] studied the roughness characteristics of several lava flows in the Mojave Desert in southern California. He found that the power spectra of these natural surfaces exhibit the general form

$$W(k) = bk^m, \tag{5.1-10}$$

with the value of the exponent m between –2 and –3, consistent with known behavior of topography at larger scales. His measurements showed values closer to –2 and that the magnitude of m first seems to increase with lava flow age, but then decreases for surfaces between 0.14 and 0.85 million years old. For surfaces older than 0.85 million years, the magnitude of m seems to increase again.

Shi et al. (1997) [7] reports a different approach to their analysis of surface roughness characteristics. Using 117 roughness profiles measured over various fields in the Washita watershed, they fitted the correlation function of the measured profiles with a general correlation function of the form

$$\rho(r) = \exp\left(-(r/l)^n\right). \tag{5.1-11}$$

Values of $n = 1$ correspond to an exponential correlation function; $n = 2$ corresponds to a Gaussian. Their results indicate that 76 percent of the surfaces could be fitted with values of $n \le 1.4$, leading to the conclusion that the exponential correlation function is the more appropriate description of the surface correlation function.

We note that for values of $kl >> 1$, the roughness spectrum of the exponential correlation function behaves like Eq. (5.1-10) with an exponent –3. The results from the Shi et al. (1997) [7] study seem to indicate that agriculture and pasture fields have roughness spectra that contain more energy at the longer spatial scales than the natural lava flow surfaces studied by Farr [12].

5.1.2 Electrical Properties

The electrical properties of a rough surface are described by the complex dielectric constant, or relative permittivity, of the soil, which is a strong function of the soil moisture. This is the result of the fact that the dielectric resonance of both pure and saline water lies in the microwave portion of the electromagnetic spectrum. Dry soil surfaces have dielectric constants on the order of 2 - 3; water has a dielectric constant of approximately 80 at microwave frequencies. Therefore, adding a relatively small amount of water to the soil drastically changes the value of the dielectric constant.

A wet bare soil consists of a mixture of soil particles, air, and liquid water. Usually, the water contained in the soil is further divided into two parts: so-called bound water and free water. Due to the influence of matric and osmotic forces, the water molecules contained within the first few molecular layers

surrounding the soil particles are tightly held by the soil particles; hence, the term bound water. The amount of bound water is directly proportional to the surface area of the soil particles, which, in turn, is a function of the soil texture and mineralogy. Because of the relatively strong forces acting on it, bound water exhibits an electromagnetic spectrum that is different from that of regular liquid water. Since the matric forces acting on a water molecule decrease rapidly with distance away from the soil particle, water molecules located more than a few molecular layers away from the soil particles are able to move throughout the soil with relative ease; for this reason, this water is known as free water. The complex dielectric constant of both bound and free water is a function of frequency, temperature, and salinity of the soil.

In general, there is a nonlinear relationship between dielectric constant and volumetric soil moisture. Wang and Schmugge (1980) [13] present an empirical soil dielectric mixing model based on various measurements at 1.4 and 5 gigahertz (GHz). If one is concerned only with the real part of the dielectric constant, one can write the expressions as follows:

$$\varepsilon = \begin{cases} 3.25 + 2.2m_v + \dfrac{76.3E_T m_v^2}{M_T} & for \quad m_v \le M_T \\ 3.25 + 76.3M_T\left(E_T - 1\right) + 78.5m_v & for \quad m_v > M_T \end{cases}, \qquad (5.1\text{-}12)$$

where m_v is the volumetric soil moisture (units cm^3/cm^3) $0 \le m_v \le 1$ and M_T is a transition moisture level (units cm^3/cm^3), which is given by

$$M_T = 0.49W_P + 0.165\,. \qquad (5.1\text{-}13)$$

W_P is the wilting point, (in units of cubic centimeter per cubic centimeter (cm^3/cm^3)), which is a function of the soil texture, and is given by

$$W_P = 0.06774 - 0.00064S + 0.00478C\,. \qquad (5.1\text{-}14)$$

In Eq. (5.1-14), S and C represent the percentages of sand and clay, respectively, in the soil. Finally, E_T in Eq. (5.1-12) is an empirical fit coefficient, which is

$$E_T = 0.481 - 0.57W_P\,. \qquad (5.1\text{-}15)$$

For a typical loam soil:

$$W_P = 0.1; \quad M_T = 0.22; \quad E_T = 0.4\,. \qquad (5.1\text{-}16)$$

Hallikainen et al. (1985) [14] report the results of extensive measurements of soil dielectric constants. Hallikainen et al. also found that the dielectric constant can be described as a quadratic function of volumetric soil moisture. Their results show the coefficients of the polynomial to be a function of the soil texture, and the polynomial is of the general form:

$$\varepsilon = (a_0 + a_1 S + a_2 C) + (b_0 + b_1 S + b_2 C) m_v + (c_0 + c_1 S + c_2 C) m_v^2 . \qquad (5.1\text{-}17)$$

This form is applicable to both the real and imaginary parts of the dielectric constant. The coefficients are functions of frequency, with values reported from 1.4 GHz to 18 GHz. At 1.4 GHz, the values for the real part of the dielectric constant are:

$$\begin{array}{lll} a_0 = 2.862 & a_1 = -0.012 & a_2 = 0.001 \\ b_0 = 3.803 & b_1 = 0.462 & b_2 = -0.341 . \\ c_0 = 119.006 & c_1 = -0.500 & c_2 = 0.633 \end{array} \qquad (5.1\text{-}18)$$

For the imaginary part of the dielectric constant, the values are

$$\begin{array}{lll} a_0 = 0.356 & a_1 = -0.003 & a_2 = -0.008 \\ b_0 = 5.507 & b_1 = 0.044 & b_2 = -0.002 . \\ c_0 = 17.753 & c_1 = -0.313 & c_2 = 0.206 \end{array} \qquad (5.1\text{-}19)$$

For a typical loam soil, Eq. (5.1-17) becomes

$$\varepsilon = 2.2575 + 22.9925 m_v + 101.8015 m_v^2 \qquad (5.1\text{-}20)$$

for the real part of the dielectric constant.

It should be pointed out that more recent work by Brisco et al. (1992) [15] concluded that soil texture has no effect on the results, and that a single cubic polynomial with constant coefficients could be used to link soil moisture and the measured surface dielectric constant, as follows:

$$m_v = -0.0278 + 0.0280\varepsilon - 0.000586\varepsilon^2 + 0.00000503\varepsilon^3 . \qquad (5.1\text{-}21)$$

Other work (Dobson et al., 1985) [16] derived a semi-empirical relationship between the real part of the dielectric constant and the volumetric soil moisture of the form.

$$\varepsilon' = \left[1 + \frac{\rho_b}{\rho_s} \varepsilon_s^{\alpha} + m_v^{\beta} \varepsilon_{fw}^{\alpha} - m_v \right]^{1/\alpha} , \qquad (5.1\text{-}22)$$

where $\alpha = 0.65$, $\rho_s = 2.66\ g/cm^3$, ε_s is the dielectric constant of the solid soil (typical value ≈ 4.7), ρ_b is the bulk density of the soil (on the order of $1.1\ g/cm^3$ for sandy loam soils), and β is a parameter that is a function of the soil texture

$$\beta = 1.2748 - 0.00519S - 0.00152C\,. \tag{5.1-23}$$

As before, S and C are the percentage of sand and clay in the soil, respectively. The dielectric constant of free water is a function of temperature and frequency and is given by

$$\varepsilon_{fw} = \varepsilon_{w\infty} + \frac{\varepsilon_{w0} - \varepsilon_{w\infty}}{1 + (2\pi f \tau_w)^2}\,. \tag{5.1-24}$$

In Eq. (5.1-24), τ_w is the relaxation time for water, ε_{w0} is the static dielectric constant for water, $\varepsilon_{w\infty} = 4.9$ is the high frequency limit of the real part of the dielectric constant for water, and f is the frequency. Both τ_w and ε_{w0} are functions of temperature (Ulaby et al., 1986 [17]). At $20°$ C, the values are $2\pi\tau_w = 0.58 \times 10^{-10}$ seconds and $\varepsilon_{w0} = 80.1$.

A comparison of the results of the models described above is shown in Fig. 5-5 for the case of a sandy loam soil at 1.4 GHz. All models show the non-linear relationship between the soil dielectric constant and volumetric soil moisture, especially at low moisture values.

5.1.3 Penetration Depth

The question of how deep a particular radar senses the surface moisture often arises. The answer to this question is unfortunately not straightforward.

Experimental results indicate that at C-band, the radar signal is well correlated with the moisture in the top 2 cm of the soil (Bruckler et al., 1988 [18]). At L-band, good correlation is typically observed with the moisture in the top 5 cm of the soil.

From a theoretical point of view, the penetration depth depends on the complex dielectric constant ε of the surface. This quantity can be written as

$$\varepsilon = \varepsilon' + i\varepsilon''\,, \tag{5.1-25}$$

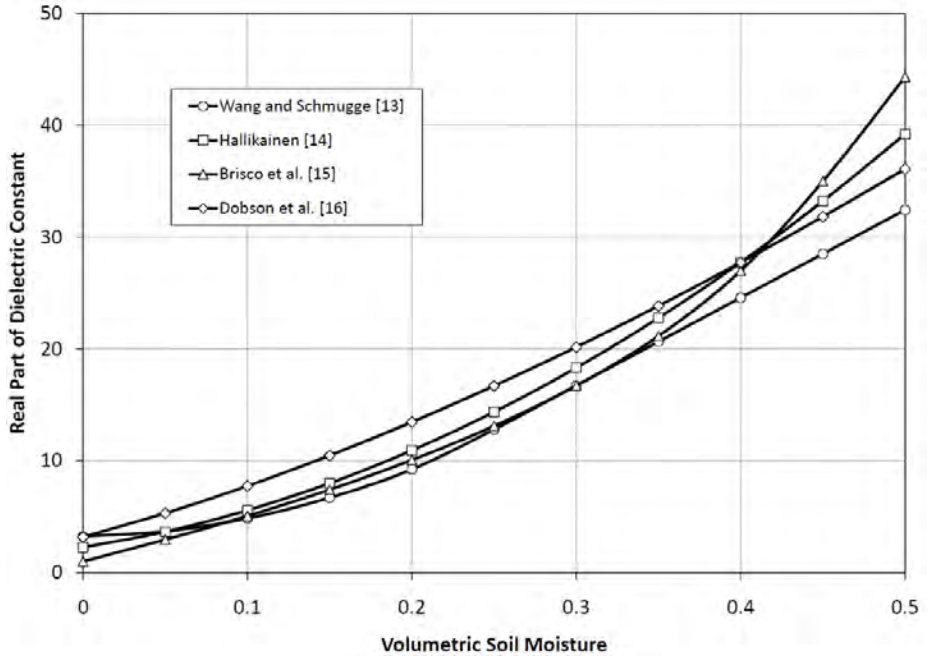

Fig. 5-5. Comparison of the results of several models linking surface dielectric constant to volumetric soil moisture. The case shown is for a sandy loam soil with 51.5 percent sand and 13.5 percent clay. Results are applicable to 1.4 GHz. Note the close comparison between the Hallikainen and Brisco curves.

where the imaginary part corresponds to the ability of the medium to absorb the wave and transform its energy to another type of energy (heat, chemical, etc.). If we consider a wave propagating purely in the x-direction in a homogeneous medium, then the electric field varies as

$$E = E_0 e^{i\sqrt{\varepsilon}kx}.$$

If we can assume that $\varepsilon'' \ll \varepsilon'$, then

$$\sqrt{\varepsilon} = \sqrt{\varepsilon' + i\varepsilon''} \approx \sqrt{\varepsilon'} + i\frac{\varepsilon''}{2\sqrt{\varepsilon'}} \tag{5.1-26}$$

and

$$E = E_0 e^{-\alpha_a x}\ e^{i\sqrt{\varepsilon'}kx}, \tag{5.1-27}$$

where

$$\alpha_a = \frac{\varepsilon'' k}{2\sqrt{\varepsilon'}} = \frac{\pi \varepsilon''}{\lambda \sqrt{\varepsilon'}}.$$

The observed radar cross-section is proportional to power. The power of the wave as a function of x can be written as:

$$P(x) = P(0)\, e^{-2\alpha_a x}. \tag{5.1-28}$$

If α_a is also a function of x, such as when the moisture profile varies with depth in the soil, then the above equation will become:

$$P(x) = P(0)\, \exp\left(-2 \int_0^x \alpha_a(\xi)\, d\xi \right). \tag{5.1-29}$$

The penetration depth L_p is defined as the depth at which the power decreases to $P(0)\, e^{-1}$ (i.e., 4.3-dB loss). Thus:

$$L_\mathrm{p} = \frac{1}{2\alpha_a} = \frac{\lambda \sqrt{\varepsilon'}}{2\pi \varepsilon''}. \tag{5.1-30}$$

This can also be expressed as a function of the medium loss tangent $(\tan \delta = \varepsilon'' / \varepsilon')$:

$$L_\mathrm{p} = \frac{\lambda}{2\pi \sqrt{\varepsilon'} \tan \delta}. \tag{5.1-31}$$

At this depth, the incident power is 4.3 dB weaker than at the surface. In the case of radar observation, if the interface is covered by a layer of thickness L_p, the attenuation due to absorption alone will be $2 \times 4.3 = 8.6$ dB for a normally incident wave. The factor 2 represents the fact that absorption affects both the incident and the scattered waves.

These expressions show that the penetration depth is a function of actual value of the dielectric constant. Based on the discussion in the previous section, this means that the penetration depth of the radar signals will then be a function of the soil moisture, with deeper penetration into dry soils and less penetration into wet soils.

Note that the penetration depth does not necessarily tell us from how deep into the soil most of the radar signal was received. As was pointed out above, the signal returned from a depth equal to the penetration depth suffered 8.6 dB of attenuation. Walker et al. (1997) [19] argue that it is unlikely that scattering

from this depth would add significantly to that arising from the soil-air interface. They suggest a modified depth based on a comparison of signals that would be received from a buried layer to that from the surface. Their results suggest a somewhat smaller sensing depth than what is normally quoted, with a reduction on the order of a factor of 2, depending on which polarization is used. A similar approach was used by Le Morvan et al. (2008) [20], who used a three-layer model to explain Advanced Synthetic Aperture Radar (ASAR) observation of soil moisture in France. As an aside, their results show significant correlations between the observed C-band backscatter and soil moisture measurements in a layer 2 - 5 cm beneath the surface. As is pointed out by these studies, however, to calculate the actual sensing depth from a theoretical point of view for anything but the simplest scattering geometries is a daunting task. For our purposes, we shall assume that, on the basis of observations and these studies, radars sense soil moisture in the top few centimeters of the soil, keeping in mind that the sensing depth is, indeed, shallower for wetter surfaces than for dry surfaces.

5.1.4 Soil Moisture Profile

When the penetration depth of a soil surface is evaluated, it is assume that the dielectric constant of the surface is uniform. However, soil moisture varies with depth [21, 22] depending upon the temperature profile, the soil type, and the surface evaporation. The soil moisture profile changes significantly as a soil surface dries after a precipitation event. The effect of the soil moisture profile on radar measurements can be evaluated by calculating the backscattering cross section from a rough surface interface on top of a layered medium with varying permittivity profile.

The reflection coefficient from a layered medium with a flat interface can be calculated for a given permittivity profile ($\varepsilon(z)$) as [23]

$$\frac{dR_n}{dz} = -i2\beta(z)R_n + \frac{d\beta(z)/dz}{2\beta(z)}\left(1 - R_n^2\right)$$

for horizontal polarization (5.1-32)

$$\frac{dR_n}{dz} = -i2\beta(z)R_n + \frac{d\left(\frac{\beta(z)}{\varepsilon(z)}\right)}{dz}\frac{\varepsilon(z)}{2\beta(z)}\left(1 - R_n^2\right)$$

for vertical polarization (5.1-33)

where

$$\beta(z) = \frac{2\pi}{\lambda}\sqrt{\varepsilon(z)}\cos\theta \tag{5.1-34}$$

Equations (5.1-32) and (5.1-33) can be solved exactly using numerical techniques. When the permittivity profile changes slowly, the reflection coefficient of the layered medium is smaller. Therefore, it is expected that the reflection coefficient will be smaller as the surface dries since the impedance changes gradually from the surface to the subsurface in addition to the lower surface dielectric constant. It is important to point out that the reflection coefficient of a soil surface with a varying moisture profile may not be the same as that calculated assuming a homogenous surface characterized by the average value of soil moisture within top 5 cm. We believe that the moisture profile may play an important role, especially for a dry surface. Notice that R_n in Eq. (5.1-32) and Eq. (5.1.33) is the specular reflection coefficient. Although the specular reflection coefficient is useful for calculating the effective impedance at the reflection interface, we must study the effects of a rough interface to realistically model backscatter from such a surface.

The backscattering cross section from a layered medium with a rough interface has been studied in [24, 25, 26]. An analytic method was derived to calculate the bistatic-scattering coefficient from a layered medium (less than three layers) with slightly rough interfaces [24]. In [24], the electromagnetic waves in each layer are expressed in terms of an infinite number of angular spectral components. A small perturbation approach is used to calculate the scattered wave, which is appropriate for the scattering calculation for a low-frequency radar system. In addition, Kuo and Moghaddam [25] used field-collected soil moisture data to understand the penetration capability of a low frequency radar. The simulation results in [25] demonstrated that both the backscattering coefficient and the co-polarization phase difference are sensitive to deep soil moisture. The inversion of the model parameters of a two-layer dielectric medium was investigated using the method of simulated annealing [26]. Although these approximate methods [24, 25] have provided the useful results, more accurate results can be obtained using a finite element method (FEM) [27, 28].

In the previous section we showed that the penetration depth is a function of the wavelength. The longer wavelength signals are expected to penetrate deeper into the surface and, depending on the moisture profile, may then sense either a drier or wetter surface. Figure 5-6 shows an example of the inferred dielectric constant of Lunar Dry Lake in Nevada using the algorithm proposed by Dubois et al. which we will discuss in detail a bit later. The oval shaped feature is the dry lake bed, which at the time of data acquisition was dry enough on the surface so that the author was able to drive a truck across the lake bed. The

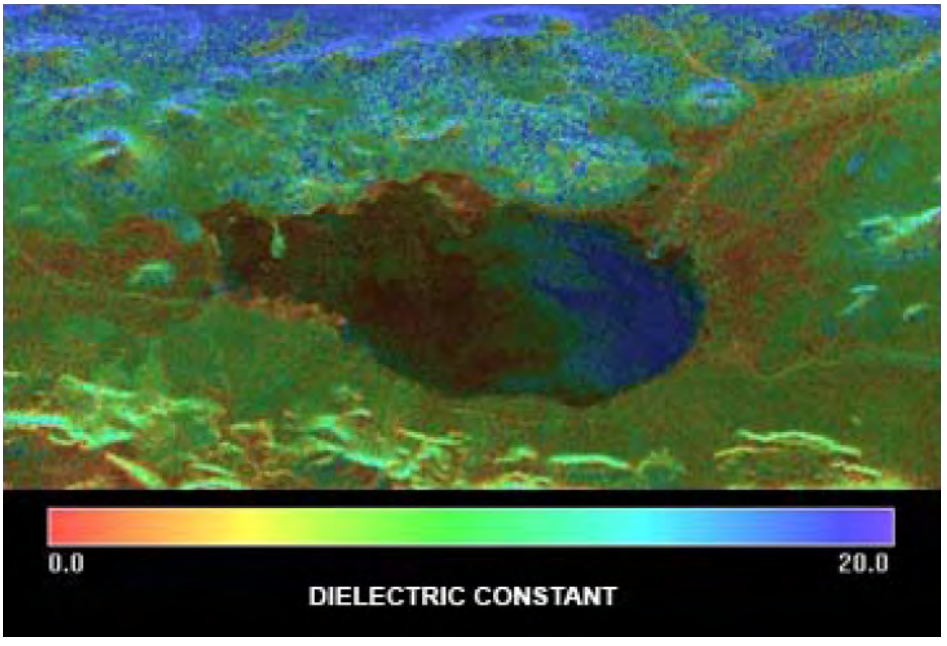

Fig. 5-6. Dielectric constant map derived from an L-Band AIRSAR image of Lunar Lake playa in Nevada. The oval shaped feature is a dry lake bed, which at the time of data acquisition was dry at the surface. The higher dielectric constant on the right portion of the lake is due to subsurface moisture. [6]

radar signals penetrated deep enough into the surface to sense subsurface moisture on the right hand side of the lake in the picture. The moisture was the remnants of runoff from light rains about a week earlier that entered the lake surface from the top right and covered only the right portion of the lake bed. The water had dried away before the data collection to the point that the surface was completely dry.

Figure 5-7 shows another example, this time showing the difference between two frequencies. The image shows a feature known as Cottonball Basin in Death Valley, California. Cottonball Basin is at the northern end of the larger Death Valley salt pan, and receives most of its inflow from groundwater. The southern edge of Cottonball Basin are covered with mud flats resulting from seeping salty water. These areas stay wet the longest after an inflow event.

Figure 5-7 shows two dielectric constant maps, the one inferred from L-band data on the left, and from P-band data on the right. There are many similarities between the two maps. First, both show relatively large dielectric constants in the mudflats, and lower dielectrics in the rest of Cottonball Basin. There are also some important differences, however. When looking closer at the mud flat areas, we note that the P-band dielectric constants show higher values over

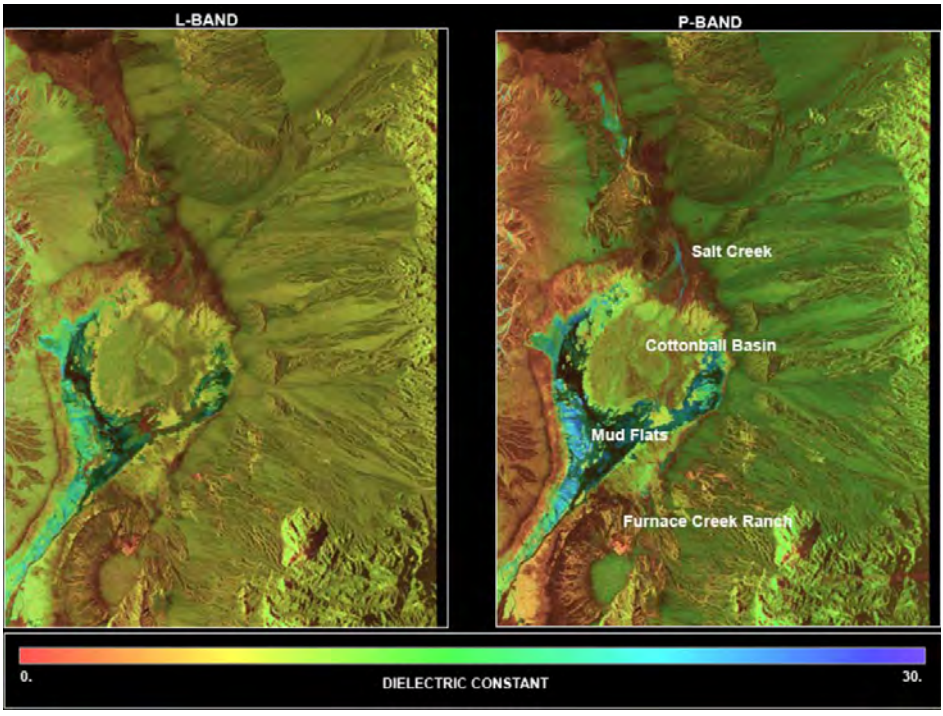

Fig. 5-7. Dielectric constant maps inferred from L-band (left) and P-band (right) AIRSAR data of Cottonball Basin in Death Valley, California. See text for discussion.

larger areas towards the edges of the mudflats. These are the shallower areas of the mud flats. As the mud flats dry out, the surface of the shallower areas dry first, while the sub-surface in these areas can stay wetter longer. The longer wavelength P-band signals more than likely penetrate deeper into these surfaces and sense more of the wetter subsurface than the L-band signals. We also note the same behavior to the northern part of the Basin, next to the word “Salt Creek” in the image. There is an area, located in the Salt Creek, that shows a higher dielectric constant at P-Band. Another area is also visible further north following the Salt Creek further up in the image. Both these areas more than likely represent subsurface moisture. Unfortunately, no actual ground measurements were made during the data collection, so these explanations cannot be verified. But given that the Dubois et al. algorithm consistently infers higher moistures at the longer wavelength in only some areas, and similar values in others, supports this conjecture.

5.2 Scattering from Bare Rough Surfaces

Many excellent texts describing the details of scattering from rough surfaces are available. Here, we will summarize some of the better known models only in

enough detail to set the stage for a better understanding of the inversion models that we will describe later. We will not, however, describe the detailed electromagnetic modeling aspects of these models.

Consider first the case of a perfectly smooth surface of infinite extent that is uniformly illuminated by a plane wave. This surface will reflect the incident wave into the specular direction with scattering amplitudes equal to the well-known Fresnel reflection coefficients. In this case, no scattered energy will be received in any other direction. If now the surface is made finite in extent, or the infinite surface is illuminated by a finite extent uniform plane wave, the situation changes. In this case, the far-field power will decrease proportional to the distance squared (the well-known R-squared law). The maximum amount of reflected power still appears in the specular direction, but a lobe structure, similar to an "antenna pattern," appears around the specular direction. The exact shape of the lobe structure depends on the size and shape of the finite illuminated area, and the pattern is adequately predicted using physical optics calculations. This component of the scattered power is often referred to as the coherent component of the scattered field. For angles far away from the specular direction, there will be very little scattered power in the coherent component.

The next step is to add some roughness to the finite surface such that the mean-square height of the surface is still much less than the wavelength of the illuminating source. The first effect is that some of the incident energy will now be scattered in directions other than the specular direction. The net effect of this scattered energy is to fill the nulls in the "antenna pattern" of the surface described before. The component of the scattered power that is the result of the presence of surface roughness is referred to as the incoherent component of the scattered field. At angles significantly away from the specular direction, such as the backscatter direction at larger incidence angles, the incoherent part of the scattered field usually dominates.

As the roughness of the surface increases, less power is contained in the coherent component and more power is contained in the incoherent component. In the limit where the rms height becomes larger than the wavelength, the coherent component is typically no longer distinguishable, and the incoherent power dominates in all directions. In this limit, the strength of the scattering in any given direction is related to the number of surface facets that are oriented such that they reflect specularly in that direction. This is the same phenomenon that causes the shimmering of the moon on a roughened water surface.

Several different criteria exist to decide if a surface is "smooth" or "rough." The most commonly used one is the so-called Rayleigh criterion that classifies a surface as rough if the rms height satisfies

$$h > \lambda/8\cos\theta\,. \tag{5.2-1}$$

In this criterion, θ is the angle at which the radar wave is incident on the surface. A more accurate approximation of surface roughness was introduced by Peake and Oliver (1971) [29]. According to this approximation, a surface is considered smooth if

$$h < \lambda/25\cos\theta\,. \tag{5.2-2}$$

A surface is considered rough if

$$h > \lambda/4\cos\theta\,. \tag{5.2-3}$$

Any surface that falls in between these two values is considered to have intermediate roughness.

Depending on the angle of incidence, two different approaches are used to model radar scattering from rough surfaces. For small angles of incidence, scattering is dominated by reflections from appropriately oriented facets on the surface. In this regime, physical optics principles are used to derive the scattering equations. As a rule of thumb, facet scattering dominates for angles of incidence less than 20 - 30 degrees (deg). For the larger angles of incidence, scattering from the small scale roughness dominates. The best known model for describing this type of scattering is the small perturbation model. This model, as its name suggests, treats the surface roughness as a small perturbation from a flat surface. More recently, Fung et al. (1992) [10] proposed a model, based on an integral equation method (IEM) solution to the scattering problem, that seems to describe the scattering adequately in both limits. Some refinements to this IEM model have been suggested by Wu et al. (2001) [30].

All models of rough surface scattering assume that the average surface is horizontal. In practice, the scattering is modulated by the local topography; this assumption, therefore, is not necessarily valid. The effect of the local topography can be described as a local tilt to the surface. This tilt is adequately described by the slope of the surface in two orthogonal directions. Note that, in this case, we mean large scale tilts, the scale of which is larger than or equal to the size of the radar pixels. The effect of such a local tilt on the scattering is two-fold. First, the wave impinges on the surface with a different local angle of incidence than it would have if the surface was not tilted. Second, the local tilt rotates the local coordinate system of the surface element with respect to that of the global system in which the radar makes its measurement. This rotation will modify the relative strengths of the scattering coefficients at the different polarizations. We will look at this effect in more detail in the next section.

Several algorithms have been proposed to invert measured radar signals to infer soil moisture. In general, the radar backscatter cross-section is a function of both the surface roughness and the surface dielectric constant (or moisture). Therefore, in order to measure either of these quantities, we must be able to separate their effects on the measured radar backscatter cross-section. Since we are trying to solve for more than one unknown, it follows that more than one measurement is needed. Most algorithms use multi-polarization measurements to accomplish the goal of separating the effects of surface roughness and dielectric constant. The sections that follow briefly discuss several of these models.

5.2.1 First-Order Small Perturbation Model

The use of the first-order small perturbation model to describe scattering from slightly rough surfaces dates back to Rice (1951) [31, 32]. Rice used a perturbation technique to show that, to first order, the scattering cross-sections of a slightly rough surface can be written as

$$\sigma_{xx} = 4\pi k^4 h^2 \cos^4\theta \left|\alpha_{xx}\right|^2 W\left(2k\sin\theta\right); \quad xx = hh \text{ or } vv, \tag{5.2-4}$$

where $k = 2\pi/\lambda$, is the wavenumber, λ is the wavelength, and θ is the local incidence angle at which the radar waves impinge on the surface. The roughness characteristics of the soil are described by two parameters: h is the surface root mean square (rms) height and $W\left(\xi_x, \xi_y\right)$ is the two-dimensional normalized surface roughness spectrum, which is the Fourier transform of the two-dimensional normalized surface autocorrelation function previously discussed in subsection 5.1.1. We note that the surface rms height should be calculated after local slopes have been removed from the surface profile; the slope of the surface changes the radar cross-section because of the change in the local incidence angle. Local slopes that tilt towards or away from the radar do not change the surface roughness; instead, they affect the local incidence angle. This is a frequent source of error in the interpretation of the results from laboratory and field experiments.

The surface electrical properties are contained in the variable α_{xx}, which is given by

$$\alpha_{hh} = \frac{(\varepsilon - 1)}{(\cos\theta + \sqrt{\varepsilon - \sin^2\theta})^2} \tag{5.2-5}$$

and

$$\alpha_{vv} = \frac{(\varepsilon - 1)\left[(\varepsilon - 1)\sin^2\theta + \varepsilon\right]}{(\varepsilon\cos\theta + \sqrt{\varepsilon - \sin^2\theta})^2}. \tag{5.2-6}$$

In these equations, ε is the dielectric constant, or relative permittivity, of the soil. We note that the small perturbation model as described here is applicable only to smooth surfaces. The usual assumptions are that the roughness is small compared to the wavelength (i.e., $kh < 0.3$) and that the rms slope (*s*) satisfies $s < 0.3$.

5.2.2 The Integral Equation Model

Fung et al. (1992) [10] showed that the expressions for the tangential surface fields on a rough dielectric surface can be written as a pair of integral equations. The scattered fields, in turn, are written in terms of these tangential surface fields. Using this formulation, and standard approximations, Fung et al. [10] showed that the scattered field can be interpreted as a single scattering term and a multiple scattering term. When the surface is smooth enough, the single scattering term reduces to the well-known small perturbation model described above and the cross-polarized terms reduce numerically to the second-order small perturbation result. Their results also show that in the high-frequency limit, only the well-known Kirchoff term described by the physical optics model remains significant for surfaces with small rms slopes. When the surface rms slopes are large, however, the multiple scattering terms are important.

Fung et al. (1992) [10] showed that the single scattering backscatter cross-sections can be written as

$$\sigma_{xy} = \frac{k^2}{2}\exp\left(-2k^2h^2\cos^2\theta\right)\sum_{n=1}^{\infty} h^{2n}\left|I_{xy}^n\right|^2 \frac{W^n(-2k\sin\theta, 0)}{n!}, \tag{5.2-7}$$

with

$$I_{xy}^n = (2k\cos\theta)^n f_{xy}\exp\left(-k^2h^2\cos^2\theta\right) + \frac{k^n\cos^n\theta\left[F_{xy}(-k\sin\theta, 0) + F_{xy}(k\sin\theta, 0)\right]}{2}. \tag{5.2-8}$$

The term W^n is the Fourier transform of the *n*th power of the surface correlation function, which can be calculated using

$$W^n(k) = \frac{2}{\pi}\int_0^{\infty} r\rho^n(r) J_o(kr)\, dr, \tag{5.2-9}$$

where $J_0(x)$ is the Bessel function of the first kind and order zero. Also,

$$f_{hh} = \frac{-2R_h}{\cos\theta}; \quad f_{vv} = \frac{2R_v}{\cos\theta}; \quad f_{hv} = f_{vh} = 0, \tag{5.2-10}$$

with R_h and R_v the well-known Fresnel reflection coefficients for horizontal and vertical polarization, respectively. Finally,

$$F_{hh}(-k\sin\theta,0) + F_{hh}(k\sin\theta,0) = \frac{-2\sin^2\theta(1+R_h)^2}{\cos\theta}\left[\left(1-\frac{1}{\mu}\right) + \frac{\mu\varepsilon - \sin^2\theta - \mu\cos^2\theta}{\mu^2\cos^2\theta}\right] \tag{5.2-11}$$

$$F_{vv}(-k\sin\theta,0) + F_{vv}(k\sin\theta,0) = \frac{2\sin^2\theta(1+R_v)^2}{\cos\theta}\left[\left(1-\frac{1}{\varepsilon}\right) + \frac{\mu\varepsilon - \sin^2\theta - \varepsilon\cos^2\theta}{\varepsilon^2\cos^2\theta}\right] \tag{5.2-12}$$

and

$$F_{hv}(-k\sin\theta,0) + F_{hv}(k\sin\theta,0) = 0, \tag{5.2-13}$$

where μ is the relative permeability of the surface and ε is the relative permittivity, or dielectric constant. Note again that the single scattering term does not predict any depolarization. The cross-polarized return is predicted by the multiple scattering term. The expressions are quite complicated and are given in Fung et al. (1992) [10].

Figure 5-8 shows the predicted backscatter cross-section as a function of incidence angle for different surface roughness values and different dielectric constants. The plot on the left shows that increasing the surface roughness generally causes an increase in the radar cross-sections for all polarization combinations. Notice how the difference between the HH and VV cross-sections becomes smaller as the surface gets rougher. The plot on the right shows that increasing the dielectric constant (or soil moisture) also increases the radar cross-sections for all polarizations. In this case, however, increasing the dielectric constant also increases the difference between the HH and VV cross-sections.

5.3 Example Bare Surface Soil Moisture Inversion Models

In this section, we discuss some examples of previously reported soil moisture inversion models. All of these examples try to invert for soil moisture using

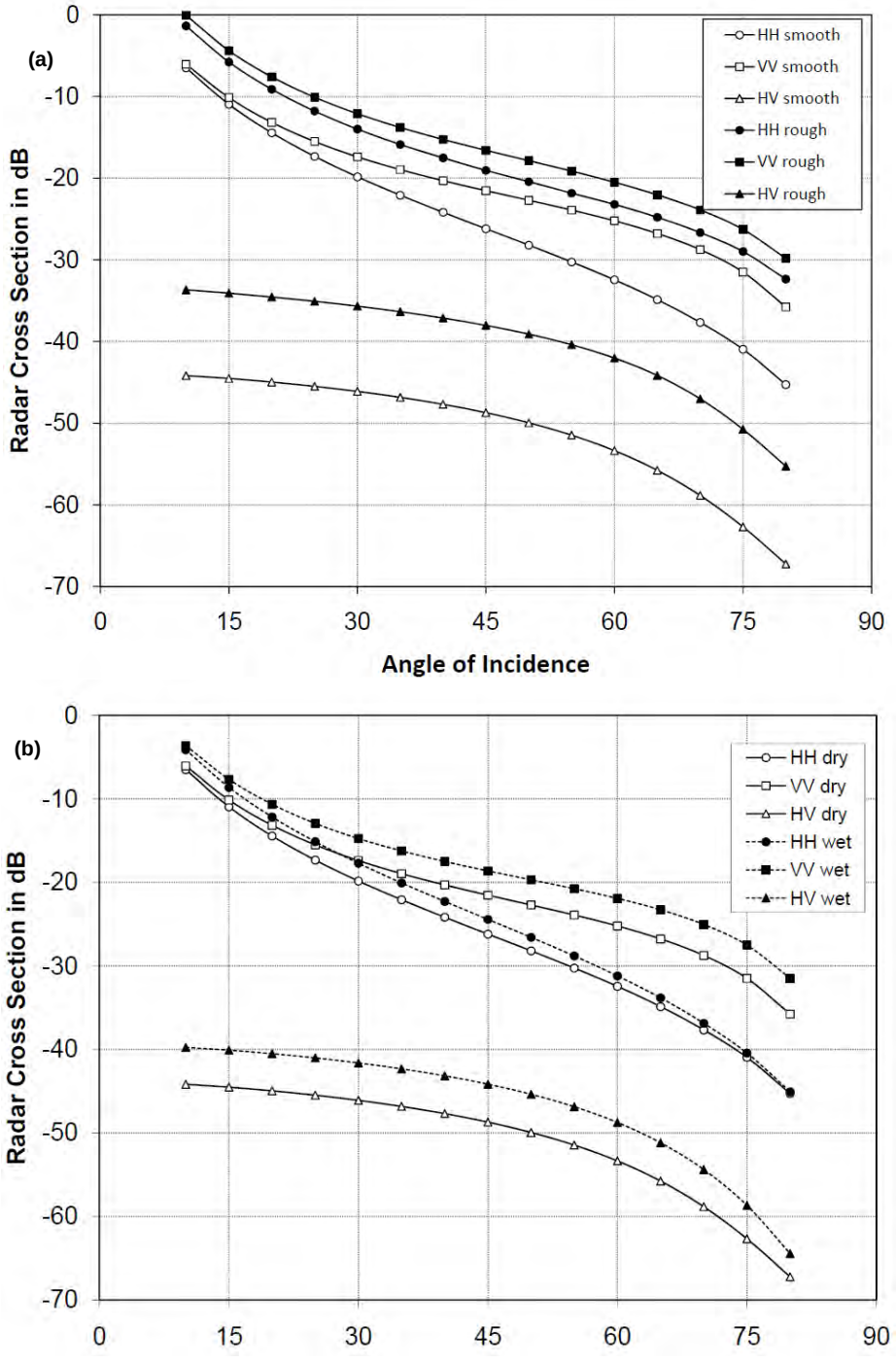

Fig. 5-8. The predicted radar cross-sections for a slightly rough surface, assuming an exponential correlation function. Chart (a) on the top shows the effect of changing surface roughness for constant dielectric constant; chart (b) on the bottom shows the effect of changing dielectric constant for constant roughness.

radar measurements made at one instant in time. As such, they can be considered to attempt to provide a "snap-shot" of soil moisture at the time the radar measurements were made. They commonly use only the radar measurements from that time instant and no other measurements from other times or other sensors.

5.3.1 The First-Order Small Perturbation Model

Returning to the expression for the small perturbation radar cross-section as given in Eq. (5.2-4), we note that the copolarized ratio

$$\frac{\sigma_{hh}}{\sigma_{vv}} = \left|\frac{\alpha_{hh}}{\alpha_{vv}}\right|^2 = \left|\frac{1}{(\varepsilon-1)\sin^2\theta+\varepsilon}\,\frac{(\varepsilon\cos\theta+\sqrt{\varepsilon-\sin^2\theta})^2}{(\cos\theta+\sqrt{\varepsilon-\sin^2\theta})^2}\right|^2 \qquad (5.3\text{-}1)$$

is only a function of the surface dielectric properties, and not of the surface roughness. Therefore, one should be able to use the measure ratio of radar cross-sections to infer the surface dielectric constant. Figure 5-9 shows how this ratio changes smoothly as the dielectric constant increases or as the incidence angle changes.

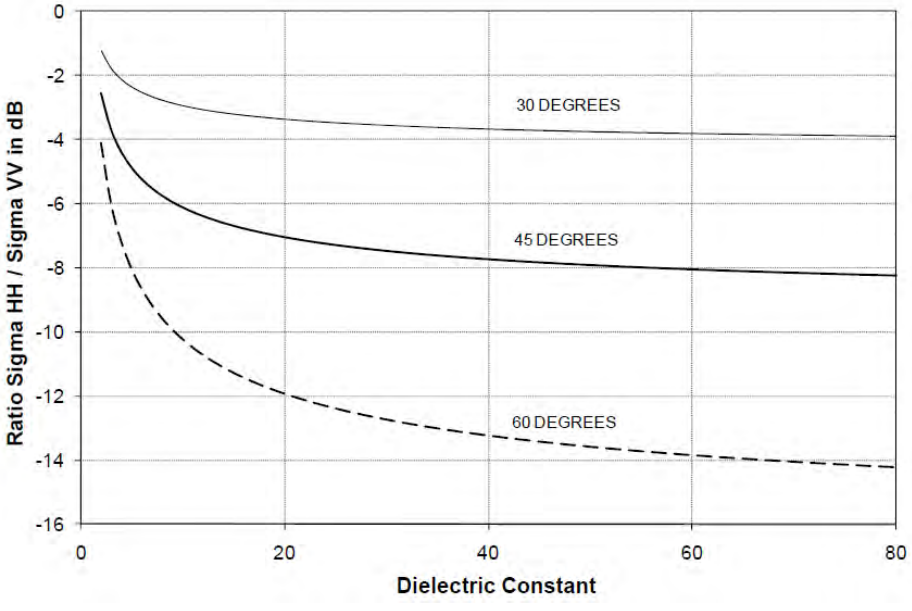

Fig. 5-9. The ratio of σ_{HH} to σ_{VV} as predicted by the small perturbation model. This ratio monotonically decreases as the dielectric constant increases. It also decreases with increasing incidence angle.

If we assume the dielectric constant to be a real number, it is possible to rewrite this expression into a fourth-order polynomial in ε as follows:

$$a_4\varepsilon^4 + a_3\varepsilon^3 + a_2\varepsilon^2 + a_1\varepsilon + a_0 = 0\,, \tag{5.3-2}$$

where

$$\begin{aligned}
a_4 &= \left[1+\sin^2\theta+\sqrt{R}\cos^2\theta\right]^2 \\
a_3 &= -2\left[2\sin^2\theta-\cos^2\theta\left(1+\sin^2\theta\right)+\sin^4\theta-\sqrt{R}\right]\left[1+\sin^2\theta+\sqrt{R}\cos^2\theta\right] \\
&\quad -4\cos^2\theta\left[1+\sqrt{R}+\sin^2\theta\right]^2 \\
a_2 &= \left[2\sin^2\theta-\cos^2\theta\left(1+\sin^2\theta\right)+\sin^4\theta-\sqrt{R}\right]^2 \\
&\quad -2\sin^2\theta\left[1+\sin^2\theta+\sqrt{R}\cos^2\theta\right]\left[\cos 2\theta+\sqrt{R}\right] \\
&\quad +\sin^2 2\theta\left[1+\sqrt{R}+\sin^2\theta\right]\left[3+\sqrt{R}+\sin^2\theta\right] \\
a_1 &= 2\left[2\sin^2\theta-\cos^2\theta\left(1+\sin^2\theta\right)+\sin^4\theta-\sqrt{R}\right]\left[\cos 2\theta+\sqrt{R}\right] \\
&\quad -2\sin^2\theta\sin^2 2\theta\left[1.5+\sqrt{R}+\sin^2\theta\right] \\
a_0 &= \sin^4\theta\left[1+2\sqrt{R}\cos 2\theta+R\right]
\end{aligned} \tag{5.3-3}$$

and

$$R = \frac{\sigma_{vv}}{\sigma_{hh}}\,. \tag{5.3-4}$$

To invert the radar measurements for surface dielectric constant, one then has to find the roots of this fourth-order polynomial. As an example, consider the case of a radar wave incident at 45 deg on a surface with $\varepsilon = 10$. The polynomial in this case is

$$0.240270\varepsilon^4 - 3.01021\varepsilon^3 + 6.56937\varepsilon^2 - 5.06918\varepsilon + 1.26975 = 0\,,$$

with roots

$$\varepsilon = 0.528;\quad 0.996;\quad 1.004;\quad 10.000\,.$$

Solving for the roots of a fourth-order polynomial is computationally quite intensive. Looking again at Fig. 5-9, we note that the co-polarized ratio decreases monotonically as the dielectric constant increases. This type of function is ideally suited to be inverted using a look-up table approach. This approach uses a table with one row for every 1 deg in incidence angle and dielectric constants as integers. Once the four table entries are identified that

bracket the measured value in incidence angle and the dielectric constant, bilinear interpolation is used between these values to find the final dielectric constant. This method provides an increase of approximately a factor 20 in computational speed over solving for the roots of the polynomial with a negligible decrease in accuracy.

We can relax the requirement that the dielectric constant must be real by performing the look-up table calculation using the soil moisture and one of the models that relate soil moisture to the complex dielectric constant. This approach would require making some assumptions about the type of soil: specifically, the texture and salinity. These assumptions must be made in any case if one wants to translate the measured dielectric constant to soil moisture.

As pointed out before, the small perturbation model is only applicable to surfaces that are smooth. While this model predicts the ratio (HH/VV) of the co-polarized radar cross-sections to be independent of the surface roughness, observations show this ratio to increase with increasing roughness. Extending the perturbation model to include second-order terms, one finds that this ratio is, indeed, affected by the surface roughness and that the effect of the roughness is to increase this ratio; that is, to make the VV cross-section closer to that at HH polarization. The net effect of this is that the measured value appears to shift to the left on the curves shown in Fig. 5-9, with the result that a first-order small perturbation inversion will tend to underestimate the surface dielectric constant in the presence of significant roughness. (We will illustrate this more clearly in the next section.) As a result of this, one could argue that the actual dielectric constant of a rough surface will be larger than or equal to the result of a first-order small perturbation inversion.

5.3.2 Algorithm Proposed by Oh et al. (1992)

Based on the scattering behavior in limiting cases and experimental data, Oh et al. (1992) [8] have developed an empirical model in terms of the rms surface height, the wave number, and the relative dielectric constant. The key to this approach is the co-polarization ratio p and cross-polarization ratio q, which are given explicitly in terms of the roughness and the soil dielectric constant. The parameters p and q from the Oh's algorithm are derived using an empirical fit to the data collected by their truck-mounted scatterometer system over bare soils of different roughness and moisture conditions. The explicit expressions for p and q are:

$$p = \frac{\sigma_{hh}}{\sigma_{vv}} = \left\{1 - \left(\frac{2\theta}{\pi}\right)^{1/3\Gamma_0} \cdot \exp(-kh)\right\}^2 \tag{5.3-5}$$

and

$$q = \frac{\sigma_{hv}}{\sigma_{vv}} = 0.23\sqrt{\Gamma_0}\cdot[1-\exp(-kh)], \tag{5.3-6}$$

where

$$\Gamma_0 = \left|\frac{1-\sqrt{\varepsilon}}{1+\sqrt{\varepsilon}}\right|^2. \tag{5.3-7}$$

As before, $k = 2\pi/\lambda$, is the wavenumber, λ is the wavelength, and ε is the complex dielectric permittivity.

Figure 5-10 shows how the co- and cross-polarized ratios are predicted to vary with changing surface roughness and dielectric constant. For large surface roughness, the co-polarized ratio approaches 1, independent of the surface dielectric constant, consistent with experimental observations. For lower dielectric constants, the co-polarized ratio is more sensitive to variations in dielectric constant than in roughness; note, however, that this is not the case for

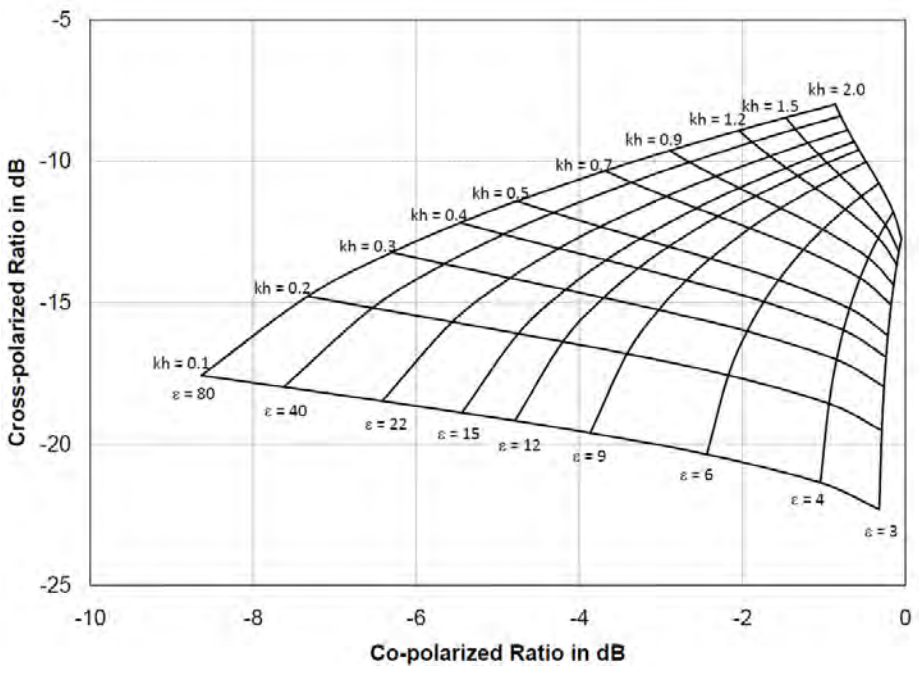

Fig. 5-10. Variation of the co- and cross-polarized ratios as a function of dielectric constant and surface roughness, as predicted by the model proposed by Oh et al. (1992) [8]. The results shown are for a 45-deg incidence angle.

high dielectric constant surfaces. The cross-polarized ratio is always a strong function of surface roughness. For rougher surfaces, this ratio is also quite sensitive to changes in dielectric constant and, in the limit of very rough surfaces, becomes a function of dielectric constant only. We also note that as the surface roughness increases, all the values bunch together more, meaning that we will have less sensitivity to moisture (or roughness) in our measurements, and larger uncertainties in the inferred quantities will likely result in the presence of measurement errors.

To invert the expressions for the soil dielectric constant, we note that we can rewrite Eq. (5.3-5) and Eq. (5.3-6) in terms of only the surface dielectric constant as

$$\sqrt{p} = 1 - \left(\frac{2\theta}{\pi}\right)^{1/3\Gamma_0} \left(1 - \frac{q}{0.23\sqrt{\Gamma_0}}\right). \tag{5.3-8}$$

Two approaches can be followed to solve this nonlinear equation in the dielectric constant: the first is to use an iterative scheme; the second is to use a look-up table approach. We found that the most efficient way (in terms of computational speed) to solve this expression for the dielectric constant is to use a look-up table inversion.

We can derive a similar expression to solve for the surface roughness from Eq. (5.3-5) and Eq. (5.3-6) as

$$\frac{0.0529\left(1 - e^{-kh}\right)^2}{q^2} \log\left(\frac{2\theta}{\pi}\right) - kh = \log\left(1 - \sqrt{p}\right). \tag{5.3-9}$$

As in the case of the dielectric constant, a look-up table approach is used to solve this expression for the rms height from the measured values of the co- and cross-polarized ratios.

One potential practical problem of the algorithm proposed by Oh et al. (1992) [8] is the fact that the cross-polarized ratio is strongly affected by the presence of vegetation. Several studies have shown that the cross-polarized return is strongly correlated with vegetation biomass; and as a result, even a relatively small amount of vegetation increases the cross-polarized ratio significantly over that of a bare surface. The presence of natural vegetation also tends to increase the co-polarized ratio, but to a lesser extent. The result is to artificially move the measurement to the upper right in Fig. 5-8, which means that the dielectric constant of the surface will be underestimated and the surface roughness will be overestimated.

5.3.3 Algorithm Proposed by Dubois et al.

Partly to avoid the difficulties that the Oh et al. (1992) [8] algorithm has when vegetation is present, Dubois et al. (1995) [6] developed an empirical model that only requires measurements of σ_{hh} and σ_{vv} at a frequency between 1.5 and 11 GHz to retrieve both the surface rms height *h* and soil dielectric constant ε from bare soils. They used two sets of ground-based scatterometer data collected by Oh et al. (1992) [8] and by the University of Berne's Radiometer Scatterometer (RASAM) (Wegmuller, 1993 [9]) system to develop two equations that relate the measured co-polarized cross sections to surface roughness and dielectric constant. Those equations are:

$$\sigma_{hh} = 10^{-2.75} \cdot \left(\frac{\cos^{1.5}\theta}{\sin^{5}\theta}\right) \cdot 10^{0.028 \cdot \varepsilon \cdot \tan\theta} \cdot (kh \cdot \sin\theta)^{1.4} \cdot \lambda^{0.7} \qquad (5.3\text{-}10)$$

and

$$\sigma_{vv} = 10^{-2.35} \cdot \left(\frac{\cos^{3}\theta}{\sin^{3}\theta}\right) \cdot 10^{0.046 \cdot \varepsilon \cdot \tan\theta} \cdot (kh \cdot \sin\theta)^{1.1} \cdot \lambda^{0.7}. \qquad (5.3\text{-}11)$$

Note that the wavelength used in these expressions must be in centimeters. These equations have been applied to a number of AIRSAR images of the Little Washita watershed and SIR-C measurements over a bare field by Dubois et al. (1995) [6], and the estimated m_v (using Hallikainen's equations to relate dielectric constant and soil moisture) values were found to agree well with those measured by ground sampling, with a resulting rms error on the order of 4–6 percent [6].

We note that the expressions derived by Dubois et al. [6] predict that the co-polarized ratio will exceed 1 in the limit of surfaces with large rms heights. Experimental results suggest that this ratio will asymptotically approach one, but will not exceed 1. This deficiency in the Dubois et al. model makes their results for rougher surfaces suspect.

Figure 5-11 shows how the VV cross-section and the co-polarized ratio are predicted to vary with changing surface roughness and dielectric constant. In contrast to the model proposed by Oh et al. [8], the co-polarized ratio does not approach 1 for large surface roughness. As mentioned before, this represents one shortcoming in the Dubois et al. model, and this failure to approach 1 is a consequence of the linear approximation they applied to the measured data in the logarithmic domain. All the curves run parallel in both directions, suggesting that the sensitivity of the cross-sections to roughness is independent of the actual value of the dielectric constant and vice versa. This, again, is a consequence of the linear approximation assumed.

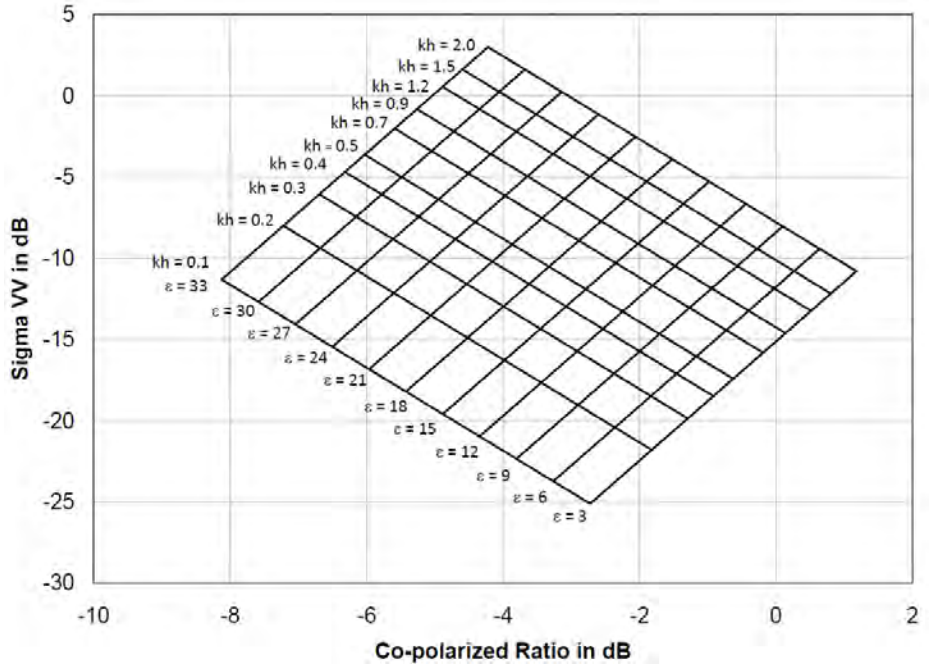

Fig. 5-11. Variation of the VV cross-section and the co-polarized ratio as a function of dielectric constant and surface roughness as predicted by the model proposed by Dubois et al. (1995) [6]. The results shown are for 45 deg incidence angle and L-band.

The Dubois et al. [6] expressions can be rewritten by expressing the radar cross-sections in decibels as follows

$$\sigma_{xx}\left(dB\right) = A_{xx}\varepsilon + B_{xx}\log_{10}(kh) + C_{xx}; \quad xx = hh \; or \; vv \,. \tag{5.3-12}$$

Using the expressions in Eq. (5.3-10) and Eq. (5.3-11), we find that

$$\begin{aligned} A_{hh} &= 0.28\tan\theta \\ B_{hh} &= 14 \\ C_{hh} &= -27.5 + 15\log_{10}\left(\cos\theta\right) - 36\log_{10}\left(\sin\theta\right) + 7\log_{10}\left(\lambda\right) \\ A_{vv} &= 0.46\tan\theta \\ B_{vv} &= 11 \\ C_{vv} &= -23.5 + 30\log_{10}\left(\cos\theta\right) - 19\log_{10}\left(\sin\theta\right) + 7\log_{10}\left(\lambda\right) \end{aligned} \,. \tag{5.3-13}$$

Equation (5.3-12) can be written in matrix form as follows

$$\begin{bmatrix} A_{hh} & B_{hh} \\ A_{vv} & B_{vv} \end{bmatrix} \begin{pmatrix} \varepsilon \\ \log_{10}(kh\cdot) \end{pmatrix} = \begin{pmatrix} \sigma_{hh} - C_{hh} \\ \sigma_{vv} - C_{vv} \end{pmatrix}. \tag{5.3-14}$$

Inverting this expression, we find that the solution for the Dubois et al. algorithm [6] is

$$\begin{pmatrix} \varepsilon \\ \log_{10}(kh\cdot) \end{pmatrix} = \frac{1}{A_{hh}B_{vv} - A_{vv}B_{hh}} \begin{bmatrix} B_{vv} & -B_{hh} \\ -A_{vv} & A_{hh} \end{bmatrix} \begin{pmatrix} \sigma_{hh} - C_{hh} \\ \sigma_{vv} - C_{vv} \end{pmatrix}. \tag{5.3-15}$$

The explicit inversion for the dielectric constant is

$$\begin{aligned} \varepsilon = \frac{1}{3.36\tan\theta}\{&14\sigma_{vv}(dB) - 11\sigma_{hh}(dB) + 26.5 - 255\log_{10}(\cos\theta) \\ &- 130\log_{10}(\sin\theta) - 21\log_{10}(\lambda)\} \end{aligned}. \tag{5.3-16}$$

According to Dubois et al. (1995) [6], their algorithms is applicable to surfaces with $kh < 3.0$ and $30^0 \le \theta \le 70^0$. The range of experimental values available during algorithm development is what places the upper limit on the surface roughness. From Eq. (5.3-15), we find the inversion for the surface roughness to be

$$\begin{aligned} \log(kh) = &-0.083\sigma_{vv}(dB) + 0.137\sigma_{hh}(dB) + 1.807 - 0.446\log_{10}(\cos\theta) \\ &- 3.345\log_{10}(\sin\theta) - 0.375\log_{10}(\lambda) \end{aligned}. \tag{5.3-17}$$

In the presence of vegetation, the co-polarized ratio is affected more than the absolute radar cross section. This means that we can expect the presence of vegetation to move a measurement mostly to the right in Fig. 5-11. The result is that the dielectric constant will be underestimated and the roughness will be overestimated. An obvious advantage of the Dubois et al. model is the simple inversion equations that are easily and efficiently implemented [6].

5.3.4 Algorithm Proposed by Shi et al. (1997) [7]

A concern about the empirical approaches described so far is that these models do not take into account the shape of the surface power spectrum that is related to the surface roughness correlation function and correlation length. This is not consistent with theoretical surface backscattering model predictions: i.e., the backscattering coefficients are sensitive not only to soil moisture m_v and surface root mean square (rms). height *h*, but also to the shape of the surface roughness power spectrum. In addition, any empirical model developed from a limited number of observations might give site-specific results because of the nonlinear response of backscattering to the soil moisture and surface roughness parameters. This drawback might be reduced by using data from many different

sites, but it is very difficult to acquire data experimentally that would cover all possible types of surfaces and include the entire range of expected roughness and moisture conditions.

Progress in theoretical modeling, such as the Integral Equation Method (IEM) (Fung et al., 1992 [10]), offers an alternative approach for the retrieval of soil moisture from radar data. Although the IEM model is valid for a wider range of surface roughness conditions when compared to other earlier theoretical models, the complexity of this model makes its application directly to the radar data to infer soil moisture and roughness parameters rather difficult. Since the number of independent radar measurements is usually limited, Shi et al. (1997) [7] developed a model by parameterizing IEM model-based numerical simulations for a wide range of surface roughness and soil moisture conditions.

Shi et al. (1997) [7] examined many different combinations of polarizations of AIRSAR and SIR-C measurements at L-band to evaluate their effectiveness in the estimation of m_v and h. Several pairs of the measurements were found to be nearly equally effective when the AIRSAR and SIR-C quad-polarized data acquired over the Little Washita watershed were used. Two of these combinations, $\sqrt{\sigma_{hh}\sigma_{vv}}$ and $\sigma_{hh}+\sigma_{vv}$, provided the best fit with three different correlation functions used in the simulation. The following two equations were used to estimate soil moisture and a surface roughness parameter S_R from SIR-C and AIRSAR data (Shi et al., 1997 [7]):

$$10\log_{10}\left[\frac{|\alpha_{vv}|^2}{\sigma_{vv}}\right]=a_{vv}(\theta)+b_{vv}(\theta)10\log_{10}\left[\frac{1}{S_R}\right] \tag{5.3-18}$$

and

$$10\log_{10}\left[\frac{|\alpha_{vv}|^2+|\alpha_{hh}|^2}{\sigma_{vv}+\sigma_{hh}}\right]=a_{vh}(\theta)+b_{vh}(\theta)10\log_{10}\left[\frac{|\alpha_{vv}||\alpha_{hh}|}{\sqrt{\sigma_{vv}\sigma_{hh}}}\right]. \tag{5.3-19}$$

In these expressions, the surface roughness parameter $S_R=(kh)^2W$, k is the wave number, and h is the surface rms height. W is the roughness spectrum of the surface, α_{hh} and α_{vv} are the polarization amplitudes for HH- and VV-polarization as in the small perturbation model that depends only on the dielectric constant of the soil ε and the incidence angle θ, as was previously demonstrated. The coefficients that are functions of the angle of incidence in Eq. (5.3-6) and Eq. (5.3-7) are

$$\begin{aligned} a_{vv}(\theta) &= -6.901 + 5.492\tan\theta - 1.051\log(\sin\theta) \\ b_{vv}(\theta) &= 0.515 + 0.896\sin\theta - 0.475\sin^2\theta \\ a_{vh}(\theta) &= \exp\left[-12.37 + 37.206\sin\theta - 41.187\sin^2\theta + 18.898\sin^3\theta\right] \\ b_{vh}(\theta) &= 0.649 + 0.659\cos\theta - 0.306\cos^2\theta \end{aligned} \quad . \qquad (5.3\text{-}20)$$

To understand the inversion of this model better, we note that it is possible to rewrite Eq. (5.3-19) in the following form:

$$\frac{|\alpha_{vv}|^2 + |\alpha_{hh}|^2}{\left(|\alpha_{vv}||\alpha_{hh}|\right)^{b_{vh}(\theta)}} 10^{-a_{vh}(\theta)/10} = \frac{\sigma_{vv} + \sigma_{hh}}{\left(\sigma_{vv}\sigma_{hh}\right)^{b_{vh}(\theta)/2}} . \qquad (5.3\text{-}21)$$

Figure 5-12 shows the behavior of the left-hand side of Eq. (5.3-21) as a function of dielectric constant.

Conceptually, the inversion algorithm for the Shi et al. algorithm [7] works as follows. The measured co-polarized returns are used to calculate the right side of Eq. (5.3-21). This value is then used in Fig. 5-12, at the appropriate incidence angle, to "read" the dielectric constant. We found a look-up table approach to be the most efficient way to invert Eq. (5.3-21) for the surface dielectric constant.

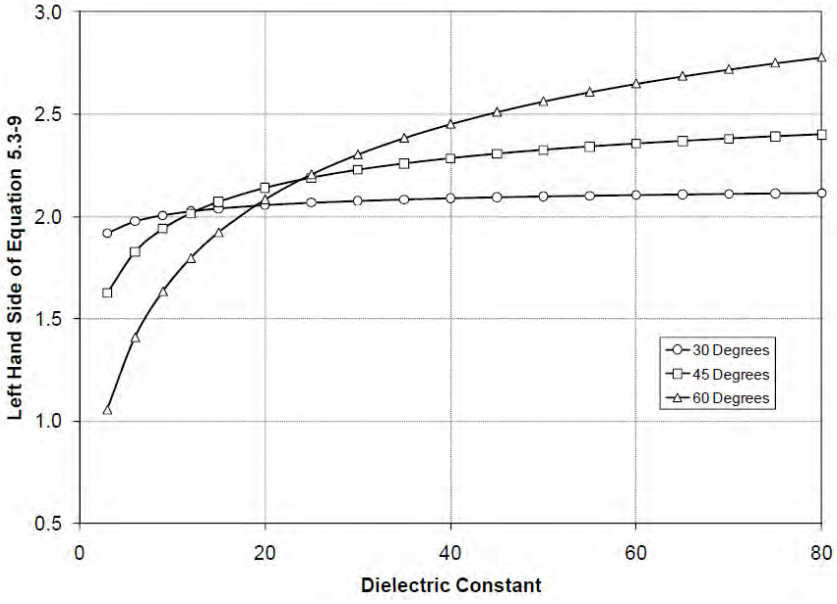

Fig. 5-12. The relationship between dielectric constant and the left hand side of Eq. (5.3-9) is a monotonically increasing function. The sensitivity of the Shi et al. algorithm is better at larger incidence angles.

5.4 Comparison of the Performance of Bare Surface Inversion Models

To investigate the ability of the individual algorithms to take the effect of surface roughness into account during the inversion, we follow this assessment by applying all the algorithms to the same AIRSAR L-band data set of a sparsely vegetated (less than 5% cover) alluvial fan in Death Valley, California, acquired during the summer of 1993. The moisture content of the soil is extremely low this time of the year, with the result that one expects similar low soil moisture throughout the scene. If we invert for the surface dielectric constant, we would expect those areas covered with more rocks to have a slightly higher dielectric constant and the valley floor where salt deposits causes the dielectric constant to be quite high (typically > 40) because of the increase in salinity. The L-band total power image for this data set is shown in Fig. 5-13.

The large alluvial fan is the Trail Canyon fan on the west side of Death Valley. The older, smoother surfaces are shown as the darker features; the rougher,

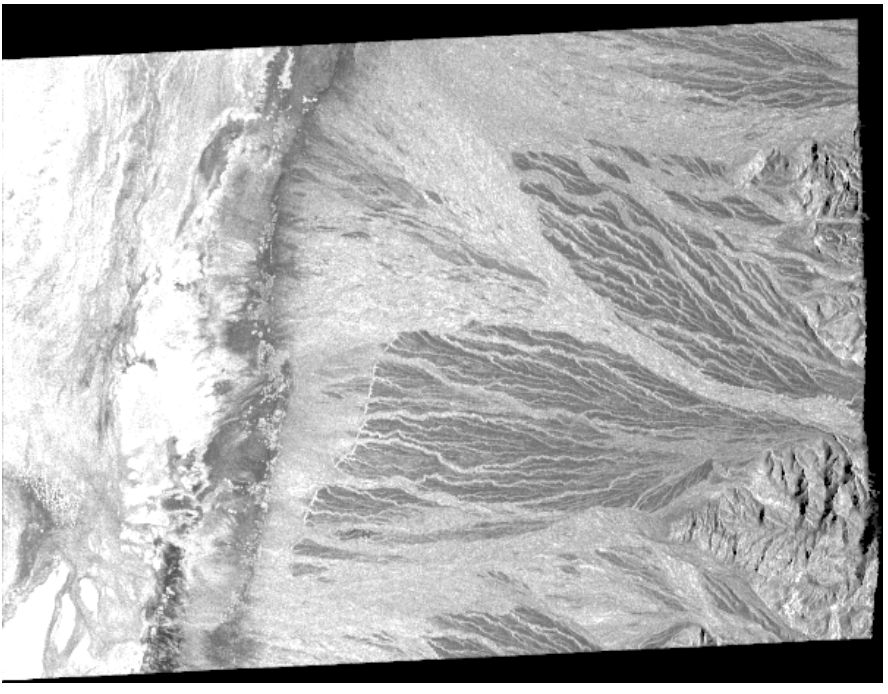

Fig. 5-13. L-band total power image of the Trail Canyon alluvial fan on the west side of Death Valley, California. The radar illumination is from the left. The bright areas on the left in the images are salty soils in the valley floor. The darker areas on the fan surface represent older, smoother fan surfaces. Active stream channels are rougher, appearing bright in the image. The image was acquired in summer when the surfaces are uniformly dry and low dielectric constants are expected.

younger surfaces are brighter, indicating more backscatter. The valley floor is covered with a rougher, salty soil and appears very bright in the image, as does the active stream channels that are covered with rocks and small boulders.

Figure 5-14 shows the inversion result for the dielectric constant for the small-perturbation algorithm described in the previous section. The first obvious observation is that this result does not appear uniform on the alluvial fan, as expected. Instead, the darker areas in the total power image, corresponding to the smoother surfaces, have higher dielectric constants than the brighter, rougher areas. As mentioned before, the ratio of the cross-sections at *hh* and *vv* is a function of the surface roughness. The first-order small-perturbation model fails to take this into account and underestimates the dielectric constant of the rougher surfaces. Note that we have applied the small-perturbation model to the

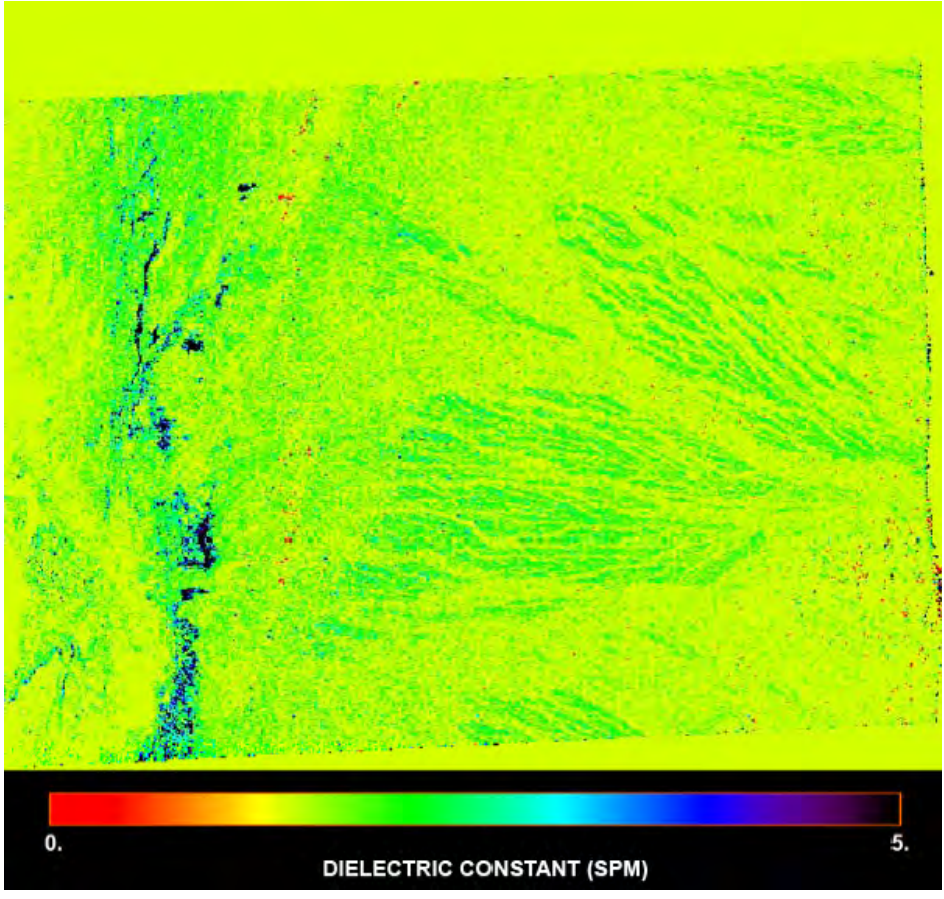

Fig. 5-14. Inversion results using the small-perturbation model algorithm. The algorithm results, as expected, are affected significantly by the changes in surface roughness, and consistently estimates lower values of dielectric constant for the rougher surfaces. Note the scale difference with the other figures following.

entire image even if the surface is rougher than that for which the small-perturbation model is supposed to be applicable. This was done only to illustrate the shortcomings of the small perturbation model in terms of not taking into account the effects of surface roughness on the HH/VV ratio.

Figure 5-15 shows the inversion result for the algorithm proposed by Oh et al. (1992) [8]. The algorithm also estimates higher dielectric constants on the smoother surfaces, but the difference is somewhat less pronounced than in the case of the small perturbation model. The inferred dielectric constant values are higher than that of the small-perturbation model (note the different scales), indicating that the Oh et al. algorithm does a better job of taking the effects of surface roughness into account. However, it is clear from the results that this algorithm still fails to completely separate the effects of surface roughness and dielectric constant.

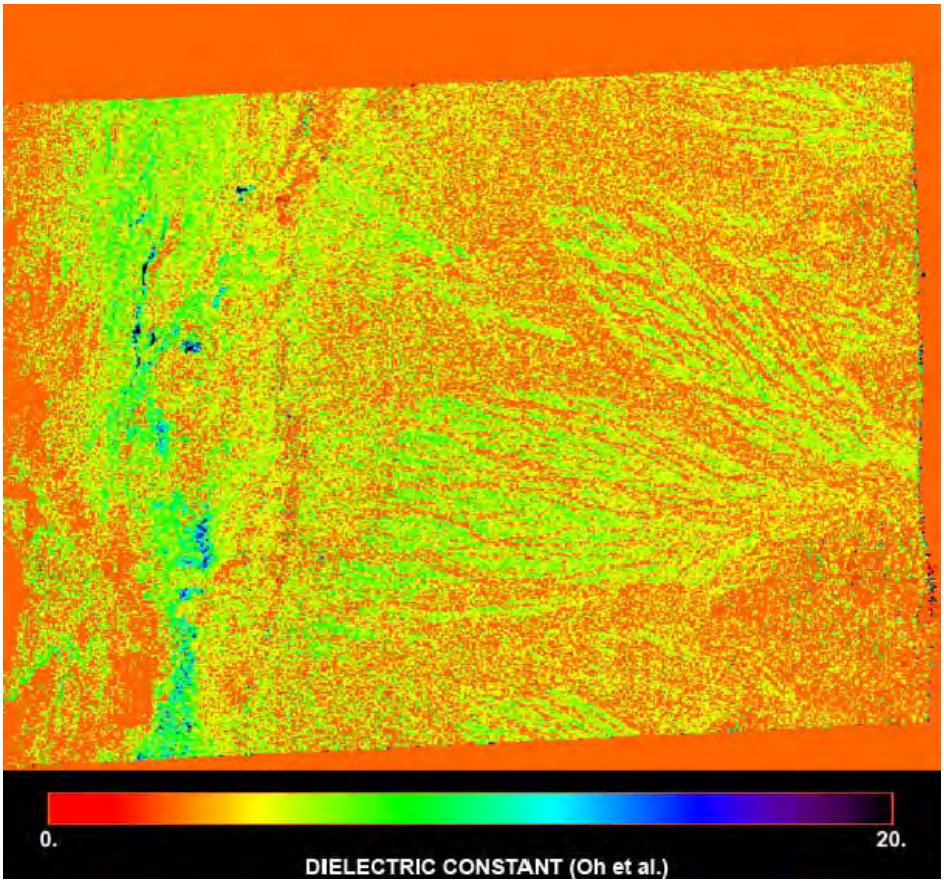

Fig. 5-15. Inversion results using the algorithm proposed by Oh et al. [8]. The algorithm results are affected significantly by the changes in surface roughness, and consistently estimate lower values of dielectric constant for the rougher surfaces.

Figure 5-16 shows the inversion results for the Dubois et al. algorithm [6]. This algorithm clearly does a better job than the others at removing the effects of surface roughness. It also clearly shows that the saline valley floor has a higher dielectric constant than the dry alluvial fan surface. The values of the dielectric constants calculated on the alluvial fan are consistent with dry soils that are covered by desert pavement. Also note that, although quite noisy, the inversion does indicate that the dielectric constant of the active stream channels is slightly higher than that of the fan surface, consistent with having more rocks and boulders and less exposed soil present in the active stream channels.

Figure 5-17 contains the inversion results for the algorithm proposed by Shi et al. (1997) [7]. Note that this algorithm, in contrast to the small-perturbation model, and the Oh et al. [8] algorithm, reports lower dielectric constants on the smoother surfaces than the rougher surfaces. It also fails to report high

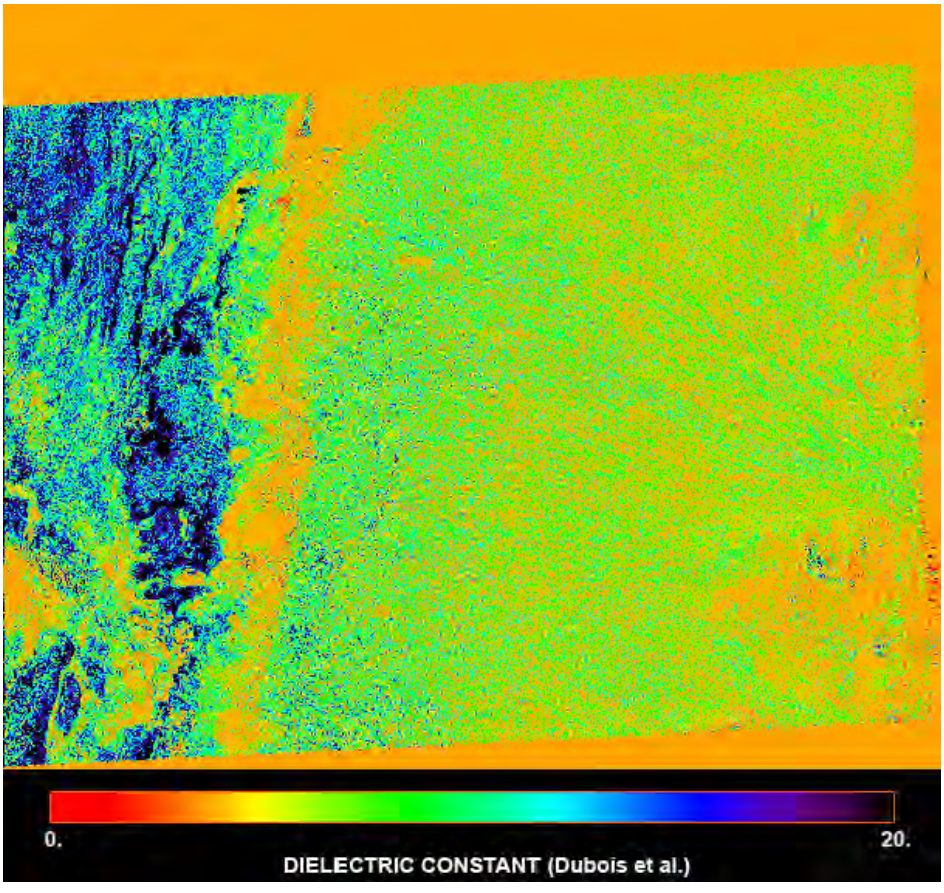

Fig. 5-16. Inversion results using the Dubois et al. algorithm. The algorithm does well at removing the effects of surface roughness. It also does better at indicating the higher dielectric constants of the saline valley floor on the left.

dielectric constants for the saline valley floor. To understand the behavior of this algorithm in the presence of roughness, let us consider the right-hand side of Eq. (5.3-21), repeated below:

$$\frac{|\alpha_{vv}|^2 + |\alpha_{hh}|^2}{(|\alpha_{vv}||\alpha_{hh}|)^{b_{vh}(\theta)}} 10^{-a_{vh}(\theta)/10} = \frac{\sigma^{\circ}_{vv} + \sigma_{hh}}{(\sigma_{vv}\sigma_{hh})^{b_{vh}(\theta)/2}}.$$

Very rough surfaces exhibit co-polarized radar cross-sections that are equal, while slightly rough surfaces exhibit larger VV radar cross-sections than HH. It is, therefore, clear that for these two measurements to become equal, the HH cross-section must increase faster than the VV cross-section with increasing surface roughness in order for the former to "catch up" and become equal to the VV cross-section. This is what the empirical Dubois et al. algorithm [6] shows.

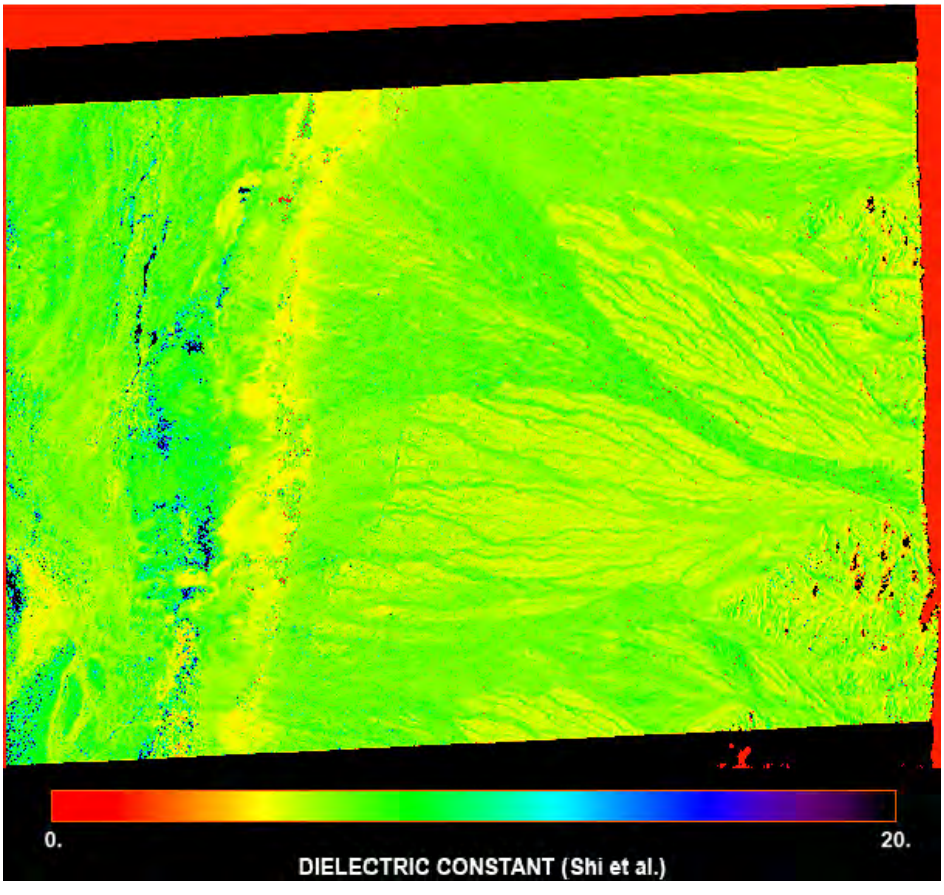

Fig. 5-17. Inversion results for the Shi et al. algorithm [7]. The algorithm seems to over-compensate for roughness, inferring lower values on the smoother surfaces than the rougher surfaces.

To help understand the results in Fig. 5-17, let us assume (as demonstrated by the Dubois et al. results) that

$$\sigma_{hh} \sim (kh)^x; \quad \sigma_{vv} \sim (kh)^y; \quad x \geq y .$$

The right side of Eq. (5.3-21) then becomes

$$\frac{\sigma_{vv} + \sigma_{hh}}{(\sigma_{vv}\sigma_{hh})^{b_{vh}(\theta)/2}} \sim \frac{(kh)^x + (kh)^y}{(kh)^{(x+y)b_{vh}(\theta)/2}} .$$

Neither x nor y are functions of the radar angle of incidence. It follows, therefore, that one could perhaps make the Shi et al. algorithm [7] insensitive to surface roughness at a particular incidence angle; however, this would not be the case at different incidence angles. In practice, however, $b_{vh}(\theta)$ changes slowly with incidence angle, so the sensitivity to roughness does not vary much with incidence angle. If we take the values found by Dubois et al. [6] for x and y and use the value of $b_{vh}(\theta)$ at 45 deg angle of incidence, we find

$$\frac{\sigma_{vv} + \sigma_{hh}}{(\sigma_{vv}\sigma_{hh})^{b_{vh}(\theta)/2}} \sim \frac{(kh)^{1.4} + (kh)^{1.1}}{(kh)^{0.48(1.1+1.4)}} = (kh)^{0.2} + (kh)^{-0.1} .$$

One should, therefore, expect the Shi et al [7] results to be slightly affected by surface roughness.

The next point to investigate is whether this argument results in an over-estimation of the surface dielectric constant in the presence of increased roughness, as Fig. 5-17 indicates. Note that the discussion above shows that the right side of Eq. (5.3-21) increases with increasing surface roughness. The left side of Eq. (5.3-21) is a monotonically increasing function of the surface dielectric constant. Therefore, increasing the right side of Eq. (5.3-21) (artificially) in the presence of surface roughness would, indeed, cause the algorithm to estimate a higher dielectric constant than the actual value.

5.5 Parameterizing Scattering Models

Most scattering models are far too computationally intensive to use in practical inversion algorithms for large images. This is especially the case when the answers are needed on relatively short timescales, such as “near real-time” applications that require soil moisture values as inputs. One way to make this problem more tractable is to use “parameterized” versions of the scattering model with simpler functions that are easily inverted.

To illustrate this process, let us postulate that we can approximate the measured radar cross-section σ_{ij} using $\hat{\sigma}_{ij}$ as follows:

$$10\log\hat{\sigma}_{ij} = A_{ij} + B_{ij} f\left(m_v\right) + C_{ij} g\left(kh\right); \quad i, j = h, v. \tag{5.5-1}$$

Here we use generic functions f and g to denote our hypothesis about the influence of soil moisture and surface roughness on the radar cross-section. The subscript ij refers to the polarization combination used to measure (or in this case simulate) the radar cross-section. We should point out that the coefficients in this function are all functions of the angle of incidence. An example of such a postulate was employed by Dubois et al. (1995) [6], who used the dielectric constant itself as f and the logarithm for g. We typically want to minimize the error between the measured and the estimated radar cross-sections in a least-squares sense. This error for *n* measurements is given by

$$E = \sum_{n=1}^{N}\left(10\log\sigma_{ijn} - 10\log\hat{\sigma}_{ijn}\right)^2 = \sum_{n=1}^{N}\left(10\log\sigma_{ijn} - A_{ij} - B_{ij} f\left(m_{vn}\right) - C_{ij} g\left(kh_n\right)\right)^2. \tag{5.5-2}$$

The solution that minimizes this error is

$$\begin{pmatrix} A_{ij} \\ B_{ij} \\ C_{ij} \end{pmatrix} = \begin{pmatrix} 1 & \langle f \rangle & \langle g \rangle \\ \langle f \rangle & \langle f^2 \rangle & \langle fg \rangle \\ \langle g \rangle & \langle fg \rangle & \langle g^2 \rangle \end{pmatrix}^{-1} \begin{pmatrix} \langle 10\log\sigma_{ij} \rangle \\ \langle 10\log\sigma_{ij} f \rangle \\ \langle 10\log\sigma_{ij} g \rangle \end{pmatrix}, \tag{5.5-3}$$

where the angular brackets $\langle\ \rangle$ denote averaging over all measurements. The question then becomes which functions f and g would provide the best results.

As an example, we use simulated data from the integral equation method at an angle of incidence of 45 deg. We vary the soil moisture from 1 percent to 40 percent and the values of *h* from 0.1 cm to 3 cm. At L-band, this would correspond to values of *kh* that vary from 0.026 to 0.78. We then use different combinations of functions to parameterize the values predicted by the integral equation model.

In the first case, we use $f(m_v) = m_v$. Several other researchers have shown a linear relationship between the logarithm of the radar cross-section and soil moisture (Quesney et al., 2000 [5]). For the function *g*, we follow Dubois et al. (1995) [6] and use the logarithm of *kh*. Using the data described above, we find

$$\begin{aligned} 10\log\hat{\sigma}_{hh} &= -20.17 + 15.33m_v + 13.63\log(kh) \\ 10\log\hat{\sigma}_{vv} &= -18.81 + 25.33m_v + 10.99\log(kh) \end{aligned}. \tag{5.5-4}$$

Note that the HH cross-section increases faster with roughness than the VV, explaining why the difference between HH and VV is observed to be smaller for rougher surfaces than for smoother ones. Conversely, the VV cross-section increases faster with an increase in soil moisture, again explaining why the difference between HH and VV is observed to be larger for wetter surfaces than for drier ones. Also, note that the coefficients for the roughness are very similar to those determined by Dubois et al. (1995) [6], as is shown in Eq. (5.3-13), even though their coefficients were determined from measured data rather than model simulations.

To determine how well these parameterizations approximate the model, we compare the accuracies of the parameterized inversions. We start with simulating 1000 model predictions in which both the surface roughness and the soil moisture are treated as random variables. We then take these 1000 pairs of HH and VV cross-sections and invert them for soil moisture and surface roughness using the expressions for the two parameterizations. We then compare the results of the inversions to the actual random values of soil moisture and surface roughness that went into the simulation.

To invert the parameterizations, we note that (see Eq. (5.5-1)) we can write

$$\begin{aligned} 10\log\hat{\sigma}_{hh} &= \Sigma_{hh} = A_{hh} + B_{hh} f(m_v) + C_{hh} g(kh) \\ 10\log\hat{\sigma}_{vv} &= \Sigma_{vv} = A_{vv} + B_{vv} f(m_v) + C_{vv} g(kh) \end{aligned}. \tag{5.5-5}$$

We can write this in matrix form as follows

$$\begin{pmatrix} B_{hh} & C_{hh} \\ B_{vv} & C_{vv} \end{pmatrix} \begin{pmatrix} f(m_v) \\ g(kh) \end{pmatrix} = \begin{pmatrix} \Sigma_{hh} - A_{hh} \\ \Sigma_{vv} - A_{vv} \end{pmatrix}, \tag{5.5-6}$$

which has the solution

$$\begin{pmatrix} f(m_v) \\ g(kh) \end{pmatrix} = \begin{pmatrix} B_{hh} & C_{hh} \\ B_{vv} & C_{vv} \end{pmatrix}^{-1} \begin{pmatrix} \Sigma_{hh} - A_{hh} \\ \Sigma_{vv} - A_{vv} \end{pmatrix}. \tag{5.5-7}$$

Figure 5-18 shows the results for the inversion. The rms error in estimating the surface roughness is 0.25 cm; the rms error in soil moisture is 5.1 percent.

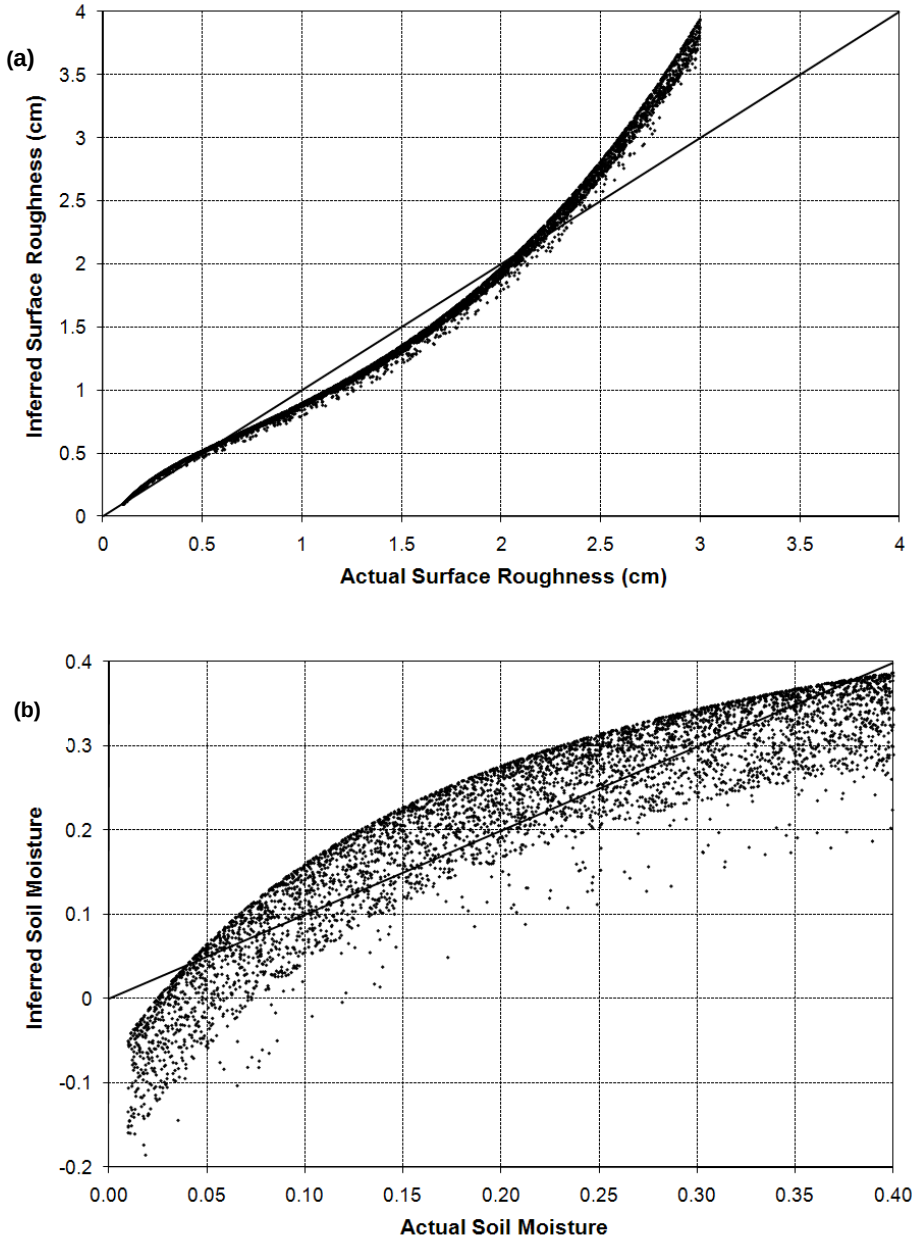

Fig. 5-18. Inversion results for the parameterization shown in Eq. (5.5-4) for (a) surface roughness and (b) soil moisture. The rms error in surface roughness is 0.25 cm; the rms error in soil moisture is 5.1 percent.

Note that particularly the soil moisture is often underestimated. Many of the lower soil moisture cases are inferred to have negative soil moistures. This is a consequence of the linear approximation used for the soil moisture in this parameterization. In fact, the same behavior is observed for the dielectric constant of drier surfaces when using the Dubois et al. (1995) [6] algorithm, as was pointed out by Wang et al. (1995) [33].

As a second case, we use for the function *f* the logarithm of the soil moisture and for *g* the logarithm of *kh*. This choice for the function *f* is an effort to take into account the fact that the radar cross-section is, in fact, a non-linear function of the soil moisture. In this case, we find

$$\begin{aligned} 10\log\hat{\sigma}_{hh} &= -12.88 + 5.23\log(m_v) + 13.63\log(kh) \\ 10\log\hat{\sigma}_{vv} &= -6.87 + 8.51\log(m_v) + 10.99\log(kh) \end{aligned} \quad . \tag{5.5-8}$$

The results for this case are shown in Fig. 5-19. The rms error in surface roughness is 0.26 cm; the rms error in soil moisture is 6.4 percent. While we have removed the negative inferred soil moisture values, there is in the inferred results a larger spread, especially for larger soil moisture values.

These two examples illustrate the difficulty in parameterizing non-linear functions with simple approximations. But is there a way to use these simple functions (which are easy to invert) to achieve better accuracy? The answer lies in using smaller ranges of moisture and surface roughness when making the approximations. As an illustration, let us assume we want to use the first approximation where we use a linear approximation for the soil moisture and a logarithmic approximation for the surface roughness. We shall assume that we want to have an accuracy of 0.1 cm or better for the surface roughness and an accuracy of 1 percent or better for soil moisture over the ranges we assumed before. We can achieve these accuracies if we are willing to break the ranges up into smaller segments. An example is shown below. For $0.01 \le m_v \le 0.1$:

$$\left.\begin{aligned} 10\log\hat{\sigma}_{hh} &= -18.77 + 42.31m_v + 16.46\log(kh) \\ 10\log\hat{\sigma}_{vv} &= -15.86 + 63.18m_v + 16.34\log(kh) \end{aligned}\right\} \text{for } 0.1 \le h \le 0.5$$

$$\left.\begin{aligned} 10\log\hat{\sigma}_{hh} &= -23.13 + 42.31m_v + 12.17\log(kh) \\ 10\log\hat{\sigma}_{vv} &= -21.80 + 63.36m_v + 10.12\log(kh) \end{aligned}\right\} \text{for } 0.5 \le h \le 1.5 \quad . \tag{5.5-9}$$

$$\left.\begin{aligned} 10\log\hat{\sigma}_{hh} &= -21.72 + 42.31m_v + 15.73\log(kh) \\ 10\log\hat{\sigma}_{vv} &= -22.77 + 64.25m_v + 7.82\log(kh) \end{aligned}\right\} \text{for } 1.5 \le h \le 3.0$$

(a)

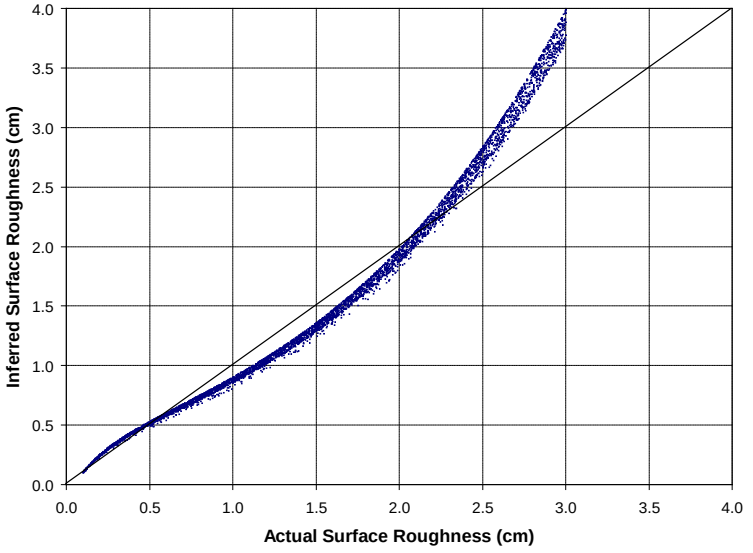

(b)

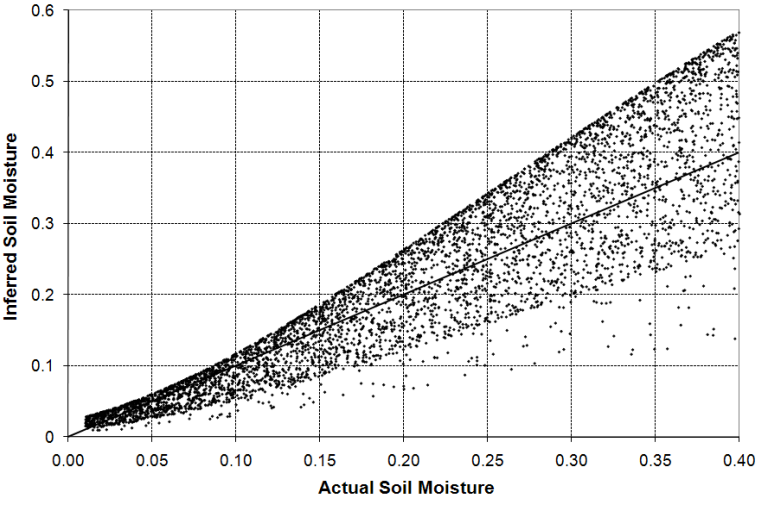

Fig. 5-19. Inversion results for the parameterization shown in Eq. (5.5-8) for (a) actual surface roughness and (b) actual soil moisture. The rms error in surface roughness is 0.26 cm; the rms error in soil moisture is 6.4 percent.

For the range $0.1 \le m_v \le 0.2$:

$$\left.\begin{aligned} 10\log\hat{\sigma}_{hh} &= -16.46 + 17.54m_v + 16.46\log(kh) \\ 10\log\hat{\sigma}_{vv} &= -12.64 + 29.08m_v + 16.34\log(kh) \end{aligned}\right\} \text{for } 0.1 \le h \le 0.5$$
$$\left.\begin{aligned} 10\log\hat{\sigma}_{hh} &= -20.82 + 17.53m_v + 12.17\log(kh) \\ 10\log\hat{\sigma}_{vv} &= -18.54 + 29.14m_v + 10.17\log(kh) \end{aligned}\right\} \text{for } 0.5 \le h \le 1.5 \cdot \qquad (5.5\text{-}10)$$
$$\left.\begin{aligned} 10\log\hat{\sigma}_{hh} &= -19.41 + 17.53m_v + 15.73\log(kh) \\ 10\log\hat{\sigma}_{vv} &= -19.42 + 29.46m_v + 8.11\log(kh) \end{aligned}\right\} \text{for } 1.5 \le h \le 3.0$$

Finally, for the range $0.2 \le m_v \le 0.4$:

$$\left.\begin{aligned} 10\log\hat{\sigma}_{hh} &= -14.37 + 7.32m_v + 16.46\log(kh) \\ 10\log\hat{\sigma}_{vv} &= -9.34 + 12.99m_v + 16.34\log(kh) \end{aligned}\right\} \text{for } 0.1 \le h \le 0.5$$
$$\left.\begin{aligned} 10\log\hat{\sigma}_{hh} &= -18.74 + 7.32m_v + 12.17\log(kh) \\ 10\log\hat{\sigma}_{vv} &= -15.22 + 13.00m_v + 10.19\log(kh) \end{aligned}\right\} \text{for } 0.5 \le h \le 1.5 \cdot \qquad (5.5\text{-}11)$$
$$\left.\begin{aligned} 10\log\hat{\sigma}_{hh} &= -17.32 + 7.32m_v + 15.73\log(kh) \\ 10\log\hat{\sigma}_{vv} &= -16.04 + 13.10m_v + 8.25\log(kh) \end{aligned}\right\} \text{for } 1.5 \le h \le 3.0$$

Note that these boundaries were not optimized; the actual segments were chosen to illustrate the point. The question now is how to invert the measurements using these nine subspaces. We simply use the original set of expressions in Eq. (5.5-4) as a starting point. Based on the results of the inversion, we then use the subspace wherein the initial inversion result fall. We then use the updated set of expressions to perform the inversion. We find that a small number of iterations are generally required to find the best results. In our test, fewer than 10 iterations are typically required for the result to stabilize. The iterations are performed using the results of the previous calculation to decide on which of the nine expressions to use for the next iteration. Once the results change less than a pre-defined amount, we stop the iterations. The results of this scheme are shown in Fig. 5-20. This clearly represents a significant improvement over the single set of expressions.

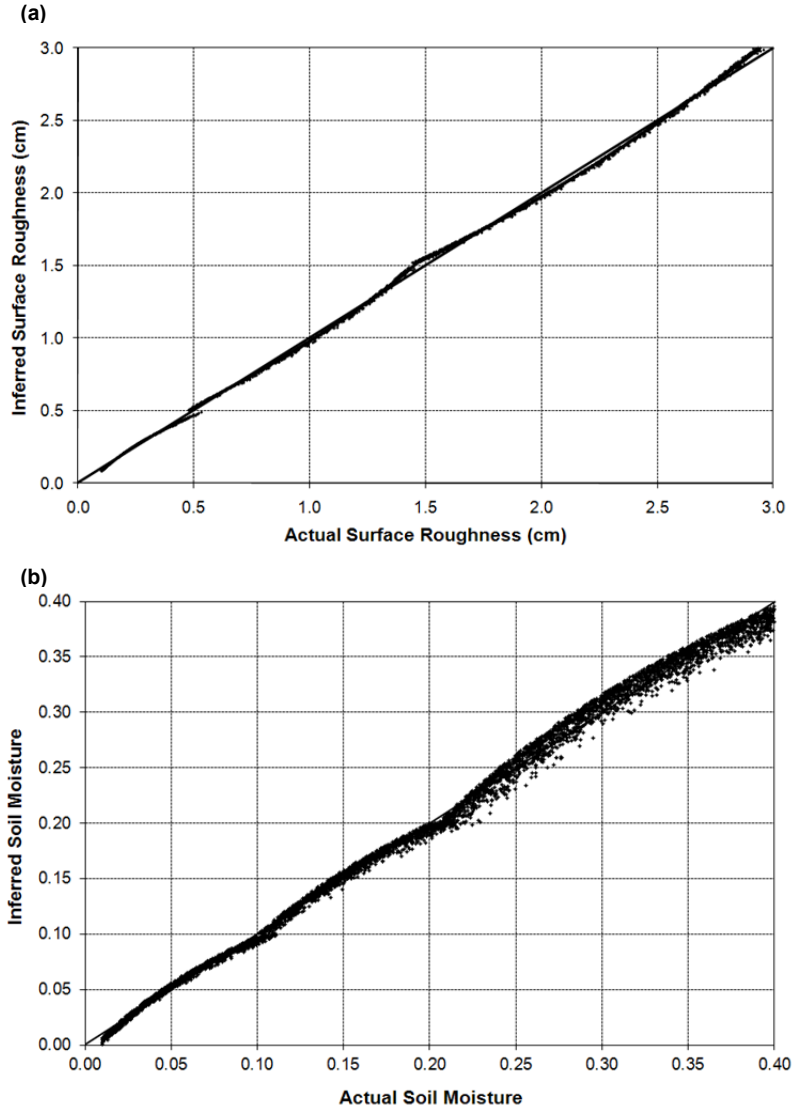

Fig. 5-20. Inversion results for the parameterization that breaks the data space into nine smaller spaces showing (a) inferred surface roughness and (b) inferred soil moisture. The rms error in surface roughness is 0.26 mm, and the rms error in soil moisture is 0.67 percent.

The discussion in this section illustrates the difficulties with parameterizing complicated non-linear expressions with simpler ones. While the inversion might be much more efficiently performed numerically using simple expressions, it is not easy to find a parameterization that is valid over a large range of geophysical variable values. Once we start adding more expressions to

better approximate sub-ranges of the geophysical parameter, the advantages become less clear. With computer capabilities rapidly increasing, direct numerical inversion of the forward radar model is becoming more feasible. We shall explore this in more detail below.

5.6 Inverting the IEM Model

The discussion in the previous section illustrates the difficulty of parameterizing non-linear models, such as the IEM, over a large range of parameters, which, in our case, includes surface roughness, soil moisture, and the angle of incidence. The main advantage of parameterizing such a model is the ease and speed with which the parametrized expressions can be inverted. The price we pay is that the inversion is less accurate.

As computer capabilities grow, however, it might become feasible to "invert" models like the IEM using some merit function to describe how different a simulated and observed result are and to then adjust the input parameters of the simulation to minimize this difference. The obvious advantage is that we no longer have to rely on functions that have a limited range of accuracy. The disadvantage is that the inversion might be much slower than a parameterized case.

To illustrate, we will look at two different approaches. The first approach uses a simple cube of pre-calculated IEM simulations for each polarization combination that is stored on a computer for later use. The inversion then reads the cube of data and uses the values in the cube to estimate the geophysical parameters based on the observed radar cross-sections. The second approach uses the downhill simplex optimization approach to minimize the error between the simulated data and the observed radar cross-sections. These two approaches will be discussed separately below.

For a merit function, we define the rms error between the measured and observed values as follows:

$$E = \sqrt{\left(\sigma_{hh\,obs} - \sigma_{hh\,sim}\right)^2 + \left(\sigma_{vv\,obs} - \sigma_{vv\,sim}\right)^2}\,, \qquad (5.6\text{-}1)$$

where the subscripts *obs* and *sim* refer to the observed and simulated values, respectively. The error function can be extended to include more polarization combinations by simply adding terms inside the square root.

5.6.1 Using a Data Cube

The inversion using a data cube utilizes a previously calculated cube of values for each of the HH and VV radar cross-sections. The three parameters making

up the cube are the surface roughness, the soil moisture, and the angle of incidence. For our illustration, we use a constant ratio of the surface roughness and the surface correlation length. Of course, one could use a four-dimensional data set where the correlation length is explicitly included as one of the parameters. We only have to calculate this data cube once; we can then store the data in a file for later use. For our purposes, we used a cube that is calculated at intervals of 0.5 deg in the angle of incidence, and 512 values in each of the surface roughness and the soil moisture. We allowed the soil moisture and surface roughness values to range over the same values as in the previous section.

When inverting the data, we first calculate the error for the entire data space, using both the HH and VV data cubes. We then select the point where the error is the minimum in the data cube, and interpolate the neighborhood of that point to a finer grid. We then find the minimum error on this finer grid, and report the surface parameters for this point as the inferred ones. The results are shown in Fig. 5-21. The rms error for the surface roughness is 0.0009 cm; and the rms error for the soil moisture is 0.06 percent.

Considering the results in Fig. 5-21, we notice that the soil moisture error is larger for the larger absolute values of the soil moisture. This can be seen by the larger spread of the values in the upper left side of the figure on the right in Fig. 5-21. This is a consequence of the fact that the radar cross-sections saturate as the moisture values become larger. In that case, a small error in roughness estimation leads to a larger error in soil moisture. Everything considered, however, these results are excellent.

The results in Fig. 5-21 were calculated for a fixed angle of incidence of 40 deg. We repeated the experiment by randomly varying the angle of incidence as well as the roughness and soil moisture values. When inverting the simulated data, we assume we know the angle of incidence. We then interpolate linearly between the two closest planes in the HH and VV data cubes to generate two data sets for that angle of incidence. These data sets are then used to invert the simulated data. The results are shown in Fig. 5-22.

Very similar results are found when using the downhill simplex method to invert the IEM model. Both these methods provide excellent results, but they come at the price of increase computational complexity. Even the cube method takes about an order of magnitude longer to invert than the simple parameterized models.

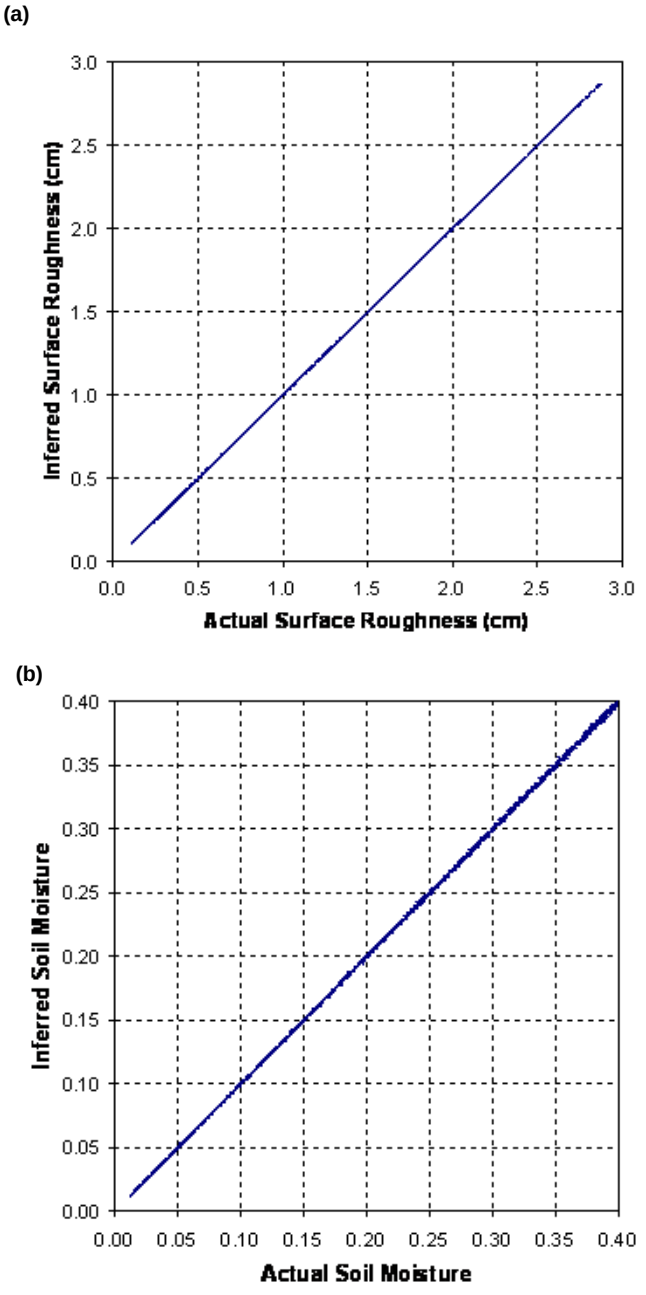

Fig. 5-21. Inversion results using a data space with 512 values for each of the (a) surface roughness and (b) soil moisture. The rms error in surface roughness is 0.009 mm, and the rms error in soil moisture is 0.06 percent. The results are shown for 5000 simulations, with random roughness and moisture values at a fixed angle of incidence of 40 deg.

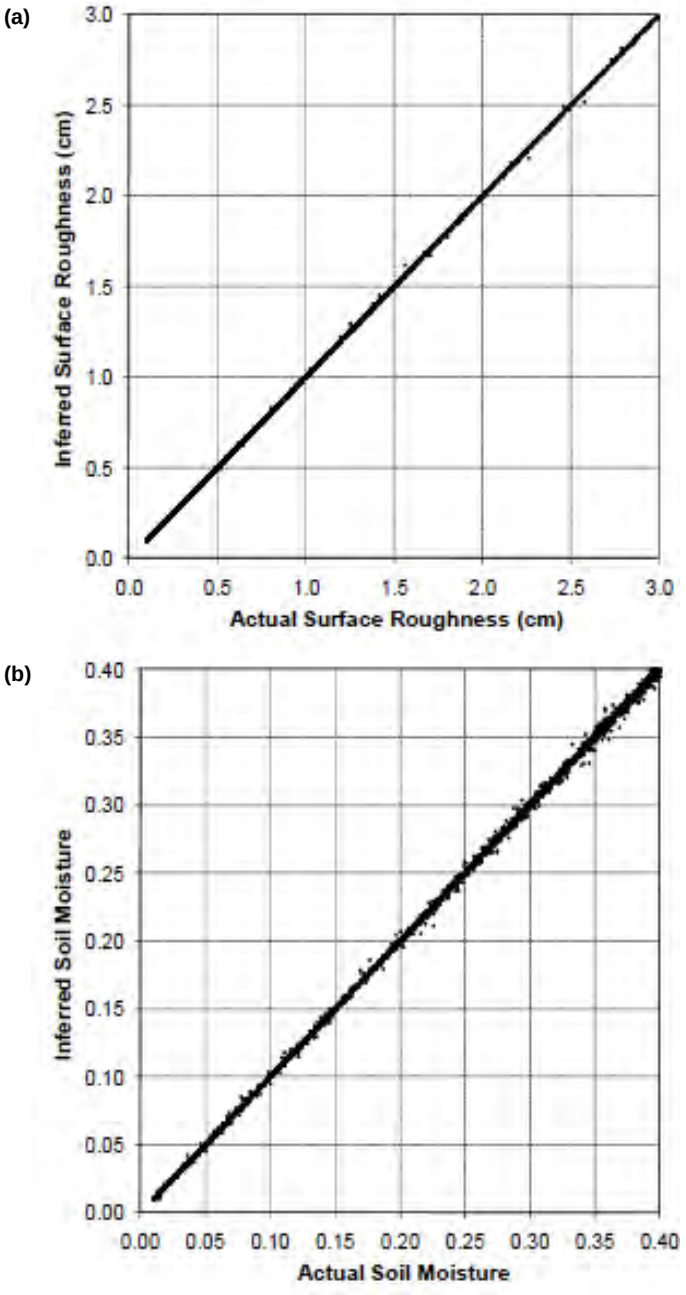

Fig. 5-22. Inversion results using a data space with 512 values for each of the (a) surface roughness and (b) soil moisture. The rms error in surface roughness is 0.03 mm, and the rms error in soil moisture is 0.16%. The results are shown for 5000 simulations with random roughness and moisture values and random incidence angles between 10 and 60 deg.

5.7 Scattering from Vegetated Terrain

Estimating soil moisture from vegetated terrain is significantly more complicated than the bare surface case. Unfortunately, however, much of the earth's surface is covered by some vegetation, so the bare surface approach has limited application. Here we shall discuss briefly how models for backscattering from vegetated terrains are constructed, and then show how these models can aid in estimating soil moisture in vegetated terrain.

Here we shall illustrate the modeling approach using a single layer vegetation model. This type of model would be used to describe scattering from pasture land, grasslands, most agriculture crops and shrubs. To model forest canopies, one or two more layers of vegetation would be added as described by Durden et al. (1989) [34].

The vegetation layer will be modeled assuming that there are two interfaces to consider (see Fig. 5-23): 1) vegetation layer, and 2) the underlying ground surface. The vegetation layer is comprised of primary scatterers, and possibly secondary scatterers. For example, the primary scatterers may be stalks in the case of corn, while the secondary scatterers may be the leaves. In the case of pasture, we will typically use only primary scatterers.

The vegetation layer has a thickness b. Each component of the vegetation (primary and secondary scatterers) is characterized by a dielectric constant $(\varepsilon_p, \varepsilon_s)$, radius (a_p, a_s), length (l_p, l_s), density (ρ_p, ρ_s) and a probability density function ($p_p(\theta_c, \phi_c), p_s(\theta_c, \phi_c)$) describing the statistical distribution of the orientation of the cylinders used to represent the component. The ground surface is characterized by a dielectric constant ε_g, rms. height h, correlation length l_g. The small-scale slopes (s_l) describe the micro-roughness of the

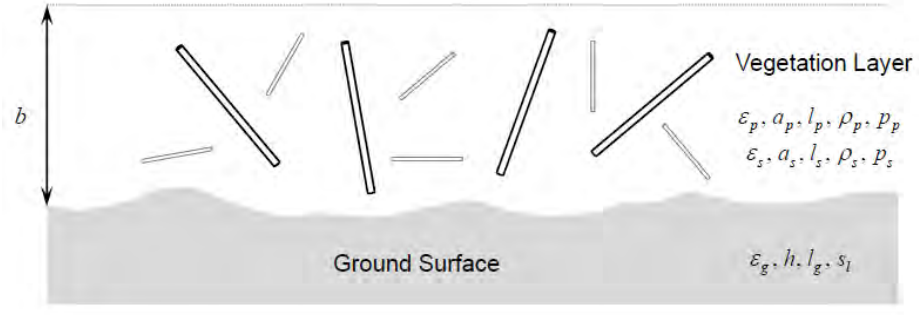

Fig. 5-23. The vegetation is assumed to consist of a layer of randomly oriented scatterers.

surface and are related to the rms. height and the correlation length of the ground surface, which is assumed to have an exponential correlation function.

Central to this type of modeling is the bistatic scattering matrix of a dielectric cylinder. Other types of scatterers often found in vegetation modeling include dielectric disks which are used to model larger flat leaves. Appendix B lists the expressions for scattering from a dielectric cylinder with arbitrary orientation.

There are several possible scattering paths to consider (see Fig. 5-24): 1) direct backscattering from the vegetation elements, 2) specular scattering at the ground surface, followed by bistatic scattering at the vegetation element, 3) bistatic scattering at the vegetation element, followed by specular scattering at the ground surface, and 4) backscattering from the underlying ground surface. For each path, the wave incident on a scatterer in the vegetation traveled through the vegetation between the scatterer and the radar before it reaches the scatterer, and suffered some attenuation as a result. Also, because the vegetation elements are assumed to be longer than the wavelength, the scattering centers in the different paths will in general be separated by several wavelengths. This implies that any phase relationships between the different scattering paths will be uniformly random, meaning that the resulting scattered powers will add incoherently. The exception is cases 2 and 3, which are exactly the same path, but in opposite directions. In that case, there will be a deterministic phase relationship between the two paths, which means the signals will add coherently. We shall now discuss each of these scattering terms separately.

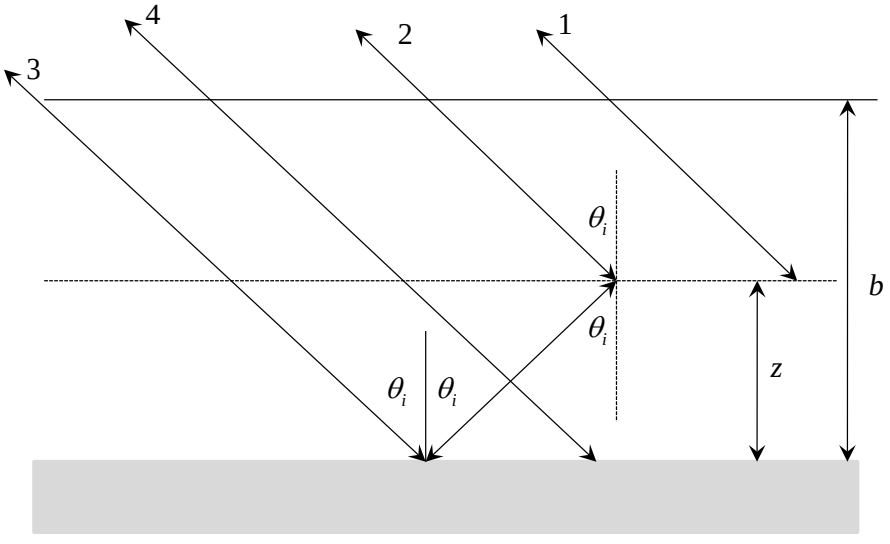

Fig. 5-24. Scattering paths to consider for a single layer vegetation model. See the text for details.

5.7.1 Scattering from the Vegetation Layer (Scattering Path 1)

The next step is to calculate the scattering coefficients from a layer randomly oriented scatterers. We shall model this by assuming that the scatterers are oriented according to a statistical distribution function that is given by $p(\theta_c,\phi_c)$. By definition,

$$\int_0^{2\pi}\int_0^{\pi} p(\theta_c,\phi_c)\sin\theta_c\, d\theta_c\, d\phi_c = 1 \tag{5.7-1}$$

Our interest is in calculating the backscattering radar cross-section of this layer, as well as the transmission coefficient for this layer. The latter is important in calculating the reflection from the underlying ground surface after the signals have propagated through the vegetation layer.

First, let us consider a scatterer that is at a height *z* above the ground surface inside the vegetation layer as shown in Figure 5-24. The wave incident on this scatterer has already propagated a distance

$$d(z) = \frac{b-z}{\cos\theta_i} \tag{5.7-2}$$

through part of the layer before reaching the scatterer. The strength of the electric field incident on this scatterer is therefore

$$\begin{pmatrix} E_h \\ E_v \end{pmatrix}^{isc} = \begin{pmatrix} e^{-\tau_h(b-z)} & 0 \\ 0 & e^{-\tau_v(b-z)} \end{pmatrix} \begin{pmatrix} E_h \\ E_v \end{pmatrix}^{inc} = \left[\boldsymbol{\alpha}(b-z)\right] \begin{pmatrix} E_h \\ E_v \end{pmatrix}^{inc} \tag{5.7-3}$$

Here the superscript *isc* refers to the wave incident on the scatterer, while *inc* refers to the wave incident on the vegetation layer. Also,

$$\tau_p(b-z) = \frac{\kappa_p^e(b-z)}{\cos\theta_i} \tag{5.7-4}$$

The extinction coefficients are average extinction coefficients as defined in Appendix B and takes into account the average extinction between the scatterer and the top of the layer. This wave is now scattered by the scatterer. In the backscatter direction, the scattering matrix of the scatterer is (see Appendix B)

$$\mathbf{S}(\theta_i,\phi_i,\theta_s=\theta_i,\phi_s=\phi_i,\theta_c,\phi_c) = \begin{pmatrix} \mathbf{h}_s\cdot\mathbf{h}_s' & \mathbf{h}_s\cdot\mathbf{v}_s' \\ \mathbf{v}_s\cdot\mathbf{h}_s' & \mathbf{v}_s\cdot\mathbf{v}_s' \end{pmatrix} \mathbf{S}(\theta_{ic},\phi_{ic},\theta_{sc},\phi_{sc}) \begin{pmatrix} \mathbf{h}_i\cdot\mathbf{h}_i' & \mathbf{v}_i\cdot\mathbf{h}_i' \\ \mathbf{h}_i\cdot\mathbf{v}_i' & \mathbf{v}_i\cdot\mathbf{v}_i' \end{pmatrix} \tag{5.7-5}$$

After being scattered, the wave again propagates through the vegetation layer to the top before returning to the radar while being attenuated as shown in Eq. (5.7-3). Adding all these terms together, we find the scattering matrix of the scatterer, as seen from outside the layer, as

$$\mathbf{S}_{veg}\left(\theta_i,\phi_i,\theta_s,\phi_s,\theta_c,\phi_c,z\right)=\left[\boldsymbol{\alpha}\left(b-z\right)\right]\mathbf{S}\left(\theta_i,\phi_i,\theta_s,\phi_s,\theta_c,\phi_c\right)\left[\boldsymbol{\alpha}\left(b-z\right)\right] \tag{5.7-6}$$

The radar cross-section is derived from the elements of the covariance matrix, which for the backscatter case, are defined by

$$\boldsymbol{\Sigma}_{veg}\left(\theta_i,\phi_i,\theta_s=\theta_i,\phi_s=\phi_i,\theta_c,\phi_c,z\right)=\begin{pmatrix} S_{hh}S_{hh}^{*} & \sqrt{2}S_{hh}S_{hv}^{*} & S_{hh}S_{vv}^{*} \\ \sqrt{2}S_{hv}S_{hh}^{*} & 2S_{hv}S_{hv}^{*} & \sqrt{2}S_{hv}S_{vv}^{*} \\ S_{vv}S_{hh}^{*} & \sqrt{2}S_{vv}S_{hv}^{*} & S_{vv}S_{vv}^{*} \end{pmatrix}_{veg} \tag{5.7-7}$$

We note that if we expand the expression on the right in Eq. (5.7-6), we find that we can write the covariance matrix as

$$\boldsymbol{\Sigma}_{veg}\left(\theta_i,\phi_i,\theta_s=\theta_i,\phi_s=\phi_i,\theta_c,\phi_c,z\right)=\mathbf{K}\left(b-z\right)\boldsymbol{\Sigma}_{veg}\left(\theta_i,\phi_i,\theta_s,\phi_s,\theta_c,\phi_c\right)\mathbf{K}\left(b-z\right) \tag{5.7-8}$$

where

$$\mathbf{K}\left(z\right)=\begin{pmatrix} e^{-2\tau_h(b-z)} & 0 & 0 \\ 0 & e^{-\left(\tau_h(b-z)+\tau_v(b-z)\right)} & 0 \\ 0 & 0 & e^{-2\tau_v(b-z)} \end{pmatrix}=\begin{pmatrix} K_{hh} & 0 & 0 \\ 0 & K_{hv} & 0 \\ 0 & 0 & K_{vv} \end{pmatrix} \tag{5.7-9}$$

The average backscatter covariance matrix is found by calculating the ensemble average for the scatterer over all possible orientations. Note that only the inner matrices on the right-hand side of Eq. (5.7-6) and Eq. (5.7-9) are functions of the orientation of the scatterer. The average covariance matrix is then

$$\left\langle\boldsymbol{\Sigma}_{veg}\left(\theta_i,\phi_i,z\right)\right\rangle=\int_0^{2\pi}\int_0^{\pi}\boldsymbol{\Sigma}_{veg}\left(\theta_i,\phi_i,\theta_s=\theta_i,\phi_s=\phi_i,\theta_c,\phi_c,z\right)p\left(\theta_c,\phi_c\right)\sin\theta_c\,d\theta_c\,d\phi_c \tag{5.7-10}$$

Similarly, the average optical depth is found from

$$\tau_p\left(b-z\right)=\int_z^b\frac{\rho_s\left(\zeta\right)}{\cos\theta_i}\int_0^{2\pi}\int_0^{\pi}\frac{2\pi}{k_0}\mathrm{Im}\left[S_{pp}\left(\theta_i,\phi_i,\pi-\theta_i,\phi_i+\pi,\theta_c,\phi_c\right)\right]p\left(\theta_c,\phi_c\right)\sin\theta_c\,d\theta_c\,d\phi_c d\zeta \tag{5.7-11}$$

where $\rho_s(z)$ is the density of the scatterers in scatterers$/m^3$ at a height z above the ground. The final step is now to integrate the contribution from all the scatterers in the layer. This is gives

$$\left\langle \boldsymbol{\Sigma}_{veg}(\theta_i,\phi_i)\right\rangle = \int_0^b \left\langle \boldsymbol{\Sigma}_{veg}(\theta_i,\phi_i,z)\right\rangle \rho_s(z)\,dz \tag{5.7-12}$$

From Eq. (5.7-8) we can show that the average covariance matrix has the form

$$\left\langle \boldsymbol{\Sigma}_{veg}(\theta_i,\phi_i,z)\right\rangle = \begin{pmatrix} \left\langle S_{hh}S_{hh}^*\right\rangle K_{hh}K_{hh} & \left\langle \sqrt{2}S_{hh}S_{hv}^*\right\rangle K_{hh}K_{hv} & \left\langle S_{hh}S_{vv}^*\right\rangle K_{hh}K_{vv} \\ \left\langle \sqrt{2}S_{hv}S_{hh}^*\right\rangle K_{hh}K_{hv} & \left\langle 2S_{hv}S_{hv}^*\right\rangle K_{hv}K_{hv} & \left\langle \sqrt{2}S_{hv}S_{vv}^*\right\rangle K_{hv}K_{vv} \\ \left\langle S_{vv}S_{hh}^*\right\rangle K_{hh}K_{vv} & \left\langle \sqrt{2}S_{vv}S_{hv}^*\right\rangle K_{hv}K_{vv} & \left\langle S_{vv}S_{vv}^*\right\rangle K_{vv}K_{vv} \end{pmatrix} \tag{5.7-13}$$

If we assume the density of the scatterers to be uniform in elevation above the ground surface, then only the K terms are functions of z, and we find

$$\begin{aligned}
&\int_0^b \rho_s K_{hh}K_{hh}\,dz = \int_0^b \rho_s e^{-4\tau_h(b-z)}dz = \frac{b\rho_s\cos\theta_i}{4\tau_{hm}}\left\{1-e^{-4\tau_{hm}/\cos\theta_i}\right\} \\
&\int_0^b \rho_s K_{vv}K_{vv}\,dz = \int_0^b \rho_s e^{-4\tau_v(b-z)}dz = \frac{b\rho_s\cos\theta_i}{4\tau_{vm}}\left\{1-e^{-4\tau_{vm}/\cos\theta_i}\right\} \\
&\int_0^b \rho_s K_{hv}K_{hv}\,dz = \int_0^b \rho_s e^{-2\left[\tau_h(b-z)+\tau_v(b-z)\right]}dz = \frac{b\rho_s\cos\theta_i}{(2\tau_{hm}+2\tau_{vm})}\left\{1-e^{-(2\tau_{hm}+2\tau_{vm})/\cos\theta_i}\right\} \\
&\int_0^b \rho_s K_{hh}K_{hv}\,dz = \int_0^b \rho_s e^{-\left[3\tau_h(b-z)+\tau_v(b-z)\right]}dz = \frac{b\rho_s\cos\theta_i}{(3\tau_{hm}+\tau_{vm})}\left\{1-e^{-(3\tau_{hm}+\tau_{vm})/\cos\theta_i}\right\} \\
&\int_0^b \rho_s K_{hv}K_{vv}\,dz = \int_0^b \rho_s e^{-\left[\tau_h(b-z)+3\tau_v(b-z)\right]}dz = \frac{b\rho_s\cos\theta_i}{(\tau_{hm}+3\tau_{vm})}\left\{1-e^{-(\tau_{hm}+3\tau_{vm})/\cos\theta_i}\right\}
\end{aligned} \tag{5.7-14}$$

Here we used the short-hand notations

$$\tau_{hm} = \kappa_h^e b;\ \tau_{vm} = \kappa_v^e b \tag{5.7-15}$$

which represent the total vertical optical path depths of the layer for the two polarizations. The radar cross-section is defined as

$$\boldsymbol{\sigma}_{veg} = 4\pi\left\langle \boldsymbol{\Sigma}_{veg}(\theta_i,\phi_i)\right\rangle \tag{5.7-16}$$

At this point it is instructive to look at the behavior of the vegetation layer in two extreme cases. First, when the optical depth is large, the second terms in Eq. (5.7-14) vanish, and the total scattering (apart from the strength of the covariance matrix terms) approach a constant value. For example, in the case of HH scattering, this constant value can be written as

$$\sigma_{hh} = 4\pi \frac{b\rho_s \cos\theta_i}{4\tau_{hm}} \left\langle S_{hh} S_{hh}^* \right\rangle \tag{5.7-17}$$

In the other extreme, the layer optical depth is small enough that we can replace the exponential by a Taylor series expansion. In that case, the radar cross-section becomes

$$\sigma_{hh} = 4\pi \frac{b\rho_s \cos\theta_i}{4\tau_{hm}} \times \frac{4\tau_{hm}}{\cos\theta_i} \left\langle S_{hh} S_{hh}^* \right\rangle = 4\pi b \rho_s \left\langle S_{hh} S_{hh}^* \right\rangle \tag{5.7-18}$$

To first order, the backscatter from the layer is directly proportional to the density of the scatterers and the thickness of the layer.

All these expressions involving scattering from cylinders are functions of the dielectric constant of the cylinder. We used the expressions reported by Ulaby and El-Rayes (1987) [35] for the vegetation dielectric constant, which is given by

$$\varepsilon_v = \varepsilon_r + v_{fw}\varepsilon_f + v_b \varepsilon_b \tag{5.7-19}$$

In this expression, ε_r is the non-dispersive residual part of the dielectric constant. They report that in terms of the soil volumetric water content M_v, this quantity is given by

$$\varepsilon_r = 1.7 + 3.2 M_v + 6.5 M_v^2 \tag{5.7-20}$$

The dielectric constant of free water is

$$\varepsilon_f = 4.9 + \frac{75}{1 + j\, f/18} - j\frac{18\sigma_{sal}}{f} \tag{5.7-21}$$

Where f is the frequency in Gigahertz, and σ_{sal} is related to the salinity of the water S (measured in parts per thousand on a weight basis) by

$$\sigma_{sal} = 0.16S - 0.0013S^2 \tag{5.7-22}$$

The dielectric constant of bound water is

$$\varepsilon_b = 2.9 + \frac{55}{1+\sqrt{j\,f/0.18}} \tag{5.7-23}$$

The volume fraction of free water is

$$v_{fw} = M_v\left(0.82M_v + 0.166\right) \tag{5.7-24}$$

And the volume fraction of vegetation-bound water is

$$v_b = \frac{31.4M_v^2}{1+59.5M_v^2} \tag{5.7-25}$$

We shall express our simulations in terms of the vegetation volumetric moisture M_v and use the expressions above to calculate the dielectric constant.

5.7.2 Backscatter from the Underlying Ground Surface (Scattering Path 4)

The electromagnetic wave incident upon the ground surface travels through the entire vegetation layer before reaching the ground surface. As it does so, it is attenuated according to

$$\begin{pmatrix} E_h \\ E_v \end{pmatrix}^{igr} = \begin{pmatrix} e^{-\tau_{hm}/\cos\theta_i} & 0 \\ 0 & e^{-\tau_{vm}/\cos\theta_i} \end{pmatrix} \begin{pmatrix} E_h \\ E_v \end{pmatrix}^{inc} \tag{5.7-26}$$

This wave is incident upon the ground element. To calculate the scattering from this element, we shall assume that the scattering from the ground surface can be described by the small perturbation model, in which the scattering matrix for an untilted ground surface is given by

$$\begin{pmatrix} E_h \\ E_v \end{pmatrix}^{sc} = \begin{pmatrix} S_{hh'g} & 0 \\ 0 & S_{vv'g} \end{pmatrix} \begin{pmatrix} E_{h'} \\ E_{v'} \end{pmatrix}^{igr} \tag{5.7-27}$$

where

$$S_{hh'g} = k^2 h\cos^2\theta_i \alpha_{hh}\left(\varepsilon_g, \theta_i\right)\sqrt{W\left(2k\sin\theta_i\right)}\,, \tag{5.7-28}$$

$$S_{vv'g} = k^2 h\cos^2\theta_i \alpha_{vv}\left(\varepsilon_g, \theta_i\right)\sqrt{W\left(2k\sin\theta_i\right)}\,, \tag{5.7-29}$$

and

$$\alpha_{hh}\left(\varepsilon_g,\theta_i\right)=\frac{(\varepsilon_g-1)}{(\cos\theta_i+\sqrt{\varepsilon_g-\sin^2\theta_i})^2}, \tag{5.7-30}$$

$$\alpha_{vv}\left(\varepsilon_g,\theta_i\right)=\frac{(\varepsilon_g-1)\left[\left(\varepsilon_g-1\right)\sin^2\theta_i+\varepsilon_g\right]}{(\varepsilon_g\cos\theta_i+\sqrt{\varepsilon_g-\sin^2\theta_i})^2}, \tag{5.7-31}$$

$$W\left(2k\sin\theta_i\right)=\frac{2l_g^2}{\pi\left[1+4^2k^2l_g^2\sin^2\theta_i\right]^{3/2}}. \tag{5.7-32}$$

The roughness spectrum W given in Eq. (5.7-32) is that of a surface with an exponential correlation function with a correlation length l_g.

After scattering from the ground surface the wave travels again through the vegetation layer before returning to the radar, suffering attenuation given by Eq. (5.7-26) in the process. The covariance matrix of the ground layer is then

$$\left[\boldsymbol{\sigma}_g\right]=4\pi\begin{pmatrix} S_{hh'g}S_{hh'g}^{*}\,e^{-4\tau_{hm}/\cos\theta_i} & 0 & S_{hh'g}S_{vv'g}^{*}\,e^{-2\left(\tau_{hm}+\tau_{vm}\right)/\cos\theta_i} \\ 0 & 0 & 0 \\ S_{vv'g}S_{hh'g}^{*}\,e^{-2\left(\tau_{hm}+\tau_{vm}\right)/\cos\theta_i} & 0 & S_{vv'g}S_{vv'g}^{*}\,e^{-4\tau_{vm}/\cos\theta_i} \end{pmatrix} \tag{5.7-33}$$

This expression is true if we use the first order small perturbation model to represent the ground scattering. If higher order approximations are included, additional terms appear in this matrix, particularly in the cross-polarized element.

5.7.3 Double Reflection Scattering (Scattering Paths 2 and 3)

The next term to consider is the double reflection from a cylinder to the ground surface and back to the radar. This term involves calculating the product of the bistatic scattering matrix of the vegetation layer and the specular scattering matrix of the ground layer. Here we shall only consider the case of a flat ground surface. For a tilted surface, additional terms need to be considered; please see van Zyl (1993) [36] for details.

Consider a scatterer at a height $z<b$ inside the vegetation layer as shown in Figure 5-24. The incident wave is scattered as shown towards the ground surface where it is reflected in the specular direction after which it propagates through the entire vegetation layer back to the radar. The opposite path also

needs to be considered. In this case, the incident wave first travels through the entire vegetation layer to reach the ground surface where it is reflected in the specular direction. The reflected wave then propagates through part of the layer before it is scattered by the scatterer back in the direction of the radar. As the scattered wave propagates back to the radar, it again travels through part of the vegetation layer before reaching the radar.

Let us first consider the path that interacts with the ground surface first. It is well known that the specular ray for a facet characterized by a surface normal $\mathbf{n}$ and light incident along a unit vector $\mathbf{k}_i$ is given by

$$\mathbf{r} = \mathbf{k}_i - 2\left(\mathbf{k}_i \cdot \mathbf{n}\right)\mathbf{n} \tag{5.7-34}$$

Note that $\mathbf{r}$ as given in Eq. (5.7-34) must be expressed in the forward scattering alignment coordinate system. The scattered wave propagation vector in the backscatter alignment coordinate system that we are using is the negative of $\mathbf{r}$. At the ground surface, the incident and scattered propagation vectors are therefore

$$\mathbf{k}_{igs1} = \mathbf{k}_i; \quad \mathbf{k}_{sgs1} = -\mathbf{r} = 2\left(\mathbf{n} \cdot \mathbf{k}_i\right)\mathbf{n} - \mathbf{k}_i \tag{5.7-35}$$

The wave that is reflected in the specular direction from the ground is now incident upon the cylinder representing the vegetation, from which the scattered wave has to propagate back to the radar. This bistatic scattering at the cylinder is therefore characterized by incident and scattered wave propagation vectors

$$\mathbf{k}_{icb1} = \mathbf{r} = \mathbf{k}_i - 2\left(\mathbf{n} \cdot \mathbf{k}_i\right)\mathbf{n}; \quad \mathbf{k}_{scb1} = \mathbf{k}_i \tag{5.7-36}$$

where the subscript c is added to indicate that these refer to the cylinder. Note that Fig. 5-24 shows specular reflection at the layer inside the vegetation. This shows the propagation paths, and does not mean there is specular reflection at the cylinder itself. Since the cylinder may have any orientation, in general we have bistatic scattering at the cylinder.

Finally, for the case of bistatic scattering at the cylinder, followed by specular reflection at the ground, these are

$$\begin{aligned} &\mathbf{k}_{icb2} = \mathbf{k}_i; \quad \mathbf{k}_{scb2} = \mathbf{r} = \mathbf{k}_i - 2\left(\mathbf{n} \cdot \mathbf{k}_i\right)\mathbf{n} \\ &\mathbf{k}_{igs2} = -\mathbf{r} = 2\left(\mathbf{n} \cdot \mathbf{k}_i\right)\mathbf{n} - \mathbf{k}_i; \quad \mathbf{k}_{sgs2} = \mathbf{k}_i \end{aligned} \tag{5.7-37}$$

Figure 5-25 shows the scattering paths for specular scattering at the ground followed by bistatic scattering at the cylinder and vice versa.

For the ground surface, the bistatic scattering matrix describing the specular reflection can be written as

$$\mathbf{R}_g\left(\theta_i,\phi_i,\theta_s,\phi_s\right)=\begin{pmatrix} R_h\left(\varepsilon_g,\theta_i\right) & 0 \\ 0 & R_v\left(\varepsilon_g,\theta_i\right)\end{pmatrix} e^{-2k^2h^2/\cos^2\theta_i} \tag{5.7-38}$$

The two Fresnel reflections coefficients are

$$R_h\left(\varepsilon_g,\theta_i\right)=\frac{\cos\theta_i-\sqrt{\varepsilon_g-\sin^2\theta_i}}{\cos\theta_i+\sqrt{\varepsilon_g-\sin^2\theta_i}} \tag{5.7-39}$$

and

$$R_v\left(\varepsilon_g,\theta_i\right)=-\frac{\varepsilon_g\cos\theta_i-\sqrt{\varepsilon_g-\sin^2\theta_i}}{\varepsilon_g\cos\theta_i+\sqrt{\varepsilon_g-\sin^2\theta_i}} \tag{5.7-40}$$

The scattering matrix for the case that involves scattering at the ground first, can be written as

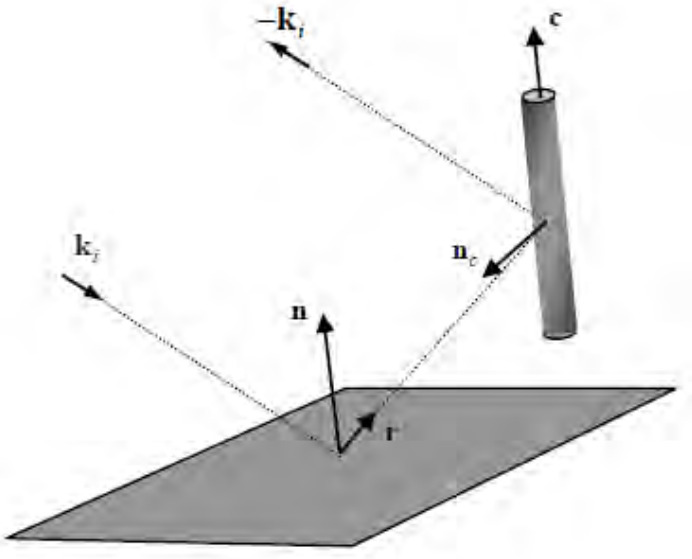

Fig. 5-25. Scattering paths for the double reflection cases.

$$\mathbf{S}_{gc2} = \begin{bmatrix} \quad (b-z) \end{bmatrix} \begin{pmatrix} S_{hhc}^{b} & S_{hvc}^{b} \\ S_{vhc}^{b} & S_{vvc}^{b} \end{pmatrix} \begin{bmatrix} \quad (z) \end{bmatrix} \begin{pmatrix} -1 & 0 \\ 0 & 1 \end{pmatrix} \mathbf{R} \begin{bmatrix} \boldsymbol{\alpha}_{\quad g} \end{bmatrix} \begin{bmatrix} \quad (b) \end{bmatrix} \tag{5.7-41}$$

The number 2 in the subscript refers to the scattering path in Fig. 5-24. The matrix in the middle of the right-hand side of these expressions is needed to take into account that each of the other matrices is described in the backscatter alignment system. The term involving scattering at the cylinder first is

$$\mathbf{S}_{g3} = \begin{bmatrix} \mathbf{R}(b) \end{bmatrix} \begin{bmatrix} \boldsymbol{\alpha}_{\quad g} \end{bmatrix} \begin{bmatrix} \quad (z) \end{bmatrix} \begin{pmatrix} -1 & 0 \\ 0 & 1 \end{pmatrix} \begin{pmatrix} S_{hhc}^{b'} & S_{hvc}^{b'} \\ S_{vhc}^{b'} & S_{vvc}^{b'} \end{pmatrix} \begin{bmatrix} \quad (b-z) \end{bmatrix} \tag{5.7-42}$$

Each of the matrices describing the scattering at the cylinder in Eq. (5.7-41) and Eq. (5.7-42) is of the form (see Appendix B)

$$\begin{pmatrix} S_{hhc}^{y} & S_{hvc}^{y} \\ S_{vhc}^{y} & S_{vvc}^{y} \end{pmatrix} = \begin{pmatrix} \mathbf{h}_s \cdot \mathbf{h}_s' & -\mathbf{v}_s \cdot \mathbf{h}_s' \\ \mathbf{v}_s \cdot \mathbf{h}_s' & \mathbf{h}_s \cdot \mathbf{h}_s' \end{pmatrix} \begin{pmatrix} S_{hhc} & S_{hvc} \\ S_{hvc} & S_{vvc} \end{pmatrix} \begin{pmatrix} \mathbf{h}_i \cdot \mathbf{h}_i' & \mathbf{v}_i \cdot \mathbf{h}_i' \\ -\mathbf{v}_i \cdot \mathbf{h}_i' & \mathbf{h}_i \cdot \mathbf{h}_i' \end{pmatrix} \tag{5.7-43}$$

where $y = b$ or b'.

For all these cases, we now need to find the elements of the transformation matrices shown in Eq. (5.7-43). We do this by defining local and global coordinate systems as described before using the propagation vectors derived previously for the interaction mechanisms. We shall describe each case separately below.

For the case where the wave first interacts with the ground surface, Eq. (5.7-34) describes the direction in which the specularly reflected energy will travel after interacting with the surface. The elements of the transformation matrices for this case are therefore (see Appendix B for the methodology of how to derive these expressions)

$$\mathbf{h}_{igs2} \cdot \mathbf{h}_{igs2}' = \frac{\mathbf{c} \cdot \mathbf{z} + (\mathbf{k}_i \cdot \mathbf{z})\left[\mathbf{k}_i \cdot \mathbf{c} - 2(\mathbf{k}_i \cdot \mathbf{z})(\mathbf{c} \cdot \mathbf{z})\right]}{\sqrt{1-(\mathbf{k}_i \cdot \mathbf{z})^2}\sqrt{1-(\mathbf{k}_i \cdot \mathbf{c} - 2(\mathbf{k}_i \cdot \mathbf{z})(\mathbf{c} \cdot \mathbf{z}))^2}} \quad , \tag{5.7-44}$$

$$\mathbf{v}_{igs2} \cdot \mathbf{h}_{igs2}' = \frac{\mathbf{k}_i \cdot (\mathbf{c} \times \mathbf{z})}{\sqrt{1-(\mathbf{k}_i \cdot \mathbf{z})^2}\sqrt{1-(\mathbf{k}_i \cdot \mathbf{c} - 2(\mathbf{k}_i \cdot \mathbf{z})(\mathbf{c} \cdot \mathbf{z}))^2}} \quad , \tag{5.7-45}$$

$$\mathbf{h}_{sgs2}\cdot\mathbf{h}'_{sgs2}=\frac{\mathbf{c}\cdot\mathbf{z}-(\mathbf{k}_i\cdot\mathbf{z})(\mathbf{k}_i\cdot\mathbf{c})}{\sqrt{1-(\mathbf{k}_i\cdot\mathbf{z})^2}\sqrt{1-(\mathbf{k}_i\cdot\mathbf{c})^2}}\quad , \tag{5.7-46}$$

and

$$\mathbf{v}_{sgs2}\cdot\mathbf{h}'_{sgs2}=\frac{\mathbf{k}_i\cdot(\mathbf{c}\times\mathbf{z})}{\sqrt{1-(\mathbf{k}_i\cdot\mathbf{z})^2}\sqrt{1-(\mathbf{k}_i\cdot\mathbf{c})^2}}\ . \tag{5.7-47}$$

where **c** is defined in Eq. (B.1).

For the case where the wave first scattered off the cylinder before reflecting in the specular direction from the ground, the propagation vectors are given by Eq. (5.7-37). The elements of the transformation matrices in this case are

$$\mathbf{h}_{igs3}\cdot\mathbf{h}'_{igs3}=\mathbf{h}_{sgs2}\cdot\mathbf{h}'_{sgs2}\,, \tag{5.7-48}$$

$$\mathbf{v}_{igs3}\cdot\mathbf{h}'_{igs3}=\mathbf{v}_{sgs2}\cdot\mathbf{h}'_{sgs2}\,, \tag{5.7-49}$$

$$\mathbf{h}_{sgs3}\cdot\mathbf{h}'_{sgs3}=\mathbf{h}_{igs2}\cdot\mathbf{h}'_{igs2}\,, \tag{5.7-50}$$

and

$$\mathbf{v}_{sgs3}\cdot\mathbf{h}'_{sgs3}=\mathbf{v}_{igs2}\cdot\mathbf{h}'_{igs2}\,. \tag{5.7-51}$$

The two signals propagating along the inverse paths add coherently. The total scattering matrix for this case is therefore

$$\mathbf{S}=\mathbf{S}_{gc2}+\mathbf{S}_{cg3}\,. \tag{5.7-52}$$

Performing the matrix multiplications shown in Eqs. 5.7-41 and 5.7-42, we find the elements of the scattering matrix to be

$$\begin{aligned}
S_{hh}&=-R'_h e^{-2\tau_h(b)}\left(S^b_{hhc}+S^{b'}_{hhc}\right)\\
S_{hv}&=e^{-(\tau_h(b)+\tau_v(b))}\left\{R'_v e^{-(\tau_v(z)-\tau_h(z))}S^b_{hvc}-R'_h e^{+(\tau_v(z)-\tau_h(z))}S^{b'}_{hvc}\right\}\\
S_{vh}&=e^{-(\tau_h(b)+\tau_v(b))}\left\{R'_v e^{-(\tau_v(z)-\tau_h(z))}S^{b'}_{hvc}-R'_h e^{+(\tau_v(z)-\tau_h(z))}S^{b}_{hvc}\right\}\\
S_{vv}&=R'_v e^{-2\tau_v(b)}\left(S^b_{vvc}+S^{b'}_{vvc}\right)
\end{aligned}\ . \tag{5.7-53}$$

Here we used the short-hand notation

$$\begin{aligned} R_h' &= R_h\left(\varepsilon_g, \theta_i\right) e^{-2k^2h^2/\cos^2\theta_i} \\ R_v' &= R_v\left(\varepsilon_g, \theta_i\right) e^{-2k^2h^2/\cos^2\theta_i} \end{aligned} . \tag{5.7-54}$$

Reciprocity dictates that the primed and unprimed scattering matrices are the same. Therefore,

$$\begin{aligned} S_{hh} &= -2R_h' e^{-2\tau_h(b)} S_{hhc}^b \\ S_{hv} &= e^{-\left(\tau_h(b)+\tau_v(b)\right)} \left\{ R_v' e^{-\left(\tau_v(z)-\tau_h(z)\right)} - R_h' e^{+\left(\tau_v(z)-\tau_h(z)\right)} \right\} S_{hvc}^b \\ S_{vh} &= S_{hv} \\ S_{vv} &= 2R_v' e^{-2\tau_v(b)} S_{vvc}^b \end{aligned} . \tag{5.7-55}$$

Note that for both S_{hh} and S_{vv} the terms describing the attenuation is simply twice the attenuation through the entire vegetation layer, and does not depend on where inside the layer the scatterer resides. For the cross-polarized term, the attenuation terms does depend on where inside the layer the scatterer is. This is a consequence of the fact that for the cross-polarized terms, the incident and scattered waves have orthogonal polarizations. For part of the path, therefore, the one polarization suffers attenuation, while for the rest of the path, the other polarization is attenuated. The terms that are dependent on z therefore is a function of the difference in attenuation between the two polarizations as shown in Eq. (5.7-55). We now have to form the covariance matrix corresponding to this scattering matrix. This is

$$\left[\boldsymbol{\Sigma}_{db}\left(\theta_i, \phi_i, \theta_s = \theta_i, \phi_s = \phi_i, \theta_c, \phi_c, z\right)\right] = \begin{pmatrix} S_{hh}S_{hh}^* & \sqrt{2}S_{hh}S_{hv}^* & S_{hh}S_{vv}^* \\ \sqrt{2}S_{hv}S_{hh}^* & 2S_{hv}S_{hv}^* & \sqrt{2}S_{hv}S_{vv}^* \\ S_{vv}S_{hh}^* & \sqrt{2}S_{vv}S_{hv}^* & S_{vv}S_{vv}^* \end{pmatrix} \tag{5.7-56}$$

The subscript *db* refers to the double reflection suffered by the signals. Next, we average this matrix over all scatterer orientations, which gives

$$\left\langle\left[\boldsymbol{\Sigma}_{db}\left(\theta_i, \phi_i, z\right)\right]\right\rangle = \int_0^{2\pi}\int_0^{\pi} \left[\boldsymbol{\Sigma}_{db}\left(\theta_i, \phi_i, \theta_s = \theta_i, \phi_s = \phi_i, \theta_c, \phi_c, z\right)\right] p\left(\theta_c, \phi_c\right) \sin\theta_c \, d\theta_c \, d\phi_c \tag{5.7-57}$$

Finally, we have to add the contributions from all the layers within the vegetation volume:

$$\left\langle \left[\boldsymbol{\Sigma}_{db}\left(\theta_i,\phi_i\right)\right]\right\rangle = \int_0^b \left\langle \left[\boldsymbol{\Sigma}_{db}\left(\theta_i,\phi_i,z\right)\right]\right\rangle \rho_s\left(z\right)dz \tag{5.7-58}$$

The radar cross section for this term is then

$$\left[\boldsymbol{\sigma}_{db}\right] = 4\pi \left\langle \left[\boldsymbol{\Sigma}_{db}\left(\theta_i,\phi_i\right)\right]\right\rangle \tag{5.7-59}$$

From Eq. (5.7-55) – (5.7-58), we find that if the density of scatterers is constant throughout the vegetation layer, the results are:

$$\begin{aligned}
\left\langle S_{hh}S_{hh}^*\right\rangle_{db} &= 4\rho b\left\langle S_{hhc}S_{hhc}^*\right\rangle \left|R_h'\right|^2 e^{-4\tau_{hm}/\cos\theta_i} \\
\left\langle S_{vv}S_{vv}^*\right\rangle_{db} &= 4\rho b\left\langle S_{vvc}S_{vvc}^*\right\rangle \left|R_v'\right|^2 e^{-4\tau_{vm}/\cos\theta_i} \\
\left\langle S_{hh}S_{vv}^*\right\rangle_{db} &= -4\rho b\left\langle S_{hhc}S_{vvc}^*\right\rangle R_h'R_v'^* e^{-2\left(\tau_{hm}+\tau_{vm}\right)/\cos\theta_i} \\
\sqrt{2}\left\langle S_{hh}S_{hv}^*\right\rangle_{db} &= 2\sqrt{2}\rho b\left\langle S_{hhc}S_{hvc}^*\right\rangle e^{-\left(3\tau_{hm}+\tau_{vm}\right)/\cos\theta_i} \\
&\quad \frac{\cos\theta_i}{\tau_{vm}-\tau_{hm}}\left\{-R_h'R_v'^*\left[1-e^{-\left(\tau_{vm}-\tau_{hm}\right)/\cos\theta_i}\right]-R_h'R_h'^*\left[1-e^{+\left(\tau_{vm}-\tau_{hm}\right)/\cos\theta_i}\right]\right\} \\
2\left\langle S_{hv}S_{hv}^*\right\rangle_{db} &= 2\rho b\left\langle S_{hvc}S_{hvc}^*\right\rangle e^{-2\left(\tau_{hm}+\tau_{vm}\right)/\cos\theta_i}\left(-R_h'R_v'^*-R_v'R_h'^*\right. \\
&\quad \left.+\frac{\cos\theta_i}{2\left(\tau_{vm}-\tau_{hm}\right)}\left\{R_v'R_v'^*\left[1-e^{-2\left(\tau_{vm}-\tau_{hm}\right)/\cos\theta_i}\right]-R_h'R_h'^*\left[1-e^{+2\left(\tau_{vm}-\tau_{hm}\right)/\cos\theta_i}\right]\right\}\right) \\
\sqrt{2}\left\langle S_{hv}S_{vv}^*\right\rangle_{db} &= 2\sqrt{2}\rho b\left\langle S_{hvc}S_{vvc}^*\right\rangle e^{-\left(\tau_{hm}+3\tau_{vm}\right)/\cos\theta_i} \\
&\quad \frac{\cos\theta_i}{\tau_{vm}-\tau_{hm}}\left\{R_v'R_v'^*\left[1-e^{-\left(\tau_{vm}-\tau_{hm}\right)/\cos\theta_i}\right]+R_h'R_v'^*\left[1-e^{+\left(\tau_{vm}-\tau_{hm}\right)/\cos\theta_i}\right]\right\}
\end{aligned} \tag{5.7-60}$$

Note that when the attenuation coefficients for the two polarizations are small, the expressions become

$$\left\langle S_{hh}S_{hh}^{*}\right\rangle_{db} \approx 4\rho b\left\langle S_{hhc}S_{hhc}^{*}\right\rangle\left|R_h'\right|^2\left[1-\frac{4\tau_{hm}}{\cos\theta_i}\right]$$

$$\left\langle S_{vv}S_{vv}^{*}\right\rangle_{db} = 4\rho b\left\langle S_{vvc}S_{vvc}^{*}\right\rangle\left|R_v'\right|^2\left[1-\frac{4\tau_{vm}}{\cos\theta_i}\right]$$

$$\left\langle S_{hh}S_{vv}^{*}\right\rangle_{db} = -4\rho b\left\langle S_{hhc}S_{vvc}^{*}\right\rangle R_h'R_v'^{*}\left[1-\frac{2\left(\tau_{hm}+\tau_{vm}\right)}{\cos\theta_i}\right]$$

$$\sqrt{2}\left\langle S_{hh}S_{hv}^{*}\right\rangle_{db} \approx 2\sqrt{2}\rho b\left\langle S_{hhc}S_{hvc}^{*}\right\rangle\left\{R_h'R_h'^{*}-R_h'R_v'^{*}\right\}\left[1-\frac{\left(3\tau_{hm}+\tau_{vm}\right)}{\cos\theta_i}\right]$$

$$2\left\langle S_{hv}S_{hv}^{*}\right\rangle_{db} \approx 2\rho b\left\langle S_{hvc}S_{hvc}^{*}\right\rangle\left|R_v'-R_h'\right|^2\left[1-\frac{2\left(\tau_{hm}+\tau_{vm}\right)}{\cos\theta_i}\right]$$

$$\sqrt{2}\left\langle S_{hv}S_{vv}^{*}\right\rangle_{db} \approx 2\sqrt{2}\rho b\left\langle S_{hvc}S_{vvc}^{*}\right\rangle\left\{R_v'R_v'^{*}-R_v'R_h'^{*}\right\}\left[1-\frac{\left(3\tau_{hm}+\tau_{vm}\right)}{\cos\theta_i}\right] \tag{5.7-61}$$

5.8 Simulation Results

In this section we present some results of a single layer vegetation model. To keep things simple, we will assume that the vegetation is grass-like, so that we can represent the vegetation elements with thin dielectric cylinders. We shall first discuss some general results, and then concentrate on the effects of soil moisture on the overall observed radar cross-section.

Putting the results of the previous Section together, we write the total covariance matrix of the vegetated layer as:

$$\left[\boldsymbol{\sigma}_{tot}\right] = \left[\boldsymbol{\sigma}_{veg}\right] + \left[\boldsymbol{\sigma}_{db}\right] + \left[\boldsymbol{\sigma}_{g}\right] \tag{5.8-1}$$

To illustrate the model, we assume the parameters for the vegetation layer and soil surface as shown in Table 5-1. We shall now discuss various different simulations to illustrate the effect of different vegetation parameters on the total scattering.

Table 5-1. Parameters used in simulating the backscatter from a vegetation layer.

Parameter	Value
Cylinder radius	2 mm
Cylinder length	50 cm
Cylinder density	900 cylinders/cubic meter
Vegetation layer height	50 cm
Orientation pdf	Cosine squared around vertical
Surface rms height	1 cm
Surface correlation length	15.2 cm
Radar wavelength	24 cm

5.8.1 Effect of the Angle of Incidence

Figure 5-26 shows the HH scattering cross-sections for the three scattering mechanisms, plus the total scattering cross-section, which is the sum of the three individual scattering mechanisms, as a function of the angle of incidence. We notice that for angles of incidence less than 30 deg, the HH scattering is dominated by direct backscattering from the ground. For angles between 30 and about 55, double reflections dominate the HH return, while for angles larger than about 55 deg, the scattering is dominated by the vegetation layer.

Fig. 5-27 shows the same plots, this time for the HV terms. Direct scattering from the ground is absent because we chose to model the surface scattering with a first-order small perturbation model, which predicts no cross-polarized return. In the cross-polarized return, we note that double reflections dominate for angles <30 deg, while vegetation scattering dominates for larger angles.

The situation is quite different for the VV case shown in Fig. 5-28. For angles less than 35 deg, the scattering is dominated by the underlying ground surface scattering. For angles larger than 35 deg, the vegetation scattering dominates. In the case of VV, double reflection scattering is typically much less than the other two, and does not really contribute much to the overall scattering.

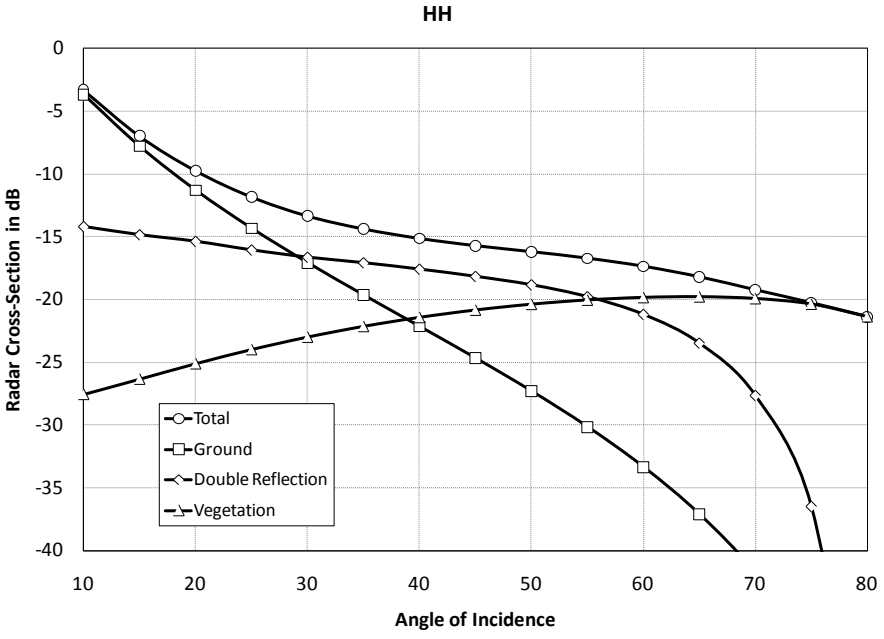

Fig. 5-26. Backscatter cross-sections for the three different scattering mechanisms as a function of angle of incidence at HH polarization.

The specifics of which mechanism dominates is obviously a function of the parameters used to characterize the vegetation and the soil. These results do point out an important point to keep in mind when analyzing scattering from vegetated surfaces, however. The dominant scattering mechanism may be different for the different polarizations. Focusing on an angle of incidence of 40 deg in Fig. 5-26 – Fig. 5-28, we note that the dominant scattering mechanism at HH is double bounce reflections, while at VV and HV the scattering from the vegetation canopy dominates.

5.8.2 Effect of Cylinder Radius

We shall evaluate the effect of the cylinder radius by fixing all other parameters at the values given in Table 5-1, and also fix the angle of incidence at 40 deg. We then vary the cylinder radius in our simulations. The results are shown for the different polarization combinations in Fig. 5-29 for the vegetation layer scattering only. From this calculation it is clear that larger cylinder sizes scatter much more efficiently and as a result the vegetation scattering contribution increases rapidly with increasing cylinder size. For larger cylinders, the increase in scattering is slower, so the rate of increase of the vegetation scattering also decreases.

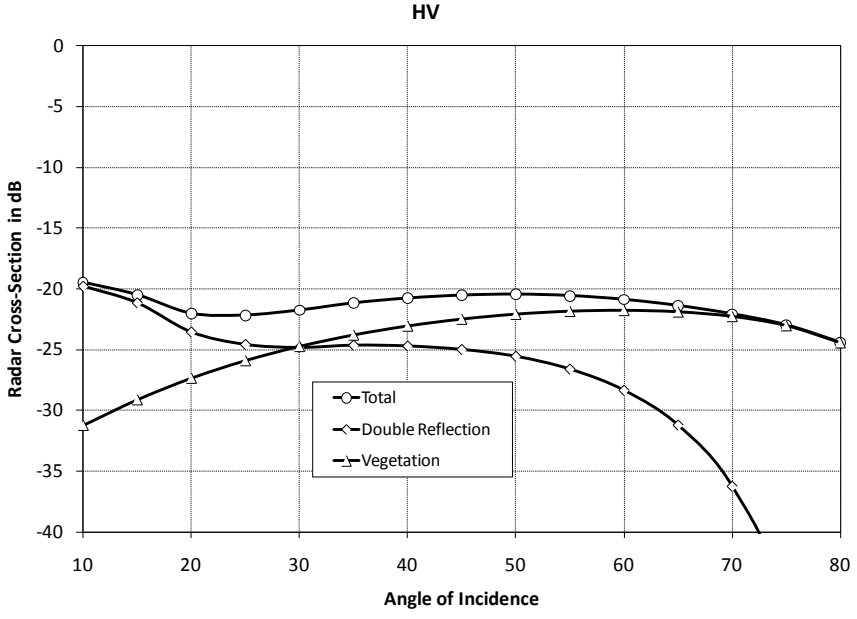

Fig. 5-27. Backscatter cross-sections for the three different scattering mechanisms as a function of angle of incidence at HV polarization.

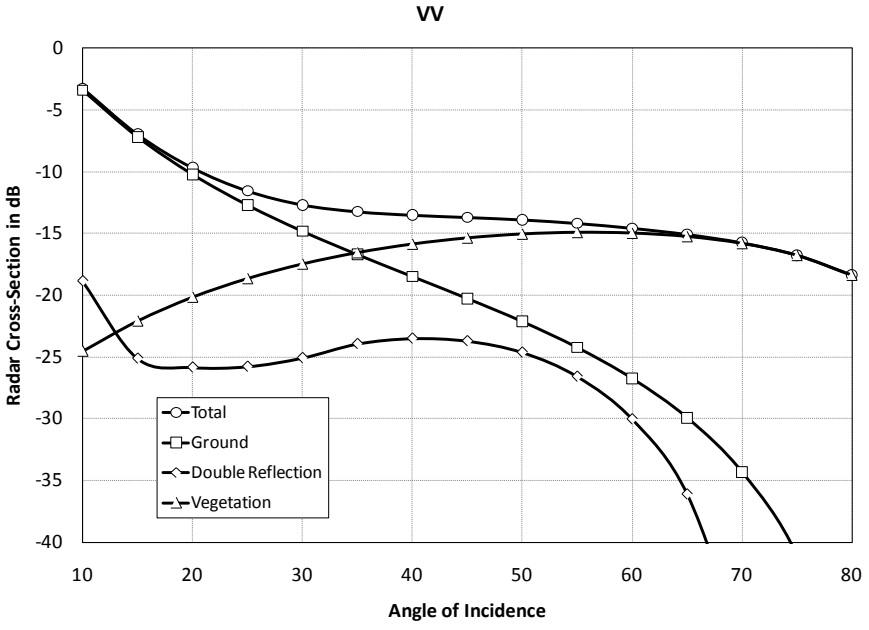

Fig. 5-28. Backscatter cross-sections for the three different scattering mechanisms as a function of angle of incidence at VV polarization.

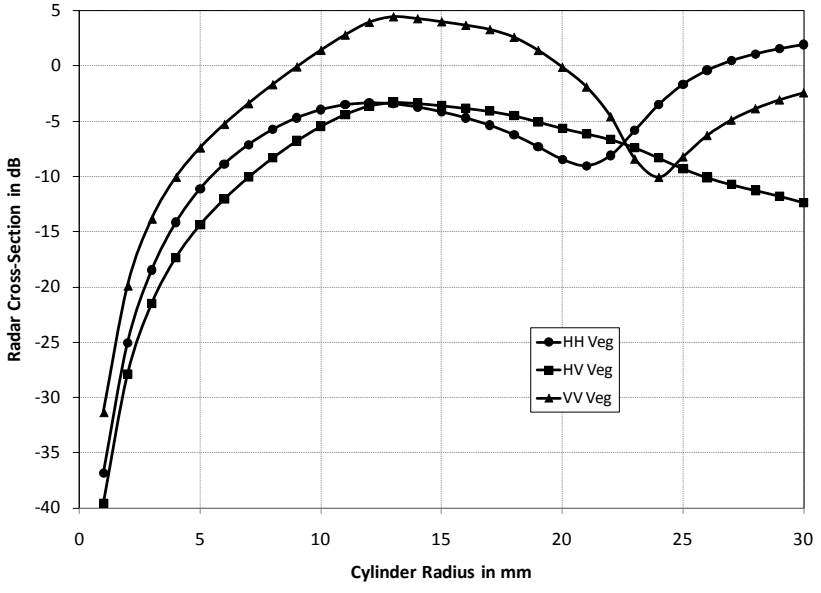

Fig. 5-29. Scattering from the vegetation layer as a function of the cylinder radius. For thin cylinders, there is a dramatic increase in scattering as the cylinder radius increases.

Figure 5-30 shows the scattering at HH polarization for all the scattering mechanisms. For very thin cylinders, the surface scattering dominates. As the cylinders become thicker, the double reflection term starts to dominate as the ground term is attenuated. As the cylinder radius increases further, the double reflection term also decreases, and the vegetation scattering becomes dominant. Not only is the vegetation scattering itself increasing, but the extinction through the vegetation layer is also increasing, as shown in Fig. 5-31.

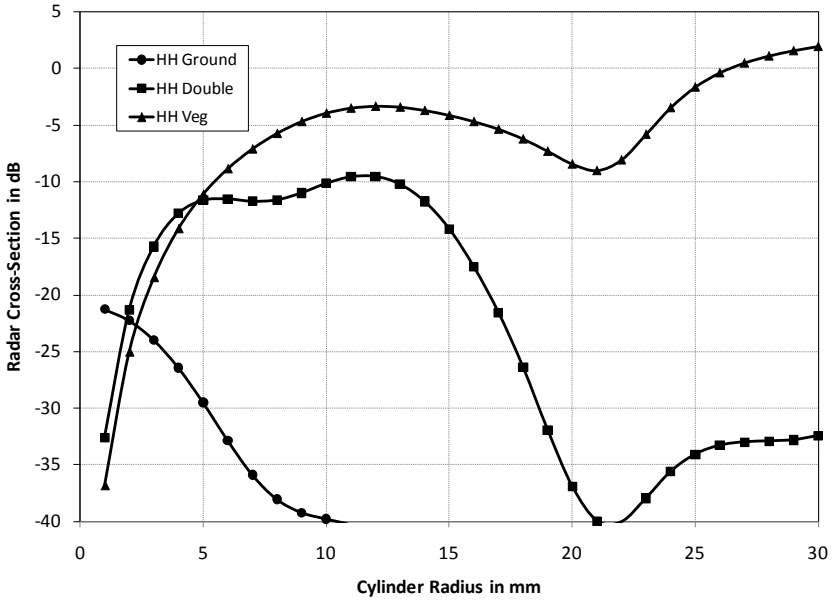

Fig. 5-30. The scattering contributions of the different scattering mechanisms as a function of cylinder radius. Only the HH terms are shown. See the text for discussion.

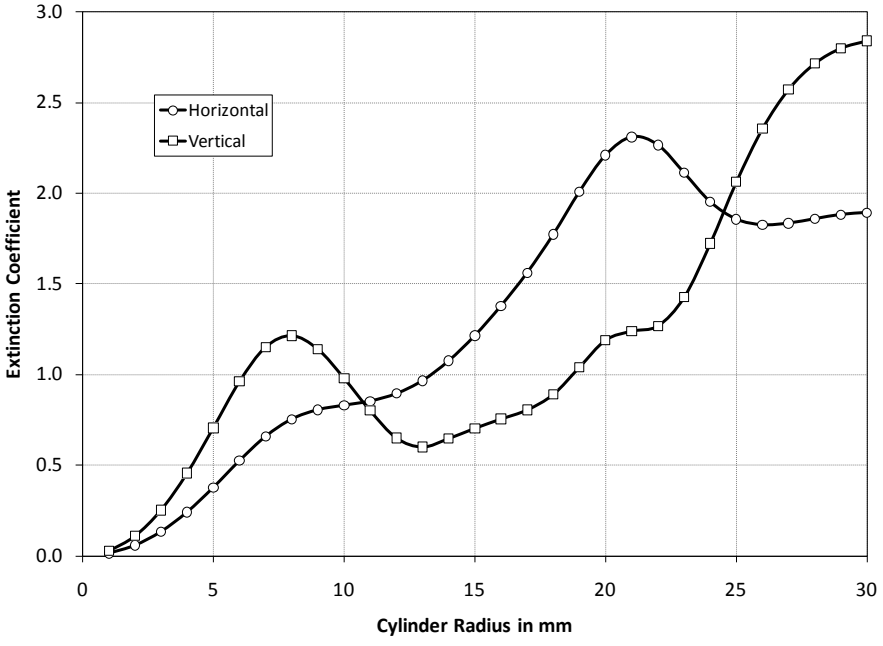

Fig. 5-31. Extinction as a function of cylinder radius. The extinction generally increases as the cylinders get thicker.

5.8.3 Effect of Cylinder Moisture

The cylinder moisture determines the cylinder dielectric constant as described in Section 5.7.1. We now fix all the parameters to their values in Table 5-1 in Section 5.8, and also fix the angle of incidence at 40 deg.

Panel (a) in Fig. 5-32 shows the vegetation scattering as a function of the cylinder water content. As expected, the radar backscatter increases as the cylinder water content (and hence the dielectric constant) increases. The higher dielectric constant means a larger dielectric contrast between the cylinder and the air, resulting in more efficient scattering. The stronger scattering at larger dielectric constant values (or equivalently higher cylinder moisture values) also leads to higher extinction as shown in the panel (b) in Fig. 5-32.

5.8.4 Radar Vegetation Index

We pointed out in Chapter 3 that the radar vegetation index is an indicator of the randomness observed in the scattering, similar to that measured by the entropy. We shall discuss this aspect next. The amount of vegetation is often characterized by the so-called vegetation water content. This quantity is the amount of water, typically expressed in kilograms per square meter, contained

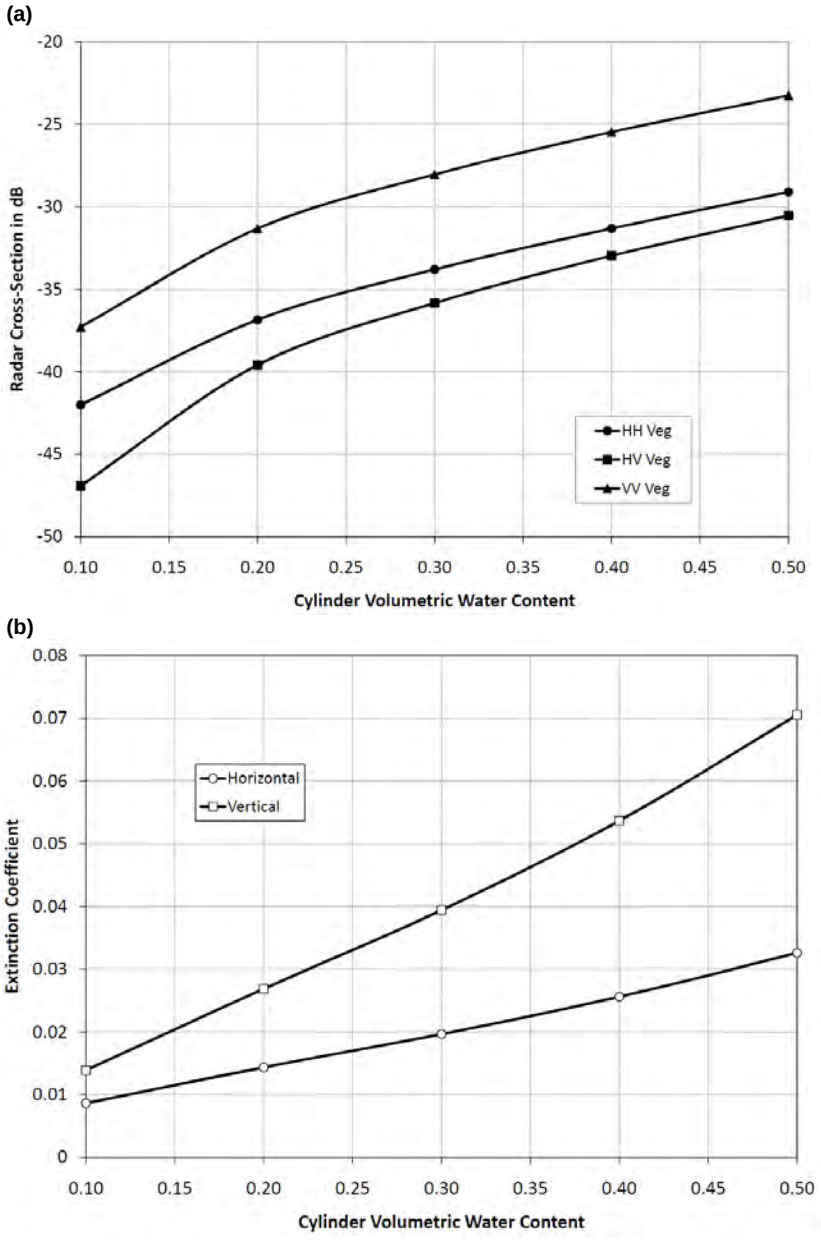

Fig. 5-32. Vegetation scattering (a) and extinction coefficient (b) as a function of the cylinder moisture content. Both quantities increase rapidly with increasing cylinder moisture.

in a column of vegetation with a surface area of 1 square meter. The example we analyzed above would translate to about 1.24 kg/m^2. Unfortunately, the

vegetation water content is a function of many vegetation parameters, namely the radius, length, and density of cylinders, the depth of the vegetation layer, and volumetric moisture of the cylinders.

Figure 5-33 shows the calculated radar vegetation index as a function of the vegetated water content for a number of different cases. The parameters for the different cases are shown in Table 5-2.

First, we notice that for all cases the RVI increases as the vegetation water content increases. This is the result of the fact that at higher vegetation water contents, the scattering from the vegetation layer itself dominates, resulting in a higher RVI. The details differ between the cases however.

Cases 1 and 2 are identical except for the vegetation moisture content. This quantity is used to calculate the dielectric constant of the vegetation as mentioned earlier. In each of these two cases, we keep the vegetation volumetric moisture constant, (and as a consequence the dielectric constant of the vegetation will be constant) and vary the number of cylinders per unit volume to increase the vegetation water content. Here vegetation water content refers to the water content of the layer, not to the moisture in each individual cylinder. These two cases would represent increasing amounts of vegetation

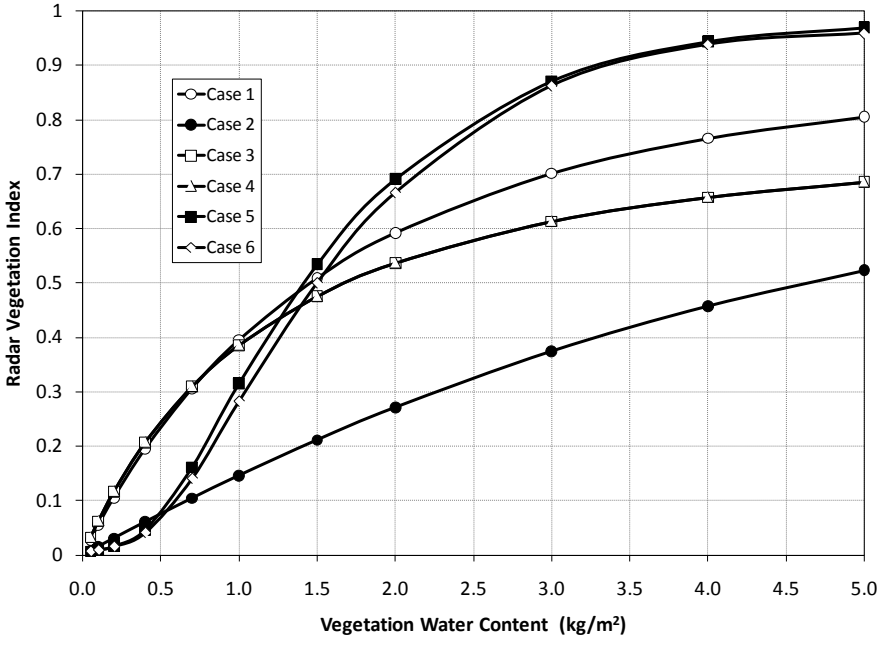

Fig. 5-33. Radar vegetation index as a function of the vegetation water content for various scenarios. See the text for discussion.

Table 5-2. Parameters for several cases of vegetated water content.

Case	Radius	Layer Height	Density	Vegetation Moisture	Soil Moisture
1	1 mm	1 m	Varies	0.5	0.2
2	1 mm	1 m	Varies	0.2	0.2
3	2 mm	1 m	Varies	0.2	0.2
4	2 mm	0.5 m	Varies	0.2	0.2
5	2 mm	1 m	1000	Varies	0.2
6	2 mm	1 m	1000	Varies	0.3

elements such as one would encounter during a growing season, although the constant vegetation water content and layer height would be artificial. In the case of the lower vegetation moisture (Case 2) the RVI increases slower than the higher vegetation water content case. This is a consequence of two factors. First, the higher moisture case means the dielectric constant of the cylinders is higher, leading to stronger scattering by the vegetation, and hence larger RVI values, as discussed earlier. At the same time, the higher dielectric constant also means higher attenuation through the vegetation because of the larger extinction, which decreases the surface related terms, and leads to higher RVI values.

Next, we compare cases 2 and 3. The only difference in this case is that for case 3 the individual cylinders are larger than for case 2. As shown before, larger cylinders scatter more efficiently, and hence the vegetation term is relatively speaking larger than the others, leading to a larger RVI. At the same time, the more efficient scattering means a larger extinction through the vegetation layer, decreasing the contribution from the ground related terms (see Fig. 5-31). This also increases the RVI, so that case 3 generally has larger RVI than case 2.

Case 4 is the same as case 3, except that the vegetation layer is half the height. This means that for the same vegetation water content, case 4 has double the cylinders that case 3 would have. The two RVI curves are identical. The reason for this is clear when the equations from the previous Section are considered. In all cases, we find the product of the density and the layer height. Therefore, if all other parameters are held constant, as long as this product is the same, we would expect the same result.

The cases discussed so far all have constant vegetation water content. For a given vegetation canopy over short time scales, the vegetation elements do not change their size and number, and the layer height can be considered constant. However, due to changing soil moisture and other environmental conditions, it is possible that the cylinder moisture content can change, thereby changing the vegetation water content. This is studied with cases 5 and 6. Both cases are identical except that the soil moisture of case 6 is higher than that of case 5. Here we keep the cylinder physical dimensions and number (density) fixed, and

vary the cylinder moisture content. Compared to case 3, this shows a different behavior. At first, when the vegetation water content is very low, (now vegetation water content is directly proportional to cylinder moisture), the dielectric constant of the cylinders is small, leading to inefficient scattering from the vegetation layer (see Figure 5-32), and a low RVI. As the moisture increases in the vegetation, the scattering from the vegetation quickly becomes dominant, leading to a rapid increase in the RVI. Once the vegetation scattering dominates, there is little additional change in the RVI. Case 6 shows indeed that the underlying soil moisture plays a relatively small part. When the surface is wetter (case 6), the soil term stays dominant a while longer, meaning that the rapid increase of the RVI happens for a slightly higher value of vegetation water content. This is a small effect, however.

5.8.5 Effect of Soil Moisture

The important question is whether we can observe changes in soil moisture by observing the overall scattering from the vegetation. As shown in the previous examples, under certain conditions, either the direct backscatter from the soil surface itself, or the double bounce scattering may dominate even though both these terms are attenuated. In these cases, we would expect to measure a change in the overall backscatter from the vegetation layer as the soil moisture changes.

Figure 5-34 shows the results of a simulation where we have assumed that the vegetation moisture does not change, even though the surface soil moisture changes. All other parameters, such as cylinder length, diameter, etc, as well as surface roughness also remain constant. The values of the parameters used in the simulation are as given in Table 5-1, except we used a cylinder density of 1600 cylinders per cubic meter.

The total scattering terms for both HH and VV show an approximately linear relationship with the soil moisture when plotted in dB. In fact, when fitting a linear function to these graphs, we find

$$\begin{aligned} \sigma_{hh}(dB) &= 9.8 m_{soil} - 21.2; \quad R^2 = 0.95 \\ \sigma_{vv}(dB) &= 13.7 m_{soil} - 18.7; \quad R^2 = 0.96 \end{aligned} \tag{5.8-2}$$

Both these functions fit the simulated data very well. From this one result it appears that the VV polarization shows more sensitivity to the underlying ground surface moisture. A look at the individual scattering mechanisms in Fig. 5-34 shows that the scattering from the ground surface actually dominates in this case. As the previous examples showed, when the vegetation water content increases, the scattering from the vegetation becomes more dominant.

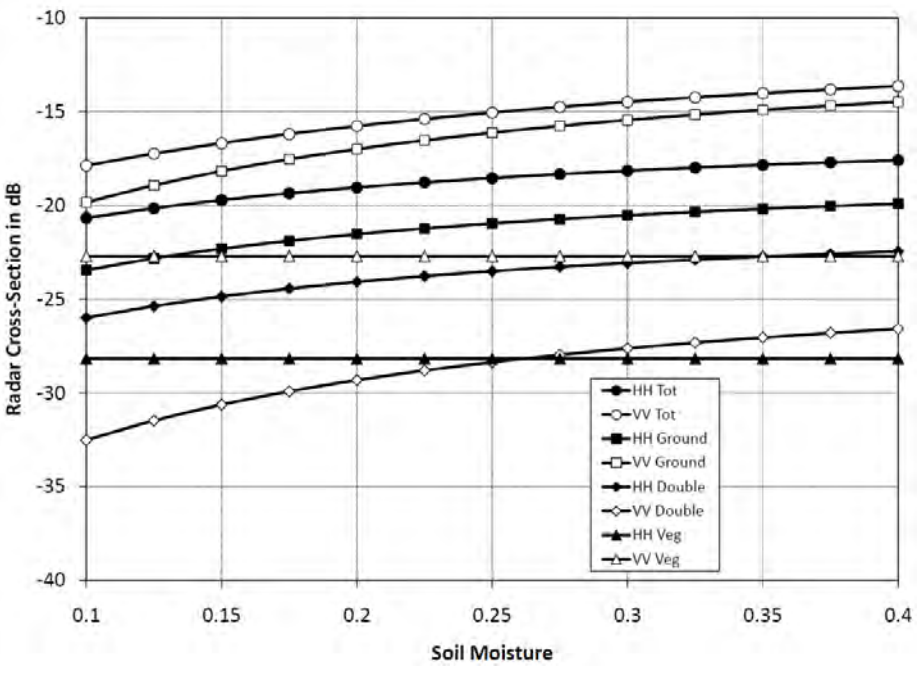

Fig. 5-34. These graphs show the sensitivity of the various scattering terms to changes in the surface soil moisture, assuming that all other parameters are constant. The vegetation water content is 0.8 kg/m^2. The incidence angle is 40 deg.

Figure 5-35 shows the slope of the linear fits to the simulated data for different values of vegetation water content. These values were calculated using different values of the cylinder moisture to vary the vegetation water content. The cylinder size and density were kept fixed.

The data shows, as expected, a decrease in sensitivity to surface soil moisture for increasing vegetation water content. The sensitivity at VV decreases faster, because the VV scattering from the vegetation and particularly the extinction for vertical polarization increases faster with increasing vegetation water content. Both these factors combine to decrease the sensitivity to scattering from the underlying soil surface. HH polarization retains a reasonable sensitivity to surface soil moisture even for the larger vegetation water content values.

Different graphs are shown for different cylinder densities. The cylinder density has a small effect on the overall sensitivity to soil moisture, with smaller densities generally resulting in smaller sensitivities. At first glance this seems counter intuitive as one would expect fewer cylinders to have less extinction, and therefore should show more sensitivity to the underlying soil moisture. The

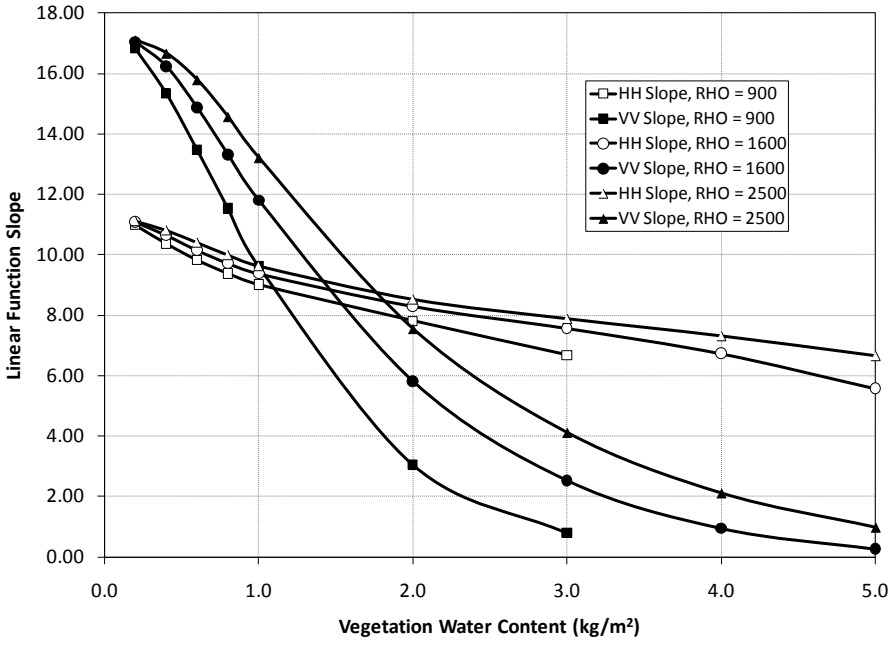

Fig. 5-35. This data shows a decrease in sensitivity to surface soil moisture as the vegetation water content increases. The VV sensitivity decreases faster than the HH sensitivity.

explanation for the graphs lies in the fact that the sensitivity is displayed as a function of the water content of the vegetation layer; not the moisture content of the cylinders. The layer water content is, among other factors, the product of the cylinder moisture and the cylinder density. Therefore, for a particular vegetation layer water content, the lower density layer has a higher cylinder moisture content, and hence a larger dielectric constant. The higher dielectric constant gives a bigger increase in scattering efficiency (and a larger associated extinction) than what is lost because of the lower density, resulting in a lower sensitivity to soil moisture. Note that in the lowest density case the graph stops at a vegetation water content of about 3 kg/m^2. At this value, the cylinders have to be 100% moisture in order for the vegetation layer to have this much water per unit area.

In the simulations above, we assumed that the vegetation moisture stays constant, regardless of what the underlying soil moisture might be. In practice one might expect that as the soil gets wetter, the vegetation moisture might increase, even if there might be a delay between the two values. Unfortunately, there seems to be little quantitative experimental data on this topic. Figure 5-36 shows the case where the vegetation moisture is 100% correlated with the soil

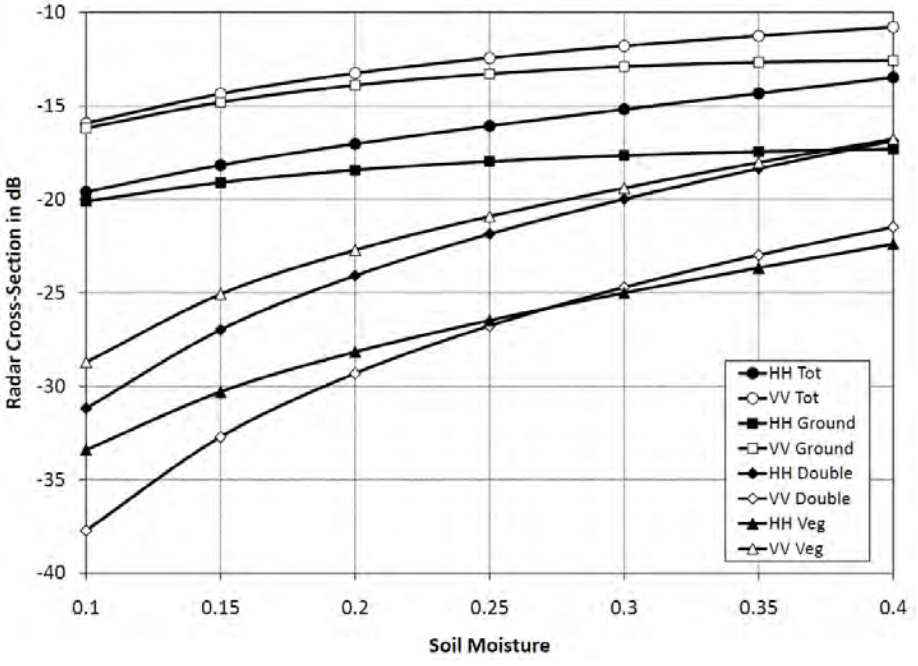

Fig. 5-36. These graphs show the strength of the various scattering components assuming that the soil moisture and the vegetation moisture are the same value. There is significant more sensitivity to moisture if these two quantities are the same.

moisture. This simulation shows that there is a significant increase in sensitivity to soil moisture if the vegetation and soil moistures are correlated. In fact, the two functions for this case are

$$\begin{aligned} \sigma_{hh}(dB) &= 19.9 m_{soil} - 21.2; \quad R^2 = 0.99 \\ \sigma_{vv}(dB) &= 16.5 m_{soil} - 16.9; \quad R^2 = 0.95 \end{aligned} \tag{5.8-3}$$

In fact, the HH sensitivity is nearly twice the maximum value we found before.

This last example is perhaps unrealistic, but can be considered a limiting case. In practice we can expect some correlation between the vegetation moisture and the soil moisture, even if it is not exactly 100% as assumed above. Any correlation will increase the sensitivity to soil moisture over that calculated assuming no correlation.

5.8.6 Inverting for Soil Moisture: The Data Cube

The aim of remote sensing is to be able to infer some of the geophysical properties of the terrain from measurements. With a single frequency

polarimetric radar, we have a limited number of measurements. In the case of terrain with reflection symmetry, we have at most 5 independent measurements, the cross-sections at HH, VV and HV, and the magnitude and phase of the correlation between HH and VV. Our model, on the other hand, has many more input parameters, even for the simple single layer model described here. When this model is extended to multiple layers, the number of input parameters increases dramatically. It is therefore impractical to solve uniquely for all of these input parameters with only a limited number of observables. It is therefore clear that we will have to combine some of the physical characteristics of the vegetation into a single descriptor in order to have any chance of inverting the observations.

In addition to the difficulty of having a limited number of observations, the modeling requires a large number of calculations for each case. This makes inversion of the data computationally quite challenging. One way to get around this problem is to construct "data cubes" for each model. This approach would calculate the polarimetric parameters for a range of input parameters. For example, one choice would be to fix many of the model parameters such as cylinder radius, length, and density, and then calculate the polarimetric parameters as a function of surface roughness, soil moisture, vegetation water content and angle of incidence. These values are then stored in files for later use. Each observation can then be "inverted" by searching these data cubes for the best simultaneous match to all the observables.

Many different ways could be used to define the best match between the observed and simulated data. As an example, for a multi-polarized radar that measures HH, VV and HV cross-sections, one could choose to define the error between the observations and the simulations as

$$\mathrm{E} = \sqrt{\left(\sigma_{hh\,obs} - \sigma_{hh\,sim}\right)^2 + \left(\sigma_{vv\,obs} - \sigma_{vv\,sim}\right)^2 + \left(\sigma_{hv\,obs} - \sigma_{hv\,sim}\right)^2} \ . \quad (5.8\text{-}4)$$

We can calculate this quantity for all values in the data cubes, and choose that set of parameters that minimizes this error to be representative of the vegetated terrain.

The cube inversion method has been studied extensively by Arii (2009) [37] in his thesis, where he compares different combinations of polarimetric parameters and the accuracy with which the vegetation parameters can be inferred. He not only looked at the multi-polarization case described above, but he also looked at including all the polarimetric parameters in the inversion. Since some of the elements of the covariance matrix are complex numbers, he proposes using the natural logarithm of the radar cross-sections in the error

calculations. This will allow the incorporation of the measured polarimetric phases in addition to the magnitudes.

Arii [37] found that for vegetation water content values less than about 0.5 kg/m^2 adding the other polarimetric parameters made little difference in the accuracy of the inversion for soil moisture. However, for vegetation water contents larger than this value, adding the cross-correlation between HH and VV made a substantial difference, improving the accuracy of the inversion substantially.

Arii also points out that the inversion accuracy is very sensitive to the exact values of the cylinder parameters. In his investigation, he simulated the data cubes with a fixed radius of 2 mm, and then generated test data with radii ranging between 2 and 3 mm. He then used the data cubes to invert the data. The resulting errors in soil moisture estimates were largest for larger vegetation moisture contents, with the error exceeding 10% at a vegetation water content of 2.5 kg/m^2 when the radius of the test cylinder was larger than 2.3 mm. Based on these results, Arii concluded that for such an inversion scheme to be successful, one would need use have a family of data cubes generated for different vegetation classes.

5.9 Time Series Estimation of Soil Moisture

So far we have discussed estimations of soil moisture that happens at a particular instant of time. We will call these "snap-shot" algorithms, since they would provide us with an estimate of the moisture as if we took a picture at a specific time. In doing so, we do not rely on any knowledge about the past values of the soil moisture at that specific location. In this Section we shall discuss a different approach in which we will track changes in the soil moisture over time.

To derive such a time series algorithm, we note that the polarimetric backscattering cross-section can be written as

$$\sigma_{pq} = f_{pq}(P_1, P_2, ..., P_N), \tag{5.9-1}$$

where P_i (i = 1, 2, …, N) represents a remote sensing variable such as soil moisture, surface roughness, and parameters characterizing vegetation. The subscripts p and q can be h or v depending upon the polarization configuration. The time variation of the backscattering cross-section is calculated as

$$\frac{\partial \sigma_{pq}}{\partial t} = \sum_{i=1}^{N} \frac{\partial f_{pq}}{\partial P_i} \frac{\partial P_i}{\partial t} . \tag{5.9-2}$$

Notice that $\partial f_{pq} / \partial P_i$ represents the backscattering cross section sensitivity to physical quantities such as soil moisture. This is the term that is used in the "snap-shot" algorithms to estimate soil moisture from polarimetric radar data. However, the time-series formulation shown in Eq. (5.9-2) has an additional term, $\partial P_i / \partial t$, that can be thought of as a temporal filter, which provides a weighting factor for each sensitivity. That is, if the time variation of a parameter such as soil texture and the vegetation structure is not significant enough to change the model function appreciably over a specified time scale, we can ignore the effect of that parameter on the temporal variation of the radar cross-section.

To best define a time-series algorithm, we have to consider the time scale over which the radar cross-section varies. There are three fundamental time scales of importance: 1) diurnal time scale, 2) soil moisture response time after a precipitation event and 3) the time scale over which a model function is invariant; this is the time scale that soil moisture will be retrieved. In order to minimize the diurnal effect on the soil moisture retrieval accuracy, time-series data must be collected at the same solar time (elapsed time after sun rise). In addition, from the time scale of the soil moisture response due to a precipitation event, we can define the sampling requirement of the time-series approach.

For the time-series approach, it is preferred that the radar data are collected using the same imaging geometry for each measurement. Especially the incidence angle should be constant for all time-series measurements unless the incidence angle effect on the backscattering cross-section can be properly compensated for. This can be accomplished with proper mission design. For instance, the Hydros radar configuration discussed by Entekhabi et al. (2004) [38] minimizes the imaging geometry change of a spaceborne radar. Even in this configuration, however, the azimuth angle of these observations can change; the impact of such azimuth angle variations was observed and characterized by Baup et al. (2007) [39] for surfaces in Mali. Except for one area that showed some azimuthal variation, they found little evidence, even in areas covered with sand dunes, for azimuth angle variations creating significant variations in radar cross-section. Nevertheless, it is obvious that a constant illumination geometry would eliminate any variations other than geophysical changes.

For bare surfaces, there are three parameters to be considered: soil moisture (P_1), surface roughness (P_2), and soil texture (P_3). If P_2 and P_3 vary in time much slower than P_1 (soil moisture), Eq. (5.9-2) can be approximated by

$$\frac{\partial \sigma_{pq}}{\partial t} \approx \frac{\partial f_{pq}}{\partial P_1}\frac{\partial P_1}{\partial t} \quad \text{if} \quad \frac{\partial P_2}{\partial t}, \frac{\partial P_3}{\partial t} << \frac{\partial P_1}{\partial t}. \tag{5.9-3}$$

Under this assumption, the temporal variation of a backscattering cross section depends only on the soil moisture variation ($\partial P_1/\partial t$). Therefore,

$$\Delta \sigma_{pq} \approx \frac{\partial f_{pq}}{\partial P_1}\Delta P_1. \tag{5.9-4}$$

It should be pointed out that if the surface roughness is influenced by soil moisture, this formulation can include this effect. For example, if the surface roughness changes when soil becomes dry after a precipitation event $(P_2 = g(P_1))$, then

$$\Delta P_2 = \frac{\partial g}{\partial P_1}\Delta P_1. \tag{5.9-5}$$

In this case the backscattering cross section can be written as

$$\Delta \sigma_{pq} \approx \left[\frac{\partial f_{pq}}{\partial P_1} + \frac{\partial f_{pq}}{\partial P_2}\frac{\partial g}{\partial P_1}\right]\Delta P_1. \tag{5.9-6}$$

The time scale over which this approach can be used to track soil moisture changes depends on the time scale over which the quantity inside the square brackets change. As long as the time is short enough that we can consider this quantity to be constant, we can attribute changes in the observed radar cross-section to changes in soil moisture.

For vegetated surfaces, at least two additional parameters must be added to include the vegetation scattering: vegetation structure (P_4) and vegetation dielectric constant or water content (P_5). If we ignore the vegetation structure (P_4) change and assume that the vegetation dielectric constant is affected by soil moisture ($P_5 = h(P_1)$), the backscattering cross section change can be written as

$$\Delta \sigma_{pq} \approx \left[\frac{\partial f_{pq}}{\partial P_1} + \frac{\partial f_{pq}}{\partial P_5}\frac{\partial h}{\partial P_1}\right]\Delta P_1. \tag{5.9-7}$$

Here, we have also assumed that the roughness change due to the soil moisture variation is much less significant than the dielectric constant change of vegetation. After a precipitation event, the dielectric constant of vegetation can change significantly as observed by McDonald et al. (2002) [40]. Both the vegetation dielectric constant and soil moisture will therefore be influenced by a precipitation event. This effect of the dielectric constant change of vegetation is represented by the second term in Eq. (5.9-7).

The next step is to derive model functions using experimental data: those shown in Eq. (5.9-6) for bare surfaces and in Eq. (5.9-7) for vegetated surfaces. We note that if these model functions are approximately linear, ΔP_1 does not have to be small since higher order terms of ΔP_1 can be ignored.

Model functions for bare surfaces can be derived using theoretical solutions such as SPM and IEM as shown in the previous Section. Kim and van Zyl (2009) [11] linked the radar cross-section expressed in dB to soil moisture directly. A similar time-series approach was successfully applied to European Remote Sensing Satellite (ERS) data by Wagner and Scipal [41]. For vegetated surfaces, Kim and van Zyl (2009) [11] used L-band radar data collected using a truck-mounted radar system from May to October 2002 at USDA-ARS (U.S. Dept. of Agriculture-Agricultural Research Service) OPE3 (Optimizing Production Inputs for Economic and Environmental Enhancement) test site in Beltsville, MD [42]. The results are shown in Fig. 5-37.

From the experimental data Kim and van Zyl (2009) [11] found that both H- and V-polarization backscattering cross sections at L-band can be modeled better using a linear relationship between the radar cross-section expressed in dB and volumetric soil moisture (m_v) as

$$10\log_{10}(\sigma_{pp}) = Cm_v + D \tag{5.9-8}$$

A similar result was reported previously at C-band by Ulaby et al. (1986) [17]. Therefore, using this linear relationship, one can write the time series algorithm for the soil moisture as

$$m_v = A\left(10\log_{10}\sigma_{pp}\right) + B \tag{5.9-9}$$

Since the two unknowns, A and B, may vary from one pixel to the next, one must develop a method to reliably estimate A and B for each pixel. Kim and van Zyl (2009) [11] point out that in order to determine the two unknowns (A and B) in Eq. (5.9-9), it is necessary to estimate at least two soil moisture values corresponding to two backscattering cross sections. As an example, if

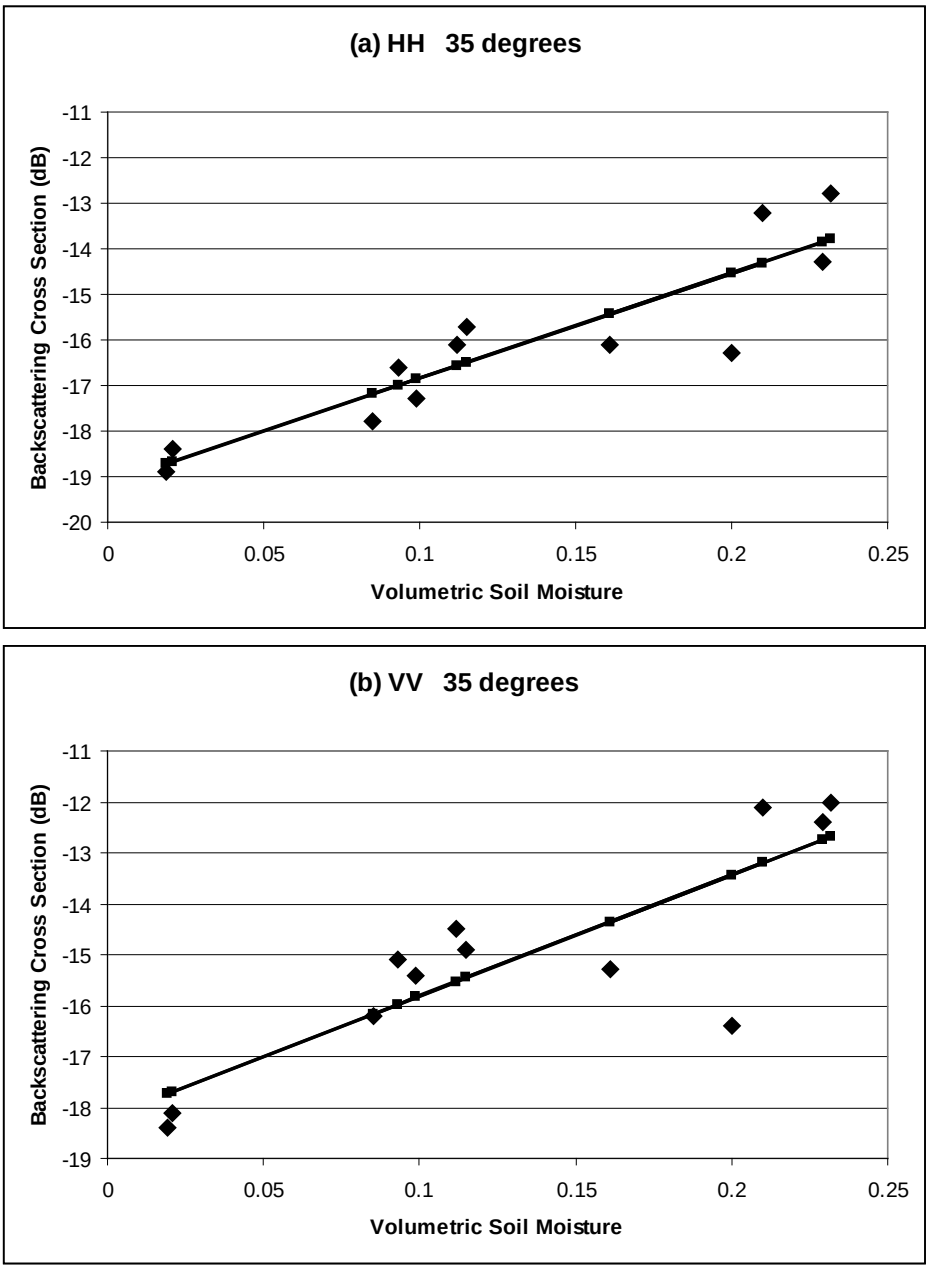

Fig. 5-37. Linear fit of L-band HH and VV backscattering cross sections (dB) for various soil moisture (unitless) collected during the USDA-ARS OPE3 (2002) [42] field experiment for a corn field (biomass > 2.5 kg/m2). In order to remove the diurnal effect, the radar data collected near 8:00 AM were used in this figure. The incidence angle is 35 deg.

the extreme soil moisture values (as an example, 35% for the maximum value and 5% for the minimum value) of time-series data are known, A and B can be estimated using the corresponding maximum and minimum backscattering cross sections. This might not be very practical since these extreme values may not be known for each pixel. On the other hand, if the time period includes completely dry and completely wet (i.e., run-off) conditions, the estimation of A and B are relatively straightforward.

Using experimental data, Kim and van Zyl (2009) [11] showed that for bare surfaces, it is possible to estimate volumetric soil moisture better than 2% if the extreme soil moisture values are known exactly. The accuracy slightly degrades for vegetated surfaces. If incorrect extreme values are used, the retrieval accuracy becomes worse. In order to evaluate the effect of the error in extreme soil moisture values statistically, Kim and van Zyl (2009) [11] performed a simple simulation by adding a random error to the exact soil moisture value of two extreme conditions (wet and dry). The random error is simulated using a uniform random variable. The simulation results are shown in Fig. 5-38. The abscissa value (x) in Fig. 5-38 represents the uniform random error over [–x, +x]. The retrieval error is calculated by averaging the magnitude of estimation errors when these random errors are introduced to the inversion process. For both bare and vegetated surfaces, the extreme soil moisture values (wet and dry) must be known better than 6% in order to reduce the retrieval error to be less than 4%.

Our previous simulations showed that as the vegetation water content increase, the slope of the linear function relating radar cross-section to soil moisture changes (see Figure 5-35). Therefore, over the full growing season, one may have to segment the radar data in order to apply the correct model function for a vegetated surface. The Radar Vegetation Index (RVI) has been proposed to identify vegetated surfaces [11]. The RVI values for the time-series data from the USDA-ARS OPE3 are shown in Fig. 5-39. When RVI > 0.35, the biomass level of the corn field was higher than 2.5 kg/m^2 except one data point. The peak biomass was about 7 kg/m^2. From this analysis, a vegetation model function must be used when RVI > 0.35. When we consider the attenuation due to vegetation (biomass as high as 7 kg/m^2), it is not obvious that the radar sensitivity to the soil moisture variation is due to the direct scattering from a soil surface. It is possible that the dielectric constant change of vegetation enhances the sensitivity.

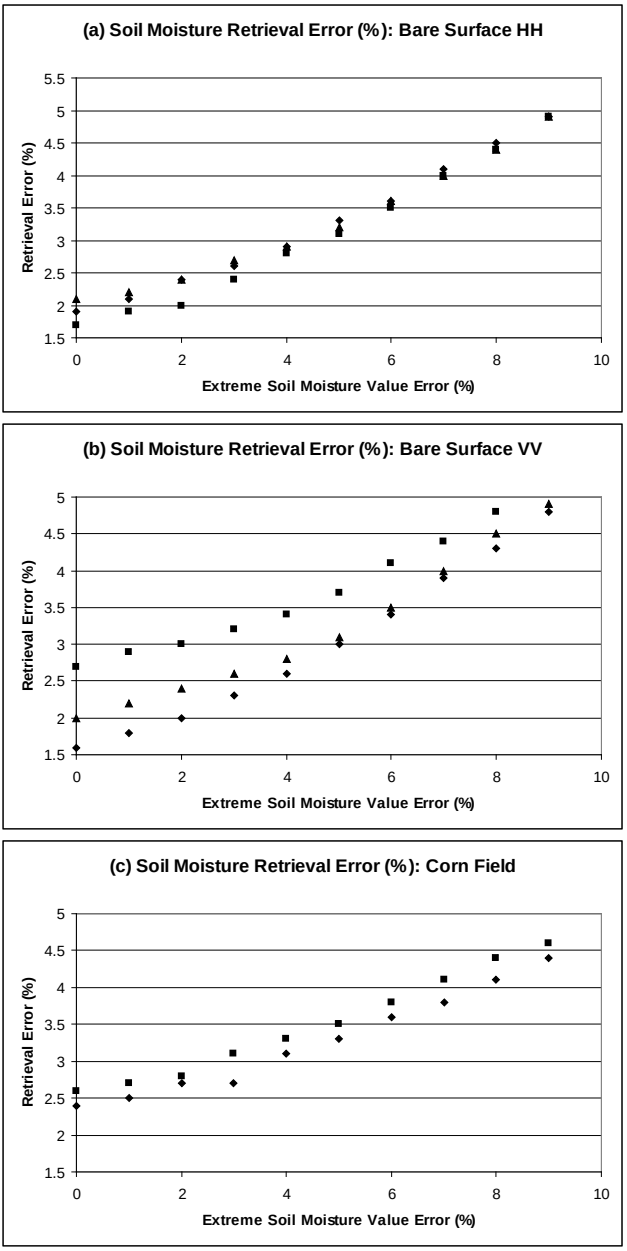

Fig. 5-38. Average retrieval errors of volumetric soil moisture (%): (a) HH for a bare surface (diamond: 30 deg, square: 40 deg. and triangle: 50 deg.), (b) VV for a bare surface (diamond: 30 deg, square: 40 deg. and triangle: 50 deg.) and (c) HH and VV for a corn field (diamond: HH and square: VV) (Kim and van Zyl, 2009) [11].

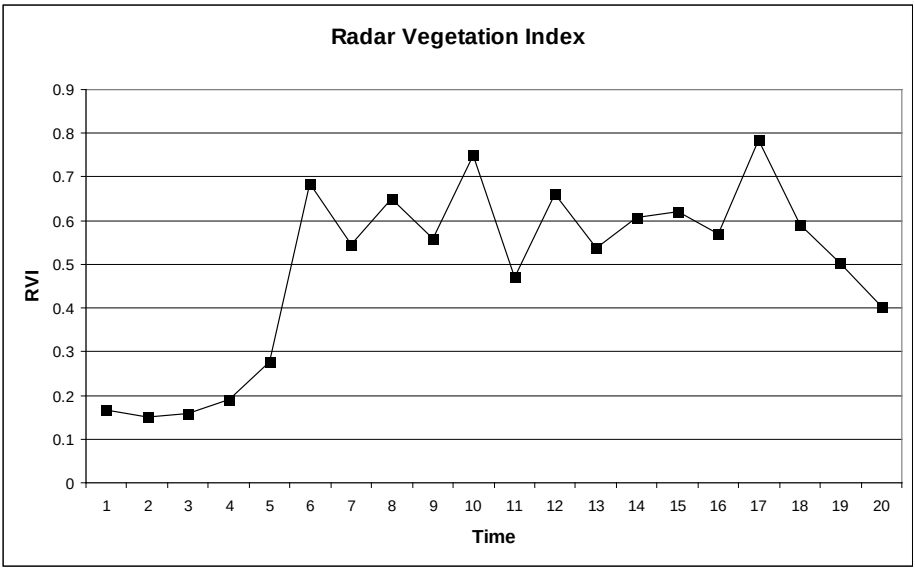

Fig. 5-39. RVI (Radar Vegetation Index) estimated from polarimetric radar data collected during the USDA-ARS OPE3 (2002) field experiment. The abscissa represents time in weeks. When RVI is compared with biomass measurements, the condition that RVI > 0.35 defines all data with biomass > 2.5kg/m2 except one point (6th week).

5.10 Summary

In this Chapter, we examined methods for using radar data to estimate surface soil moisture and roughness. Many different models exist to calculate the radar cross-section as a function of surface roughness and surface dielectric constant. Herein, we looked only at a small subset of these models and showed that they all predict sensitivity to soil moisture.

We also looked at a few of the more commonly used inversion algorithms and compared the results. Most of these models perform reasonably well for bare surfaces. For vegetated surfaces, however, the models become very complicated and the soil moisture inversion becomes less accurate.

Most of the models we discussed here fall into the class of “snapshot” algorithms; that is, they try to estimate the soil moisture using data only from one instant in time, effectively ignoring all prior information that might exist. We also discussed a different approach that holds the promise of being applicable to many different types of surface covers. This time series approach fits a linear function through the radar cross section as a function of soil moisture using the extreme values of the radar cross-sections as indicators of saturated wet and completely dry conditions. As long as these extreme values are accurate to within 6 percent, soil moisture can be estimated to an accuracy

of better than 4 percent. The obvious disadvantage of the time series approach is that inversions can only be performed once the extreme values have been observed.

The science of inverting radar data for soil moisture will receive a significant increase in attention in the near future. As of the writing of this book, the Japanese Advanced Land Observing Satellite Phased Array type L-band Synthetic Aperture Radar (ALOS PALSAR) system is acquiring polarimetric SAR data that could be used to check many of these algorithms. The National Aeronautics and Space Administration (NASA) is also planning the Soil Moisture Active Passive (SMAP) mission for launch in 2015. This system will carry both a radar and a radiometer to routinely cover the globe specifically for the purpose of estimating surface soil moisture. Undoubtedly, this area of research will expand rapidly to meet this challenge, and the climate research community can look forward to excellent results from these missions.

References

[1] J. Wang, E. Engman, J. Shiue, M. Ruzek and C. Steinmeier, "The SIR-B Observations of Microwave Backscatter Dependence on Soil Moisture, Surface Roughness, and Vegetation Covers," *IEEE Transactions on Geoscience and Remote Sensing*, vol. 24, pp. 510–516, 1986.

[2] M. C. Dobson and F.T. Ulaby, "Preliminary Evaluation of the SIR-B Response to Soil Moisture, Surface Roughness, and Crop Canopy Cover," *IEEE Transactions on Geoscience and Remote Sensing*, vol. 24, pp. 517-526, 1986.

[3] T. J. Jackson and F. R. Shiebe, *Washita '92 Data Report*, NAWQL Report 101, USDA National Agricultural Water Quality Lab, Durant, Oklahoma, 1993.

[4] K. Schneider and N. Oppelt, "The Determination of Mesoscale Soil Moisture Patterns with ERS Data," *1998 IEEE International Geoscience and Remote Sensing Symposium Proceedings (IGARSS1998)*, Vol. 4, pp. 1831–1833, 1998.

[5] A. S. Quesney, S. Le Hegarat-Mascle, O. Taconet, D. Vidal-Madjar, J. P. Wigneron, C. Loumagne, and M. Normand. "Estimation of Watershed Soil Moisture Index from ERS/SAR Data," *Remote Sensing of the Environment*, vol. 72, pp. 290–303, 2000.

[6] P. C. Dubois, J. J. van Zyl, and E. T. Engman, "Measuring Soil Moisture with Imaging Radars," *IEEE Transactions on Geoscience and Remote Sensing*, vol. 33, issue 4, pp. 915–926; plus corrections to, vol. 33, issue 7, p. 1340, 1995.

[7] J. Shi, J. Wang, A. Hsu, P. O'Neill, and E. T. Engman, "Estimation of Bare Surface Soil Moisture and Surface Roughness Parameters Using L-Band SAR Image Data," *IEEE Transactions on Geoscience and Remote Sensing*, vol. 35, pp. 1254-1266, 1997.

[8] Y. Oh, K. Sarabandi, and F. T. Ulaby, "An Empirical Model and Inversion Technique for Radar Scattering from Bare Soil Surface," *IEEE Transactions on Geoscience and Remote Sensing*, vol. 30, pp. 370–381, 1992.

[9] U. Wegmuller, *Active and Passive Microwave Signature Catalogue on Bare Soil (2-12 GHz)*, Institute of Applied Physics, University of Berne, Switzerland, 1993.

[10] A. K. Fung, Z. Li, and K. S. Chen, "Backscattering from a Randomly Rough Dielectric Surface," *IEEE Transactions on Geoscience and Remote Sensing*, vol. 30, pp. 356–369, 1992.

[11] Y. Kim and J. J. van Zyl, "A Time-Series Approach to Estimate Soil Moisture Using Polarimetric Radar Data: Bare Surfaces," *IEEE Transactions on Geoscience and Remote Sensing*, vol. 47, pp. 2519–2527, August 2009.

[12] T.G. Farr, "Microtopographic Evolution of Lava Flows at Cima Volcanic Field, Mojave Desert, California" *Journal of Geophysical Research*, vol. 97, pp. 15,171–15,179, 1992.

[13] J. R. Wang and T. J. Schmugge, "An Empirical Model for the Complex Dielectric Permittivity of Soils as a Function of Water Content," *IEEE Transactions on Geoscience and Remote Sensing*, vol. 18, pp. 288–295, 1980.

[14] M. T. Hallikainen, F. T. Ulaby, M. C. Dobson, M. A. El-Rayes, and L. Wu, "Microwave Dielectric Behavior of Wet Soil – Part I: Empirical Models and Experimental Observations," *IEEE Transactions on Geoscience and Remote Sensing*, vol. 23, pp. 25–34, 1985.

[15] B. Brisco, T. J. Pultz, R. J. Brown, G. C. Topp, M. A. Hares, and W. D. Zebchuck, "Soil Moisture Measurement Using Potable Dielectric Probes and Time Domain Reflectometry," *Water Resources Research*, vol. 28, pp. 1339–1346, 1992.

[16] M. C. Dobson, F. T. Ulaby, M. T. Hallikainen, and M. A. El-Rayes, "Microwave Dielectric Behavior of Wet Soil – Part II: Dielectric Mixing Models," *IEEE Transactions on Geoscience and Remote Sensing*, vol. 23, pp. 35-46, 1985.

[17] F. T. Ulaby, R. K. Moore, and A. K. Fung, *Microwave Remote Sensing: Active and Passive, vol. II*, Artech House, Norwood, Massachusetts, pp. 860-862, 1986.

[18] L. Bruckler, H. Witono, and P. Stengel, "Near Surface Soil Moisture Estimation from Microwave Measurements," *Remote Sensing of Environment*, vol. 26, pp. 101-121, 1988.

[19] J. P., Walker, P. A. Troch, M. Mancini, G. R. Willgoose, and J. D. Kalma, "Profile Soil Moisture Estimation Using the Modified IEM," *1997 IEEE International Geoscience and Remote Sensing Symposium Proceedings (IGARSS'97)*, Vol. 3, pp. 1263-1265, 1997.

[20] A. Le Morvan, M. Zribi, N. Baghdadi, and A. Chanzy, "Soil Moisture Profile Effect on Radar Signal Measurement," *Sensors*, vol. 8, pp. 256-270, 2008.

[21] D. Entekhabi, H. Nakamura, and E. G. Njoku, "Solving the Inverse Problem for Soil Moisture and Temperature Profiles by Sequential Assimilation of Multifrequency Remotely Sensed Observations," *IEEE Transactions on Geoscience and Remote Sensing*, vol. 32, pp. 438–448, March 1994.

[22] J. F. Galantowitz, D. Entekhabi, and E. G. Njoku, "Tests of Sequential Data Assimilation for Retrieving Profile Soil Moisture and Temperature from Observed L-band Radiobrightness," *IEEE Transactions on Geoscience and Remote Sensing*, vol. 37, pp. 1860–1870, July 1999.

[23] F. T. Ulaby, R. K. Moore, and A. K. Fung, *Microwave Remote Sensing: Active and Passive*, Vol. I. Addison-Wesley, Reading, Massachusetts, pp. 82–87, 1981.

[24] A. Tabatabaeenejad and M. Moghaddam, "Bistatic Scattering from Three-Dimensional Layered Rough Surfaces," *IEEE Transactions on Geoscience and Remote Sensing*, vol. 44, pp. 2102–2114, August 2006.

[25] C. Kuo and M. Moghaddam, "Electromagnetic Scattering From Maltilayer Rough Surfaces With Arbitrary Dielectric Profiles for Remote Sensing of Subsurface Soil Moisture," *IEEE Transactions on Geoscience and Remote Sensing*, vol. 45, pp. 349–366, February 2007.

[26] A. Tabatabaeenejad and M. Moghaddam, "Inversion of Subsurface Properties of Layered Dielectric Structures With Random Slightly Rough Interfaces using the Method of Simulated Annealing," *IEEE Transactions on Geoscience and Remote Sensing*, vol. 47, pp. 2035–2046, July 2009.

[27] S. H. Lou, L. Tsang, C. H. Chan, and A. Ishimaru, "Application of the Finite Element Method to Monte Carlo Simulations of Scattering of Waves by Random Rough Surfaces With the Periodic Boundary Condition," *Journal of Electromagnetic Waves and Applications*, vol. 5, pp. 835–855, 1991.

[28] K. Pak, L. Tsang, L. Li, and C. H. Chan, "Combined Random Rough Surface and Volume Scattering Based on Monte Carlo Simulations of Solutions of Maxwell's Equations," *Radio Science*, vol. 28, pp. 331–338, 1993.

[29] W. H. Peake and T. L. Oliver, *The Response of Terrestrial Surfaces at Microwave Frequencies*, Technical Report AFAL-TR-70301, Electroscience Laboratory, Ohio State University, Columbus, Ohio, 1971.

[30] T. D. Wu, K. S. Chen, J. Shi, and A. K. Fung, "A Transition Model for the Reflection Coefficient in Surface Scattering," *IEEE Transactions on Geoscience and Remote Sensing.*, vol. 39, pp. 2040–2050, 2001.

[31] S. O. Rice, ''Reflection of Electromagnetic Waves from Slightly Rough Surfaces,'' *Communications on Pure and Applied Mathematics*, vol. 4, pp. 361–378, 1951.

[32] P. Beckmann and A. Spizzichino, *The Scattering of Electromagnetic Waves from Rough Surfaces*, Artech House, Norwood, Massachusetts, 1987.

[33] J. R. Wang, P. E. O'Neill, E. T. Engman, R. Pardipuram, J. C. Shi, and A. Y. Hsu, "Estimating Surface Soil Moisture from SIR-C Measurements over the Little Washita Watershed," *1995 International Geoscience and Remote Sensing Symposium (IGARSS '95)*, Vol. III, IEEE, pp. 1982–1984, 1995.

[34] S. L. Durden, J. J. van Zyl, and H. A. Zebker, "Modeling and Observations of the Radar Polarization Signatures of Forested Areas," *IEEE Transactions on Geoscience and Remote Sensing*, vol. 27, pp. 290–301, 1989.

[35] F. T. Ulaby and M. A. El-Rayes, "Microwave Dielectric Spectrum of Vegetation Part II: Dual-Dispersion Model," *IEEE Transactions on Geoscience and Remote Sensing*, vol. 25, pp. 550–557, 1987.

[36] J. J.van Zyl, "The Effects of Topography on the Radar Scattering from Vegetated Areas," *IEEE Transactions on Geoscience and Remote Sensing*, vol. 31, pp. 153–160, 1993.

[37] M. Arii, "Soil Moisture Retrieval under Vegetation Using Polarimetric Radar," Ph.D. dissertation, California Institute of Technology, Pasadena, California, 2009.

[38] D. Entekhabi, E. G. Njoku, P. Houser, M. Spencer, T. Doiron, Y. Kim, J. Smith, R. Girard, S. Belair, W. Crow, T. J. Jackson, Y. H. Kerr, J. S. Kimball, R. Koster, K. C. McDonald, P. E. O'Neill, T. Pultz, S. W. Running, J. Shi, E. Wood, and J. van Zyl, "The Hydrosphere State (Hydros) Satellite Mission: an Earth System Pathfinder for Global Mapping of Soil Moisture and Land Freeze/Thaw," *IEEE Transactions on Geoscience and Remote Sensing*, vol. 42, pp. 2184–2195, 2004.

[39] F. Baup, , E. Mougin, P. Hiernaux, A. Lopez, P. D. Rosnay, and I. Chenerie, "Radar Signatures of Sahelian Surfaces in Mali Using ENVISAT-ASAR data," *IEEE Transactions on Geoscience and Remote Sensing*, vol. 45, pp. 2354–2363, 2007.

[40] K C. McDonald, R. Zimmermann, and J. S. Kimball, "Diurnal and Spatial Variation of Xylem Dielectric Constant in Norway Spruce (Picea abies [L.] Karst.) as Related to Microclimate, Xylem Sap Flow, and Xylem Chemistry," *IEEE Transactions on Geoscience and Remote Sensing*, vol. 40, pp. 2063–2082, September 2002.

[41] W. Wagner and K. Scipal, "Large-Scale Soil Moisture Mapping in Western Africa Using the ERS Scatterometer," *IEEE Transactions on Geoscience and Remote Sensing*, vol. 38, pp. 1777–1782, 2000.

[42] P. E. O'Neill, A. Joseph, G. De Lannoy, R. Lang, C. Utku, E. Kim, P. Houser, and T. Gish, "Soil Moisture Retrieval Through Changing Corn Using Active/Passive Microwave Remote Sensing," *2003 IEE International Geoscience and Remote Sensing Symposium (IGARSS 2003: Learning from Earth's Shapes and Sizes*, Toulouse, France, pp. 407–409, July 2003.